MULTIPHASE FLOW ESTIMATION USING IMAGE PROCESSING

BY

MUSTAFA AHMAD ALNASER

A Dissertation Presented to the

DEANSHIP OF GRADUATE STUDIES

KING FAHD UNIVERSITY OF PETROLEUM & MINERALS

DHAHRAN, SAUDI ARABIA

In Partial Fulfillment of the
Requirements for the Degree of

DOCTOR OF PHILOSOPHY

In

SYSTEMS & CONTROL ENGINEERING

APRIL 2016

KING FAHD UNIVERSITY OF PETROLEUM AND MINERALS

DHAHRAN- 31261, SAUDI ARABIA

DEANSHIP OF GRADUATE STUDIES

This thesis, written by **MUSTAFA AHMAD ALNASER** under the direction of his thesis advisor

and approved by his thesis committee, has been presented and accepted by the Dean of Graduate

Studies, in partial fulfillment of the requirements for the degree of **DOCTOR OF PHILOSOPHY**
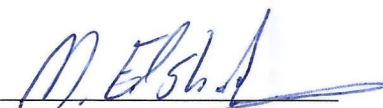
IN SYSTEMS & CONTROL ENGINEERING

Dr. Moustafa Elshafei
(Advisor)

Dr. Abdelsalam Al-Sarkhi
(Co-Advisor)

Dr. Hesham K. Al-Fares
Department Chairman

Dr. Sami El-Ferik
(Member)

Dr. Salam A. Zummo
Dean of Graduate Studies

Dr. Fouad M. Al-Sunni
(Member)

_____24/5/16_____
Date

Dr. Abdul-Wahid A. Saif
(Member)

Dedication

To My Father, My Mother and My Wife

ACKNOWLEDGMENTS

TABLE OF CONTENTS

LIST OF TABLES

LIST OF FIGURES

LIST OF ABBREVIATIONS

Symbols

f	*Original image*
g	*Segmented image*
Th	*Threshold [-]*
H	*Hold up [-]*
A	*Area [m^2]*
Vol	*Volume [m^3]*
r	*Radius [m]*
D	*Diameter [m]*
Win	*Window*
in	*intensity value*
$Hist$	*Histogram*
$Tran$	*Transformation function.*
J	*Bubble polar momentum of inertia [m^4]*
a	*ellipse major axis [m]*
b	*ellipse minor axis [m]*
x	*Coordinate*
y	*Coordinate*
z	*Coordinate*
t	*Time[s]*
FR	*Frame Rate [fps]*

Pix	*Pixel*
V	*Velocity [m/s]*
Ro	*Roundness Value*
M	*Number of images*
d	*Distance [pixel , meter]*
W	*Wave*
u,v,w	*offset in x, y, z respectively [pixel]*
NF	*Number of frames*
n	*Number of pixels*
R	*Cross Correlation Function*
S	*Perimeter [m]*
Fre	*Frequency*
Tr	*Time Resolution*
Rd	*Dynamic Range*
Cont	*Contrast*
FOV	*Field of View [m]*
FW	*Frame Width [pixel]*
Li	*Intensity Levels*
C	*Celerity [m/s]*
Vs	*Superficial Velocity [m/s]*
A	*Pipe Cross sectional Area [m2]*
q	*Volume flow rate [m3/s]*
P	*Pressure [Pa]*

Re	*Reynolds number [-]*	
l	*Length [m]*	
X^*	*Modified Lockhart- Martinelli parameter*	
T	*Period [s]*	
xm	*Mass Quality*	
$\dot{m}$	*Mass Flow Rate*	
m	*Mean*	
Var	*Variance*	
∇	*Gradient*	
E	*Energy*	
αi	*Weighting parameter*	

Greek symbols

ε	Volumetric Gas Fraction [-]
μ	Deformation factor
β	Calibration correction value
Δ	Difference
μ	Viscosity *[Pa·s]*
ρ	Density *[kg/m³]*
$\emptyset$	Pressure Drop Multiplier *[-]*
α	Phase fraction
σ	*Standard Deviation*

Subscripts

im	*Image*
O	*Oil*
G	*Gas*
Wa	*Water*
B	*Bubble*
s	*Size*
Sl	*Slug*
N	*Nose*
Ta	*Tail*
i	*Field index , x-direction*
j	*Field index , y-direction*
k	*Field index , z-direction*
I	*Pixel Index*
W	*Wave*
p	*Pipe*
fr	*Frame*
Amp	*Amplitude*
L	*Liquid*
TP	*Two Phase*
acc	*Acceleration*
fric	*Friction*
ga	*Gravity*
Lo	*Liquid Only*

l	*Length*
Samp	*Sampling*

ABSTRACT

Full Name   : [MUSTAFA AHMAD ALNASER]

Thesis Title   : [Multiphase Flow Estimation Using Image Processing]

Major Field   : [Systems & Control Engineering]

Date of Degree : [April , 2016]

Multiphase flow measurement is one of challenging issues in process industry. Multiphase flow measurement requires estimation of several parameters such as phase hold up, phase velocity and bubbles characteristics and other parameters. There are various technologies to measure/ estimate multiphase flow parameters. One of the promising approaches is the image/video processing technique. The image processing techniques are utilized for estimating several multiphase flow parameters such as hold up, bubble size distribution, velocity, wavelength, wave frequency, wave period and wave amplitude. In this work, a high speed vision system is used to capture the video for multiphase flow in a flow loop built at KFUPM. In particular, multiphase flow parameters are estimated for Stratified Wavy flow pattern using image processing techniques. Artificial Intelligence (AI) techniques are also explored to identify the flow patterns at different flow conditions. We used an Artificial Neural Network (ANN) for flow pattern identification with pre-processing stage using natural logarithmic normalization. This pre-processing stage helps to normalize large data ranges and to improve identification of flow patterns in the transition regions. The validity of the model was extended by using dimensionless inputs to be used

for horizontal pipes of various diameters, liquid's densities and viscosities. The concept was verified and validated by building and testing the model using experimental data. The efficiency of the proposed approach was demonstrated by an ANN model using only three dimensionless parameters, namely, Liquid Reynolds Number, Gas Reynolds Number and Pressure Drop Multiplier to identify 4 flow patterns close to their critical transition.

ملخص الرسالة

الاسم الكامل: مصطفى أحمد فيصل الناصر

عنوان الرسالة: تقدير خواص تدفق السوائل المتعددة الأوجه باستخدام معالجة الصور

التخصص: هندسة الأنظمة والتحكم

تاريخ الدرجة العلمية: أبريل , 2016

قياس تدفق الموائع متعددة الأطوار هي مسألة صعبة للغاية في الصناعة. قياس تدفق الموائع متعددة الأطوار يتطلب تقدير العديد من المعاملات مثل كمية المائع ، سرعه المائع في كل طور وخواص الفقاعات وغيرها من المعاملات. هناك تقنيات مختلفة لقياس / تقدير معاملات تدفق الموائع متعددة الأطوار. إحدى الطرق الواعدة هي استخدام ومعالجة الصور لتقدير معاملات تدفق الموائع متعددة الأطوار. تمت الاستفادة من تقنيات معالجة الصور لتقدير العديد من تدفق الموائع متعددة الأطوار مثل كمية المائع، تصنيف الفقاعات بناء على حجمها والسرعة، والطول الموجي وتردد وفترة الموجه وسعة الموجة. في هذا العمل، استخدم نظام رؤية عالية السرعة لالتقاط الفيديو لتدفق للموائع متعددة الأطوار في حلقة تدفق بنيت في جامعة الملك فهد. على وجه الخصوص ، قمنا بتقدير معاملات نظام التدفق الطبقي المتموج باستخدام تقنيات معالجة الصور. ثم، تم استكشاف واستغلال تقنيات الذكاء الاصطناعي (AI) للتعرف على أنماط التدفق في ظروف تدفق مختلفة. استخدمنا الشبكات العصبية الاصطناعية (ANN) لتحديد نظام تدفق لكن مع مرحلة ما قبل المعالجة باستخدام التطبيع اللوغاريتمي الطبيعي. هذه مرحلة ما قبل المعالجة تساعد على تطبيع مجموعة كبيرة من البيانات والحد من التداخل بين نظم التدفق وتحسن دقة التعرف على نظام التدفق. ثم، تم تمديد صلاحية النموذج باستخدام مدخلات غير بعدية لاستخدامها في الأنابيب الأفقية ذوات أقطار مختلفة، وسوائل ذوات كثافة ولزوجة مختلفة. تم التحقق من صحتها من خلال بناء واختبار نموذج باستخدام البيانات التجريبية. تم التحقق من فعالية هذا الأسلوب من خلال نموذج شبكات عصبية ANN باستخدام ثلاث مدخلات غير بعدية فقط وهي رقم رينولدز للسائل ورقم رينولدز للغاز و هبوط الضغط المضاعف.

CHAPTER 1

INTRODUCTION

Multiphase flow refers to the flow of two phases or more and they can be liquid, gas, solid and may also be two components from the same phase such as oil and water. Multiphase flow is encountered in many industries and processes such as Oil and Gas industry and petrochemical process. Since early eighties, a number of multiphase flow meters were developed by various research institutes, flow meter manufacturers and oil and gas operators [1]. By mid-ninety, multiphase flow meters became widely adopted solution by operators in oil and gas field [2]. Multiphase flow meter market was about $ 240 million in 2011 and it is expected to grow up to $ 472.2 million in 2016 [3].

Multiphase flow meter (MPFM) gradually replaced the conventional test separators in oil and gas industry, which are costly to acquire, operate, and maintain. They also require large space which may not be feasible especially in offshore platforms. In addition, it is not possible to perform continuous monitoring using test separator. On the other hand, multiphase flow meters can perform continuous well monitoring which is useful for production optimization, reservoir monitoring and flow assurance. Other important applications of multiphase flow meters are production allocation metering, well testing and custody transfer metering [1]. In spite of advantages of multiphase flow meters, the current technology has several limitations. The first limitation is the uncertainty of measurement due to complexity of flow [1]. The second limitation is the difficulty to find representative

samples since MPFM needs prior information about the fluid properties [1]. The third limitation, which is considered the weakest point in these technologies, is the need to identify flow patterns which are more than 20 types such as bubble flow, Slug flow and Annular flow. The identification of flow pattern becomes even more difficult at the transition zone between flow patterns [4, 5].

There are many hardware multiphase flow metering system developed by different manufactures utilizing several measurement technologies to meet the demand of multiphase flow measurement especially of oil and gas field. However, current multiphase meters are quite expensive, and still lacking sufficient accuracy. Alternative solutions are called soft-sensing or estimation methods. These techniques utilize existing and simple measurements. In the following section, we will review the flow patterns types and the existing solutions for multiphase flow meters.

1.1 Flow Patterns

The multiphase flow can take various forms and this is one of the most challengeable aspects in dealing with multiphase flow. There are more than 20 main flow patterns .The flow patterns depends on many factors such as operating conditions , flow rates and pipe inclination as shown in Figure 1-1, [6].

1.1.1 Flow Patterns in Vertical Pipes

Basically there are four main types of flow patterns in vertical pipes: bubbly, churn, slug, annular and there are other subtypes such as annular with droplets.

a) **Bubble flow**: It has a continuous liquid phase with gas bubbles that are dispersed in it.

b) **Slug flow**: It is formed when the gas void fraction increases causing the small gas bubble to collide and form larger gas bubbles that can reach up to the diameter of the pipe. Slug flow is very dangerous, as it creates large fluctuation in the fluid pressure inside the pipe and terminal equipment.

c) **Churn flow**: It is formed at high velocity and breaking down big slug bubbles .This flow pattern can be considered as an intermediate flow pattern between the slug flow and annular flow.

d) **Annular flow**: In this type, the liquid phase moves as thin film on the pipe wall and it occurs when the gas travels at high velocity and the interfacial shear becomes dominant on the gravity.

1.1.2 Flow Patterns in Horizontal Pipes

a) **Bubbly flow:** As in the vertical pipes, Bubbly flow has a continuous liquid phase in which the gas bubbles are dispersed. For horizontal pipes, this can happen only at high mass flow rates.

b) **Annular flow:** Similar to the vertical pipe case, the liquid phase forms a continuous film on the pipe wall when the gas travels at high velocity. However, in the horizontal pipe case the lower film is thicker than the upper one.

c) **Slug flow:** Gas bubbles become larger and can reach to almost diameter of the pipes and cause discontinuities in the liquid phase.

d) **Elongated Bubble flow** (Plug flow): In this type of flow, there are liquid plugs and gas bubbles with a smaller diameter than pipe diameter. The liquid phase is continuous in the lower part of the pipe.

e) **Stratified flow:** In this type, the liquid phase travels in the lower part of the pipe and the gas in the upper part. The boundary between the two phases is smooth. As the velocity of the gas increases, the boundary between the two phases becomes wavy. In this case, the flow pattern is known as **Stratified Wavy** flow.
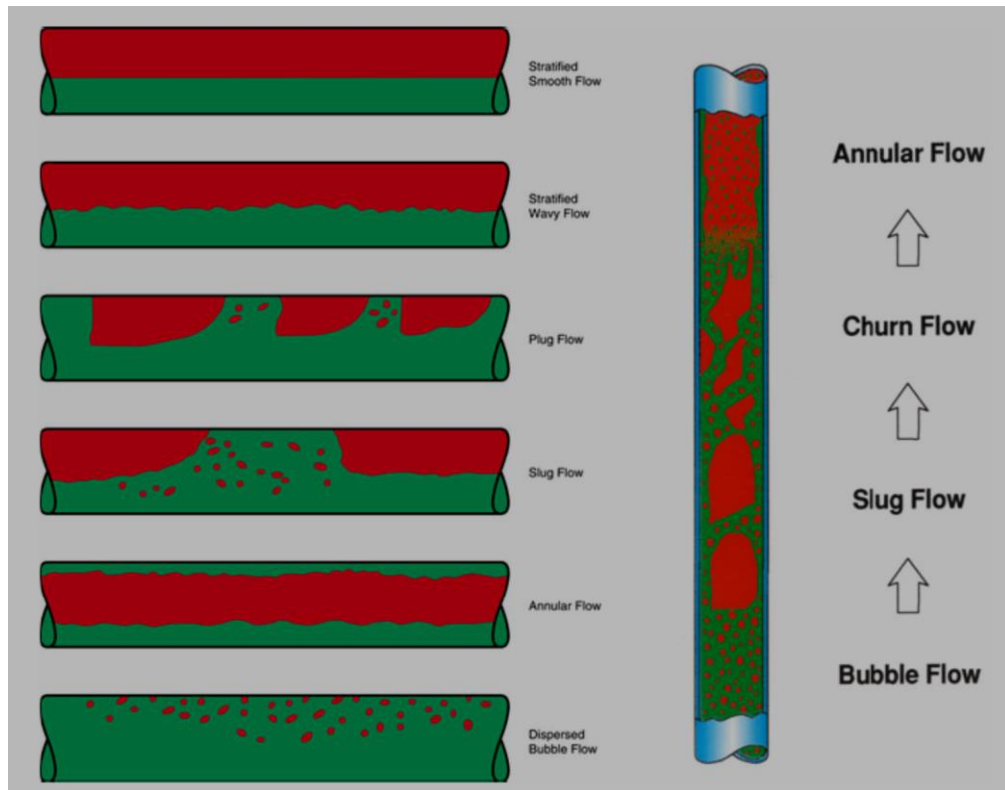
Figure 1-1: Common Multiphase flow patterns. [7]

1.2 Multiphase Flow Measurement Techniques

In general, the multiphase techniques used in the current multiphase meters can be divided to two main types [8]:

4

1- First Approach: the techniques used to measures the flow parameters as functions of the flow rates. Examples of these meters are differential pressure meters and nuclear meters.

2- Second Approach: This type measures the basic parameters of the phase velocities, phase cross-sectional fractions (holdups), or quantities that can be explicitly related to these parameters. Cross –Correlation meters utilize this type of measuring approach.

In the next section, a description of current multiphase meters for liquid dominant flow is presented as the main focus of this work is on liquid dominant type

1.2.1 Multiphase Flow Metering (liquid dominant)

Liquid dominant does not mean that it is always predominance of liquid phase over gas phase but the multiphase measurement techniques are designed in such way that the operation start from the far end of the spectrum at which the liquid flow is 100 %. In general, most of the multiphase techniques are composed of three equations with three unknown flow fractions (Oil, Gas, and Water). Every technique takes various forms with some other auxiliary equations to find other physical properties of each phase such as density ρ and phase fractions α as follows:

$$\alpha_O + \alpha_G + \alpha_{Wa} = 1 \tag{1.1}$$

$$\rho_{mix} = \rho_O \alpha_O + \rho_G \alpha_G + \rho_{Wa} \alpha_{Wa} \tag{1.2}$$

where O refers to oil , G refers to Gas , Wa refers to water and mix refers to mixture

However, current commercial meters still lack the sufficient accuracy since they depend mainly on the flow modelling. This modelling inaccuracy arises because these models are based on lab tests which provide an estimation of the actual situation only, [6].

The common multiphase flow techniques are: Differential Pressure meters, Nuclear meter, and cross correlation meter.

1-Differential Pressure Meter (DP):

DP based meter is a common multiphase flow meter and it utilizes the Venturi meter or any other DP device to provide total flow only. To provide three phase flow, the DP meters readings are combined with other techniques measurement such as densitometry, cross- correlation and water cut. However, the DP based meters do not provide accurate measurement in case of multiphase flow because of rapid change of Reynolds numbers, [6, 9].

2- Nuclear Meters:

There are two main types of nuclear meters: High Energy Gamma Ray & Low Energy Gamma Ray.

a) High Gamma Ray Meters:

In this type of meters, the gamma ray stream is passed perpendicularly through the flow and the photons are counted at other side. In fact, some of the gamma ray stream reach to the opposite side and some of it could be absorbed by the material and this depends on the density of the material. So, the difference between the count on the initial point and that of the opposite side give the average density of flow. These meters use high energy source which allow the ray to pass through pipe wall and this make it as non-intrusive techniques, [6].

b) Low Gamma Ray Meters:

These meters can work on lower energy level and two separate energy levels called multiple energy gamma ray spectroscopies. The attenuation of distinct spectral lines resulting from using multiple energy levels can be fed to the flow models to find the flow components fractions (Composition). So, the attenuation of the two energy levels rely mainly on the fraction of oil, gas & water. The measurement of the gamma ray absorption must be done only at minimum of the two distinct energy.

Another approach in the nuclear metering technology is to use a nuclear source that can emit a low energy X-Ray. This approach is supposed to provide the optimal performance. However, X-Ray puts limitations on the diameter of the meter and it requires a low density window for the X-ray to reach the opposite side. In addition, this approach depends on the understanding of the flow components properties which are time varying parameters especially for water components, [6].
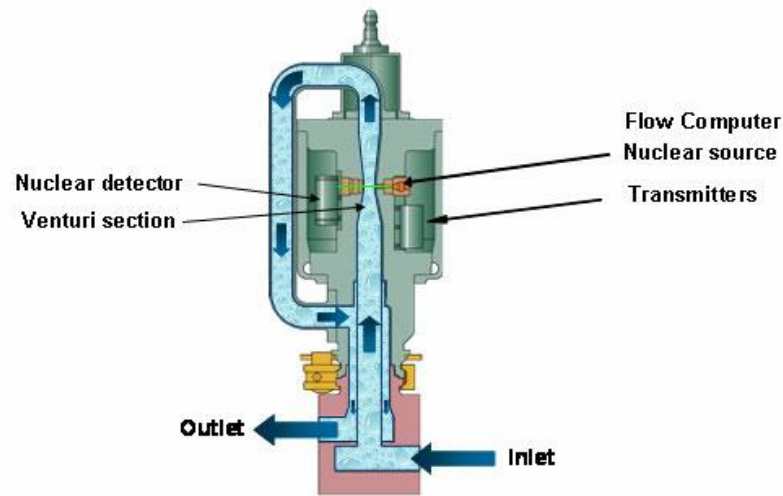
Figure 1-2: Nuclear Multiphase Flow Meters. [7]

3- Cross Correlation Techniques

7

Cross correlation techniques utilize two sensors to detect one of the flow parameters such as electrical conductivity or ultrasound. These two sensors are displaced at known distance and the travel time can be used to determine the stream velocity. However, this velocity is affected by type of flow pattern and sensing technology. For that reason, the slip equation should be involved also to find average stream velocity of the mixture, [6, 9].

4- Permittivity and Conductivity Techniques:

It is important to measure the electrical properties of multiphase flow such as capacitance and conductance of the multiphase flow mixture. Using electrical capacitance sensor to measure permittivity of the mixture can provide phase fraction of each phase. Capacitance sensor provide the best performance for oil continuous flow. Conductivity sensor measure the electrical properties by injecting electrical currents into the flow and measures the voltage difference through electrical probes. The measured electrical property can be used to determine the fraction of each phase in the mixture. Conductive sensor works well for water continuous flow, [6, 9].

5- Microwaves Techniques

Microwave is another approach to measure the multiphase flow mixture properties. Similar to capacitance sensor, the microwave measures the permittivity of the flow to determine the phase fraction but microwave techniques works well for both oil and water continuous flow, [6, 9].
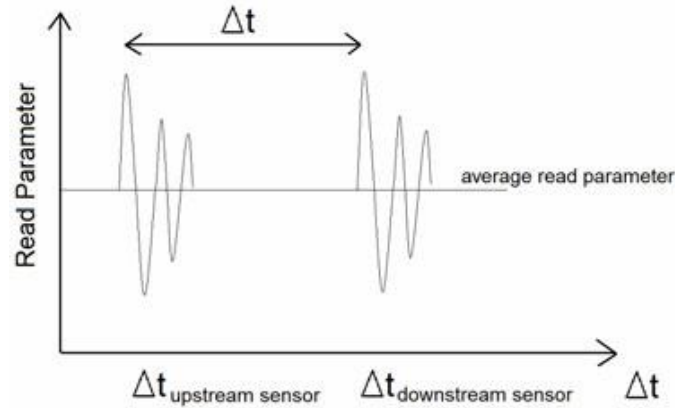
Figure 1-3: Cross Correlation. [7]

6- Soft Sensing Techniques

These techniques are very useful one because it does not need more infrastructures to the field and it is low cost and more flexible than hardware type. The soft meters gather main process data and utilize mathematical modeling and estimation techniques to provide multiphase flow characteristics. In terms of modeling, there are three main types: Empirical, which depends on the experimental data and Mechanistic which is built based flow dynamic physics and homogenous which assume homogenous mixture. Among of these models, the empirical type was the most common use one. Wallis [10] Lockhart and Martinelli [11] Duns and Ros [12] and Dukler et al. [13] Beggs and Brill [14] which are considered main works in multiphase flow field. Mechanistic models start to being used but still there is a need to use some empirical correlations with them. Taitel and Dukler [15], Barnea [16], Petalas and Aziz [17] are examples of the main work done using mechanistic.

Two common estimation approaches are used:

1. Probability theory based such as Kalman Filter and Extended Kalman Filter.

2. Numerical optimization based such as Moving Horizon Estimator.

9

The second approaches have better performance than first one but it requires longer computational time.

However, there are some issues about the performance of these techniques in estimating flow rates. These techniques lack the sufficient accuracy due to many reasons, such as:

1. Limitation of the dynamical models because these models are valid only in certain boundary conditions (depending on flow patterns).

2. Estimation accuracy is affected by measurement noise.

Soft meters have a potential in oil and gas industry and there is a need for them to reduce the hardware type which is very expensive but it is not possible to replace all hardware types.

In this work, we studied one of the relatively new technology implemented in multiphase flow area, namely, image processing which is very promising technology to enhance the accuracy for multiphase flow measurement.

1.3 Layout of the Thesis:

The layout of this Thesis is arranged as follows:

Chapter 2: Literature Review

Review for flow visualization system components, main multiphase flow parameters, limitations of the image processing and proposed solutions.

Chapter 3: Image Pre-Processing

Describe the common multiphase flow techniques that can be utilizes for multiphase flow estimation.

Chapter 4: Multiphase Flow Facility

Describe Multiphase flow facility used in this work and vision system

Chapter 5: Flow Features Extraction and Analysis

Estimate multiphase flow parameters for Stratified Wavy flow.

Chapter 6: Dimensionless Model for Flow Patterns Identification Using Artificial Neural Network.

Build AI model to identify flow patterns.

Chapter 7: Conclusion

CHAPTER 2

LITERATURE REVIEW

Introduction

Multiphase flow refers to the simultaneous flow of two phases or more and they can be liquid, gas, solid, two components from the same phase such oil and water, or two phases single component such as water vapor and liquid. Multiphase flow is encountered in many industries and processes such as oil and gas industry and petrochemical processes. There is an increasing demand for more accurate multiphase metering systems. Several approaches were reported in the literature in the modeling side to accurately identify the flow features and parameters [18]. One of the common difficulties in these techniques is the need to identify the flow pattern first for better estimation of the other multiphase flow parameters such as pressure gradient, liquid fractions and others. Flow patterns are more than 20 types including bubble flow, slug flow, annular flow and many more. These flow patterns depend on many factors such as pipe inclination, phase composition and physical properties, and velocity of the individual fluids, [5].

The overlapping between these flow patterns, especially at the transition zones makes the identification more difficult . The misidentification introduces metering errors, as these meters usually assume one type of flow patterns and are tuned based on it. Thus, identification of the correct flow pattern at different time interval will greatly improve the multiphase flow measurements, [4].

There are many hardware systems invented to meet the demand of multiphase flow measurement, [6, 19]. However, current multiphase meters are expensive, lacking sufficient accuracy and require re-tuning from time to time. Alternative solutions are called soft-sensors or virtual meters, [20]. These techniques utilize existing and simple measurements and use mathematical models to estimate multiphase flow parameters, [21, 22]. In terms of modeling, there are three main types: Empirical, which depends on the experimental data; Mechanistic which is based on flow physics and homogenous models which assume homogenous flow characteristics especially for physical properties of the phases, [18].Among of these models, the empirical type was the most commonly used one. There are many empirical correlations such as Lockhart and Martinelli [11] Beggs and Brill [14] and Mukherjee and Brill, [23]. However, the mechanistic models are more accurate. With the availability of powerful computing hardware and software, it becomes possible to be implemented efficiently, [24, 25, 26, 16, 17]. The current preferable practice is to use mechanistic models with help of empirical models, [18].

Image processing method started to be utilized in the field of multiphase flow due to the advancement of video processing systems and availability of low cost recoding system and powerful computing system, [27, 28, 29, 30]. Multiphase modeling can be used to verify the values of multiphase flow parameters estimated by image processing techniques.

In this chapter, the use of image processing for estimating main multiphase flow parameters will be presented. The main parameters addressed in the Literature are: hold-up, bubble size, phase velocity, bubble length and slug frequency. The inherent limitations of the image processing and some proposed enhancement methods will be discussed in details. The chapter is organized as follow: Section 2.1 describe flow visualization system components. Section 2.2 presents the techniques used for multiphase flow parameters

estimation, Section 2.3 discusses the current limitations of the image processing techniques and proposed solutions.

2.1 Flow Visualization System

Flow visualization system consists of three main components: imaging system, illumination system and processing unit, [30]. Imaging system is usually a high speed video capturing device such as high speed camera. There are several specifications of high speed camera that should be carefully selected based on the objective and application. The first specification is the frame rate, which is defined as the number of frames per unit time (usually second) (FPS) or the camera frequency (Hz). This specification should be selected based on the flow velocity to captures all necessary details while avoiding redundant information. It may be as low as 60 FPS [31] and high up to 10000 FPS [32], so, as the flow velocity increases, FPS should also increase, [33, 34]. Another aspect is the type of applications: online or offline. If it is online, then FPS should be minimized to reduce the processing time, [28]. The second specification is the shutter speed or exposure time which is the amount of time each frame is exposed to light and it is expressed in fractions of second. This feature is needed to be tuned carefully to avoid blurred image and get clear images, [33]. Fast shutter speed is usually used to freeze the fast moving objects which is needed in high velocity case, but it should be optimized to avoid redundant frames. Another specification is the image spatial resolution which is defined as the number of pixels or dots per unit area. Spatial resolution is an important specification because it determines the clarity of the image. Although high spatial resolution is preferred to show flow details more clearly, the recording time will be longer which results in fewer number of frames per second. So, there should be a compromise between image spatial resolution and frame rate,

[35]. Spatial resolution should not be mixed with pixel resolution which is the total number of pixels in the image or pixel dimensions. In other words, the number of pixel in the image does not determine the clarity of the image, [36, 37]. Image clarity is important to identify the flow characteristics correctly such as boundaries between different phases.

The second component of the visualization system is the illumination system. There are several illumination devices that can be used to illuminate the flow such as Halogen lamp [38], light emitting diode array [35], fluorescent lamp [27] and laser [28], which is preferred for contaminated liquid. The illumination of the test section should be arranged in proper way to avoid light reflection and have a uniform illumination. Uniform illumination eliminates the need of advanced thresholding techniques to compensate for the non-uniform illumination, which usually requires long processing time and careful tuning of thresholding parameters, [39]. A rectangular transparent box filled with water can be installed at the test section around the pipe to reduce the image distortion from light source [28] and a diffusive surface is installed between the lamp and the box [33, 38] or a diffusive light emitting diode array to achieve uniform illumination, [35]. Another technique to improve the quality of the image is the backlighting using reflected light on a white screen to illuminate the test section, [40].

The third components of flow visualization system is the processing unit which is usually a PC with high computing capabilities and fast processing speed to meet the requirements of image processing especially for online applications. Image processing algorithm running on the PC will be explained in the coming sections.

There are several interface that can be used to connect the camera with computer: USB, Firewire and Gigabit Ethernet (GigE). The selection of the proper interface depends

on several factors such as the supported cable length, immunity to industrial noise due to electromagnetic fields and speed of data transfer. Table 2-1 summaries the key features of the existing camera interface, [41, 42].

Table 2-1: Camera Interfaces Comparison. [41, 42]

Spec/Interface	Camera Link	USB.2	USB.3	Firewire	Gigabit Ethernet
Speed	2 Gbps (Base) 6.1 Gbps (Full	480 MB/s	5 Gbps	786 MB/s	1 Gbps
Cable length	10 m	3 m	3 m	4.5 m	100 m
Real time trigger	Yes	No	No	No	No
Frame Grabber	Yes	No	No	No	No
Immunity to industrial noise	Yes	No	No	Yes	Yes

2.2 Multiphase Flow Parameters Estimation

2.2.1 Hold Up:

Hold up, which is the area or volume fraction of the phase, is a key parameter in multiphase flow analysis. In order to estimate the holdup of each phase using image processing, the area of each phase is needed to be labeled. Two main algorithms are used to estimate hold up based on flow conditions.

1) Labeling using boundary**:**

This algorithm is used for flow types which have clear boundaries such as stratified flow and plug flow. The boundaries can be extracted using edge detection techniques such as canny operator or morphological boundary extraction algorithms. The second algorithm provides better results than the former one [31].

2) Labeling using the pixel intensity:

This algorithm is used for cases at which the boundaries are not clear such as the stratified wavy, slug and annular flow. In these types of flow, three phases can coexist: gas, liquid, and mixture of gas and liquid. As a result, it is very difficult to identify clearly the boundary between different phases. Also, there are variety of pixel intensity due to non-uniform mixing in the mixture zone. After the implementation of the initial steps and producing the gray image, the pixels are classified into six different levels based on the intensity value as shown in the Table 2-2 and Table 2-3. [31]

Table 2-2: Labeling Levels and Intervals. [31]

Name	Interval
Liquid	$0 <= in < 80$
Gas & Liquid mix Level 1	$80 <= in < 105$
Gas & Liquid mix Level 2	$105 <= in < 130$
Gas & Liquid mix Level 3	$130 <= in < 160$
Gas & Liquid mix Level 4	$160 <= in < 200$
Gas & Liquid mix Level 5	$200 <= in < =225$

Table 2-3: Used Levels for Frame to Generate Gas and Liquid Mixture. [31]

Frame Type	Used Levels for liquid and gas mixture
Dispersed Annular	Level 4 and Level 5
Wavy Annular	Level 3, Level 4 , Level 5
Dispersed Bubble	Level. 1, Level 2, Level 3, Level 4, Level 5

Since the flow patterns are not known in advance, it is better to use the combination of algorithms to get the best results. Also, combination of two algorithms can be used for three phase flow case because using the boundaries is not enough to identify three phases in the image. Once the liquid and gas phase are labeled, the holdup of any phase can be calculated as follow:

$$H_L = \frac{A_L}{A} \tag{2.1}$$

$$H_G = 1\text{-}H_L \tag{2.2}$$

where H_L is the liquid hold up, H_G is the gas hold up or void fraction, A_L is the area occupied by the liquid phase A_p total cross sectional area of the pipe.

In some applications, Volumetric Hold up $\widetilde{H}_L$ is used instead of cross sectional hold up.

$$\widetilde{H}_L = \frac{Vol_L}{Vol} \tag{2.3}$$

where Vol_L is the volume of the liquid and Vol is the total volume.

In order to calculate the volumetric hold up, disk method is used. It is required to measure the radius and find a function to integrate it and get the volume. This is done by the following two steps:

1- Calculate the distance between the bottom of the image and the oil-water interface.

2- Obtain a polynomial fit for the radius $r(x)$. For Annular flow as an example, the polynomial fit is given by [43]:

$$r(x) = x^4 + a_3 x^3 + a_2 x^2 + a_1 x^1 + a_0 \tag{2.4}$$

where x is the axial direction. Then the volume can be calculated as:

$$Vol_L = \int_l^{l_p} \pi r^2 (x) dx \tag{2.5}$$

where l_p is the pipe section length, x is the axial direction.

Then, the liquid hold up can be calculated using equation (2.3). [43]

2.2.2 Bubble Size

Another important parameter which can be estimated using image processing is bubbles sizes. In most of the cases, the shape of the bubbles are assumed as either a sphere

or an ellipsoid. These bubbles are projected on 2D plane as either circle or ellipse. The spherical bubble is simplest assumption to classify. Once the bubble is projected as a circle, the radius of the bubble can be calculated. However, this assumption reduces the accuracy of BSD (Bubble Size Distribution) calculation because non-circular bubbles are not counted as shown in the Figure 2-1.
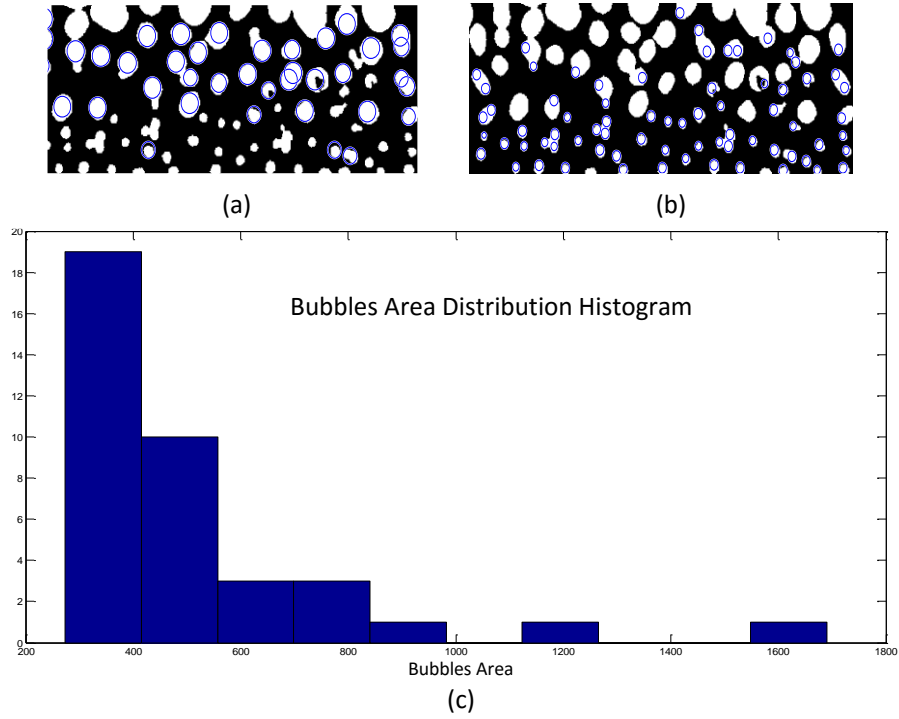
Figure 2-1: Classification of the bubble based assuming spherical shape: (a) Bubbles with radius 8-10, (b) Bubbles with radius 3-5, (c) Bubble Size Histogram.

Ellipsoid bubble assumption is more general than spherical ones and it provides better results. Projected ellipsoid semi axes can be estimated from bubble shadow area and bubble polar moment of inertia. Then, volume of the bubble is calculated by assuming that bubble extension in third dimension is equal to the larger diameter of the ellipsoid. Finally, the bubble diameter can be calculated from a sphere with same volume [35]:

$$A_B = \pi a b \cong A_{Pix} \cdot \sum_I n_I \qquad (2.6)$$

19

$$J_z = \frac{\pi ab}{4}(a^2 + b^2) \cong A_{Pix}{}^2 \cdot \Sigma_I[(x_I - \bar{x})^2 + (y_I - \bar{y})^2] \tag{2.7}$$

$$a = \frac{1}{2}\left[\left(\sqrt{\left(\frac{4J_z}{A_B} + \frac{2A_B}{\pi}\right)}\right) + \left(\sqrt{\left(\frac{4J_z}{A_B} - \frac{2A_B}{\pi}\right)}\right)\right] \tag{2.8}$$

$$b = \frac{1}{2}\left[\left(\sqrt{\left(\frac{4J_z}{A_B} + \frac{2A_B}{\pi}\right)}\right) - \left(\sqrt{\left(\frac{4J_z}{A_B} - \frac{2A_B}{\pi}\right)}\right)\right] \tag{2.9}$$

where A_B is the area occupied by the bubble shadow, A_{Pix} is the pixel area, a is the ellipse major axis and b is the ellipse minor axis and J_z is the bubble polar moment of inertia, $(\bar{x}, \bar{y})$ is the bubble center of mass , n is the number of pixels that belong to the bubble projection.

Wire Mesh Sensor is an advanced technique that can be used for multiphase flow analysis with high spatial and temporal resolution. It consists of two sets of crossing electrodes. Transmitter set are sequentially activated and the receiver set measures the conductivity of the passing fluid at each crossing point which provides instantaneous cross sectional gas fraction distribution as shown in Figure 2-2 (a, b, c). Then, three dimensional bubble shape can be reconstructed and bubble diameters can be calculated as shown in Figure 2-2 (d). So, wire mesh sensor can be used for two phase flow based on the difference in conductivity between liquid and gas.
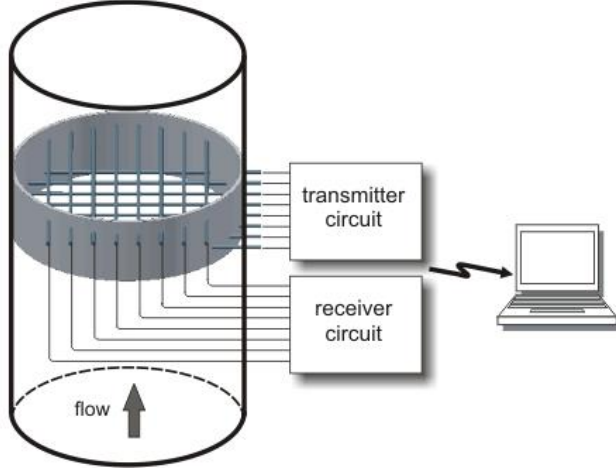
(a)

(b)
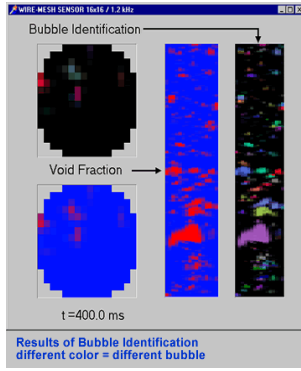
(c)
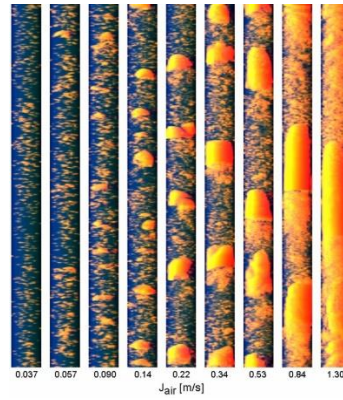
(d)
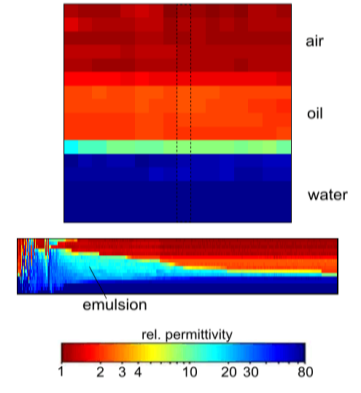
(e)

Figure 2-2: Wire Mesh Sensor: (a) Wire Mesh sensor principle [44], (b) Wire Mesh Hardware [44], (c) Bubble identification and void fraction [45], (d) 3-D Visualization of bubble [44], (e) the cross section of a stratified structure air/oil/water [46].

The bubble volume can be calculated by integration over gas fraction distribution elements $\varepsilon_{i,j,k}$ of a given bubble. The total gas volume that flows through one mesh of the sensor during a measuring time Δt can be calculated as [47]:

$$\boldsymbol{Vol_B} = \Delta x.\Delta y.\Delta t.\sum \varepsilon_{i,j,k} \cdot V_{g,i,j,k} \ , \forall \ [\boldsymbol{i,j,k}] \in \boldsymbol{B} \qquad (2.10)$$

where $\Delta x.\Delta y$ are lateral spacing between wires and $V_{g,i,j,k}$ is axial component of instantaneous local gas velocity.

Then, the bubble diameters can be calculated as follow [47]:

21

$$D_B = \sqrt[3]{\frac{6}{\pi} V_B}$$ (2.11)

Due to the difficulty in measuring gas phase velocity $V_{g,i,j,k}$, the equation (2.10) can be simplified by assuming the bubble velocity is approximately equal to gas phase velocity, Then, bubble volume can be calculated:

$$\frac{Vol_B}{V_{g,i,j,k}} = \widetilde{Vol}_B = \Delta x. \Delta y. \Delta t . \sum \varepsilon_{i,j,k} , \forall [i,j,k] \in B$$ (2.12)

However, wire mesh sensor may disturb the flow and may cause bubble fragmentation as the bubbles move through the wires which depends on how bubbles approach the wire and liquid superficial velocity as shown in Figure 2-3. As the bubble size increases, the effect of fragmentation decreases because of recombination due to coalescence. To compensate for that, bubble size can be calculated by integrating the local instantaneous gas fraction of measuring points' area occupied by bubble. [47, 48]
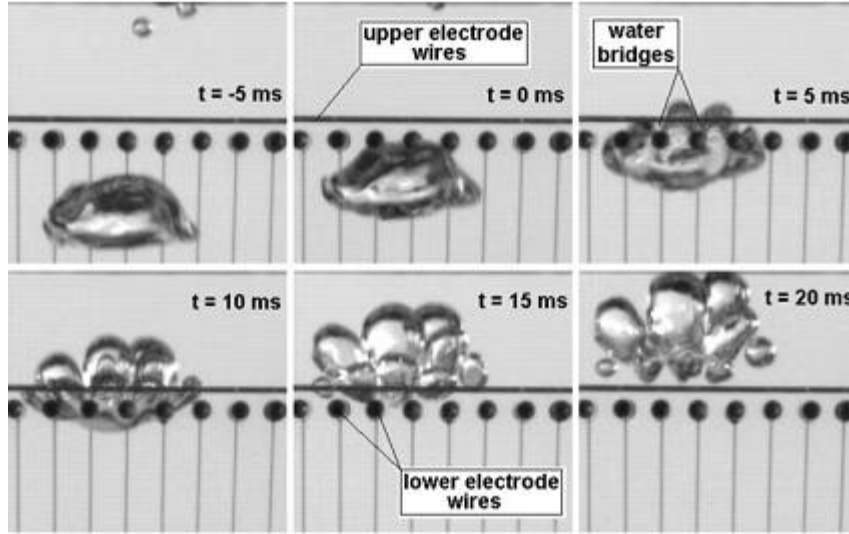
Figure 2-3: Bubbles Fragmentation by Wire mesh sensor. [47]

In real flow, the bubbles shape are mostly neither spherical nor ellipsoid. For that reason, other methods have been developed that can handle deformed bubbles such as semi-

ellipsoid bubbles or semi–spherical bubbles as shown in Figure 2-4. This method uses Hough Transform, which can cover most of bubble edge points, to extract the projected ellipse parameters from binary edge images. In this method, the bubbles are represented by two connected semi-ellipses with semi-major axis a and semi-minor axes b and μb instead of ellipse with major axis a and minor axis b. Using μ provides flexibility to express various shapes of bubbles and bubbles deformation. Using characteristic matrix method, 3D ellipsoid parameters can be extracted by matching between the characteristic points extracted from 2D planes with characteristic points extracted from 3D ellipsoid as shown in Figure 2-5. However, this method requires further simplifications to reduce computation effort and time to handle flow with higher velocities. [49]
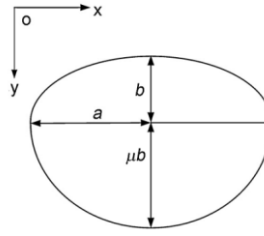
Figure 2-4: Diagram of Deformed Bubble (μ>1). [49]
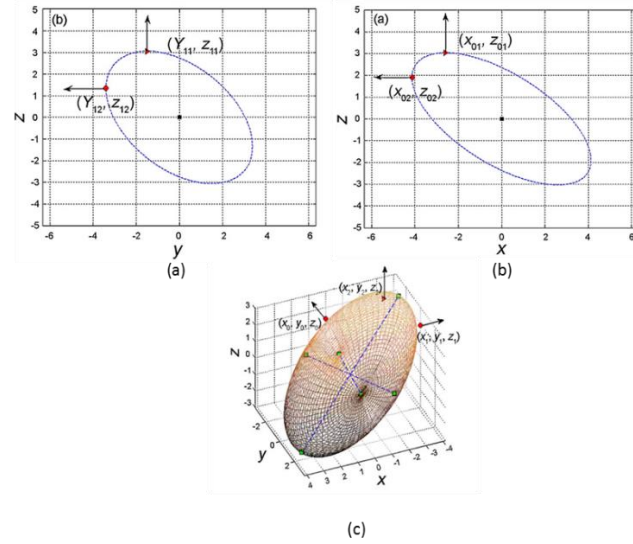
Figure 2-5: The Characteristic points of an ellipse on two projection planes: (a) x-z plane, (b) y-z plane, Characteristic points on 3D Ellipsoid. [49]

2.2.3 Fluid Velocity

1- Bubble Tracking:

In this approach, a label is assigned to each bubble, more specifically to its center of the mass. Then, the velocity of each bubble is calculated as a function of the bubble center of mass displacement related to the time interval between successive frames [35].

However, this method has the following limitations [35]:

a) If there are coalescence and break up events, then a new identity should be assigned to the new bubbles and the procedure is repeated again which reduces the efficiency of this approach.

b) It is not efficient for the flow with large number of bubbles.

c) It cannot be used for highly turbulent flow.

2- Cross Correlation:

One of the useful approaches to calculate the velocity in multiphase flow is to determine the displacement of some objects such as bubbles and waves between successive frames.

One application using cross correlation approach is calculating the velocity of the Taylor bubble in a slug flow based on changes of the bubbles coordinates as shown in Figure 2-6. For example, in the case of Taylor bubble, the tail of bubbles recorded in more than two frames, the final velocity corresponds to the average of each sequence pair [33]:

$$V_B = \frac{\Delta x_{Pix}}{NF}(Pix_s)(FR) \tag{2.13}$$

where V_B is the bubble nose velocity, Δx_{Pix} is the pixel difference computed between x position when elongated bubble enters and leaves the camera field of view, Pix_s is the pixel size and NF is the number of frames showing the bubble nose and FR is the frame rate.
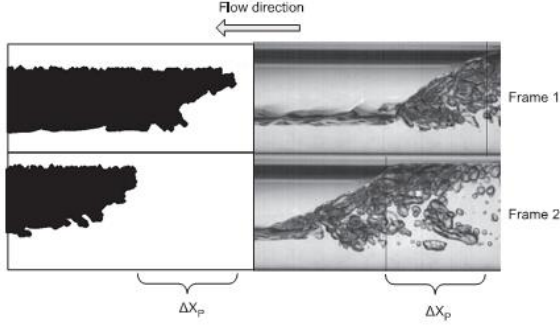
Figure 2-6: Determination of the bubble rear velocity based in the distance ΔX_P that tail moves between different frames. [33]

This technique may fail in some cases such as bubble breaking while the bubble is in the field of view of the camera or in the case of large number of dispersed bubbles at the rear. Image cross correlation is very promising technique to estimate the velocity. This method is utilized to determine Δx_{Pix} using cross correlation as shown in the following equation [33]:

$$R_{x_n y_n}(pTr) = \frac{Tr}{M}\sum_{c=0}^{M-1} x_I(c)y_I(c+p) \qquad (2.14)$$

where p is the shift in the number of frames and Tr is the time resolution and M is the number of images for which the cross correlation is calculated, I is the pixel index, $x_I(f)y_I(f+p)$ represent the numerical values associated pixel I from c^{th} image.

Using the cross-correlation, the value of Δx_{Pix} can be found by measuring the pixel distance between the peak of the signal and zero coordinate as shown in Figure 2-7.
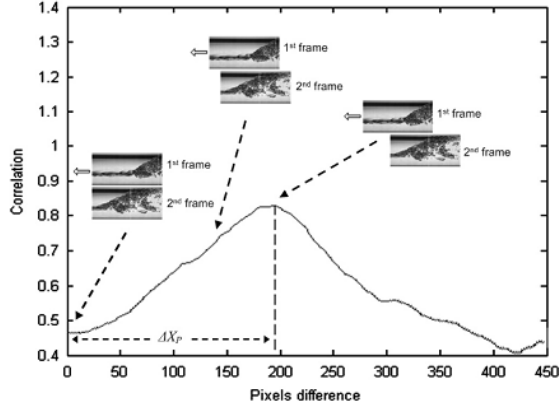
Figure 2-7 : Determination of the bubble rear velocity for JI= 1m/s and JG=1 through cross-correlation technique. [33]

More sophisticated approach in which a cross correlation between the two consecutive frames is calculated to determine the amount of displacement in the direction of flow as shown in Figure 2-8, [50].

The cross correlation between a template t and an image f is given by

$$R(u,v) = \frac{\sum_{x,y}[f(x-u,y-u)-\bar{f}_{uv}][t(x,y)-\bar{t}]}{\sqrt{\sum_{x,y}[f(x-u,y-u)-\bar{f}_{uv}]^2 \sum_{x,y}[t(x,y)-\bar{t}]^2}} \qquad (2.15)$$

where f is the image and $\bar{f}_{uv}$ is the mean value of f under the template, t is the template and $\bar{t}$ is the mean value of the template; u and v are the offset between the images.

The procedure returns a matrix R of the values of the correlation, from which the offset (u^*, v^*) in pixels corresponding to the peak of the correlation.

If three dimensional (3-D) objects can be constructed, then similar cross correlation function can be formulated as follow:

$$R(u,v,w) = \frac{\sum_{x,y}[f(x-u,y-v,z-w)-\bar{f}_{uvw}][t(x,y,z)-\bar{t}]}{\sqrt{\sum_{x,y}[f(x-u,y-v,z-w)-\bar{f}_{uv}]^2 \sum_{x,y}[t(x,y,z)-\bar{t}]^2}} \qquad (2.16)$$

Then, determine the peak displacement d as a fraction of the frame width. Then the velocity of the phase can be obtained as:

$$V(t) = \beta \frac{d(t)}{FW} FOV / t_{fr} \qquad (2.17)$$

where $d(t)$ is the displacement in pixels between frame at time t and frame at time t-1, FW is the Frame width in pixels, FOV is the field of view in meters (the physical width of the image in the pipe), and β is a calibration correction value to compensate for variability in FOV and t_{fr} is the frame period.
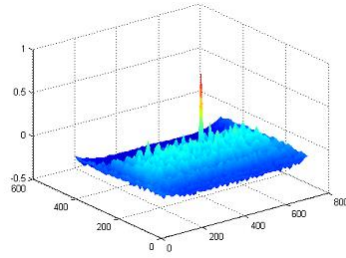
Figure 2-8: Image Cross Correlation function. [54]

Clearly, the image and *3D* cross correlation is different from signal cross correlation, which is used in the conventional flow meters. Signal cross correlation is only defined for time varying signals, while image cross correlation is performed primarily in two and three spatial dimensions.

For stratified wavy flow, which usually exists in horizontal pipelines, the wave velocity is called celerity. It is an important factor in stratified wavy flow analysis. The wave celerity is defined as the distance that wave crest travels per unit time [51]:

$$C = \frac{W_l}{t_W} \qquad (2.18)$$

where W_l is the wave length and t_W is wave period.

The celerity can be found using cross correlation between two frames to find the lag time between them, [52].

3. Particle Image Velocimetry (PIV):

PIV is an optical method used for flow visualization by finding instantaneous velocity measurements and related properties in fluids. It uses tracer particles seeded into the fluid. These particles are illuminated to become visible. Then motion of these particles is used to calculate speed and direction of the flow as shown in Figure 2-9. One of the main advantages of PIV is that it is not intrusive method. Particle Tracking Velocimetry (PTV) is another method to determine the velocity by tracking trajectory of the individual particles. In PIV, the mean velocity of a group of particles is determined while in PTV, the trajectory of each individual particle is tracked. So, PTV is used for low density image and PIV is used for medium density image. For high density images, there is another method called Laser Speckle Velocimetry (LSV), [53, 54, 55, 56, 57].

New PIV is able to handle few thousands of frame per second using of advanced visualization systems such as high speed CMOS camera, advanced laser system such as high repetition rate Nd:YAG (neodymium-doped yttrium aluminum garnet) and Nd:YLF (Neodymium-doped yttrium lithium fluoride) laser and Computer hardware with high speed processing units and large memory units , [53]. These improvement in PIV is helping in capturing more details for multiphase flow with high velocity such as annular flow**.**
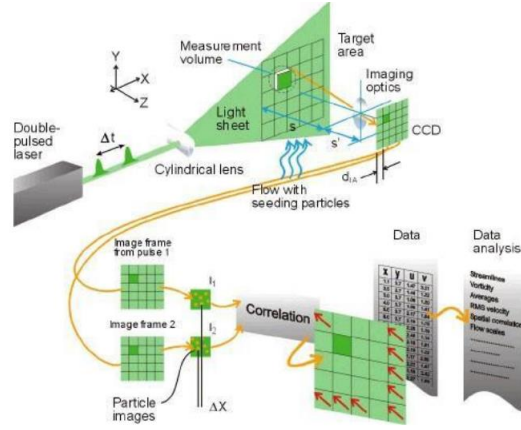
2.2.4 Bubble Length and Frequency

Special attention is given to big elongated bubbles or Taylor bubbles due to their effect on the process equipment specially the case of slug flow. By utilizing the velocity measurement and knowing the start and the end of the bubble, it is possible to calculate several bubble parameters such as bubble length, as shown in Figure 2-10 and frequency.

For bubble length, there are two cases [33]:

1- If the bubble length is smaller than the image size, in other word, the whole bubble fits inside the image, then the length of the bubble can be measured while the bubble is in the field of view and the final length is the mean value between the observed lengths.

2- If the bubble exceeds the frame length, then the bubble length can be calculated through the following equation:

$$l_B = Pix_s(X_{Ta} - X_N) + \left(\frac{V_B}{FR}\right)(NF) \tag{2.19}$$

where l_B is the bubble length, V_B is the bubble nose velocity, Pix_s is the pixel size, X_{Ta} is the horizontal position of the bubble tail, X_N is the horizontal position of the bubble nose,

29

FR is the frame rate, NF is the number of the frames showing the bubble body. From the above equation, it is possible to re-build the bubble shape through a series of pictures.
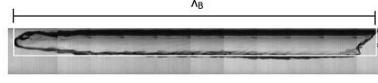
The slug unity frequency (Fre_{Unity}) can be found by the inverse of the time required to cross a specific section which is equal to bubble velocity divided by unity, which is bubble length plus slug length. The slug unit frequency is given by the following relation [24]:

$$Fre_{Unity} = \frac{V_B}{l_B + l_{Sl}}$$ (2.20)

where l_{Sl} is the slug length.

2.3 Limitations of Image Processing

There are some limitations of the image processing that need to be overcome to improve the accuracy of this approach. Six limitations will be discussed in this section: 3D-2D projection, overlapping, cylindrical to rectangular conversion, non-transparent fluids, and long processing time.

The first one is the 3D to 2D projection which may result in losing information. Lose of information due to projection is one of the common issues in the image processing, [58]. There are some assumptions used to deal with this issue. One of them is to assume that flow is symmetric, so, the view from one side is equivalent to other side, [31]. Another technique proposed for the case of ellipsoid bubble size is to assume that bubble extension in third

dimension is equal to the larger diameter of the ellipsoid. Finally, the bubble diameter can be calculated for a sphere with same volume, [35]. However, all of these techniques are not enough to have an accurate estimation of the actual case.

The best way to have an accurate estimation is by reconstructing the 3D image from 2D images. There are various ways to reconstruct the 3D image from its 2D projections. The simplest one is to use an additional orthogonal camera to reconstruct the 3D object as shown in the Figure 2-11 using the following procedure [50]:

Step 1: Use the image processing techniques to create a binary image of one class of objects from the top view camera.

Step 2: Use the image processing techniques to create a binary image of the same class of objects from the side view camera where the two images are synchronized.

Step 3: Extend the top view image and the side view image to 3D matrices by repeating the images.

Step 4: Turn the side view image.

Step 5: Multiply the two matrices to get the common pixels.

Step 6: Compute the size of the objects by summing up their pixels.
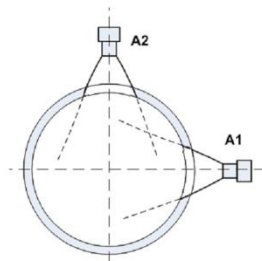
Figure 2-11: Use of two perpendicular cameras for 3D visualization [50]

The new version of wire mesh can be used for three phase flow using the electrical permittivity (capacitance) as a measured variable. Capacitance wire mesh is suitable for non-conducting fluid such as oil as shown in Figure 2-2 (e). Wiremesh sensor can be used also to reconstruct 3D image, [59, 60]. However, it is an intrusive method and cannot be used for unclean or sticky liquids such as crude oil.

More sophisticated techniques is the Tomography which is a non-invasive technique with high frame rate up to 10000 frames/s which helps in reconstructing accurate 3D images as shown in Figure 2-12. There are four types of tomography implemented for multiphase flow metering: X-Ray Tomography as shown in Figure 2-13, Electrical Capacitance Tomography (ECT), Gamma Ray and Microwave Tomography. Image reconstruction is usually done using computational methods known Computed Tomography. Several algorithms, such as minimum cross entropy, are used to make image reconstruction faster for online applications. Electric Tomography is cheaper, faster and safer than nuclear tomography but the latter has higher spatial resolution. The type of tomography depends also on application, e.g., ECT is used for non-conducting fluids such as oil, [61, 62, 63, 64, 65, 66, 67, 68].

Magnetic Resonance Imaging, which is used in medical application, can be used also to have 3-D images. The selection of scan protocol is important to have the required image characterizations. For example, spiral imaging scan protocol is selected for fluid flow application due to high temporal resolution and robustness, [69, 70].
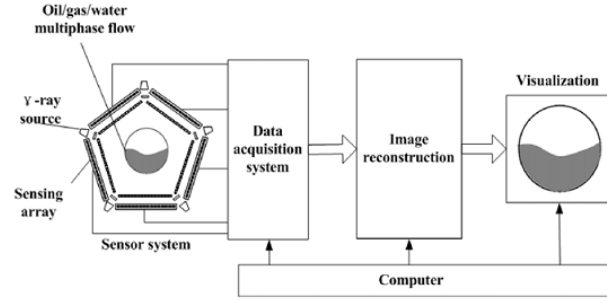
Figure 2-12: Computed Tomography [67].
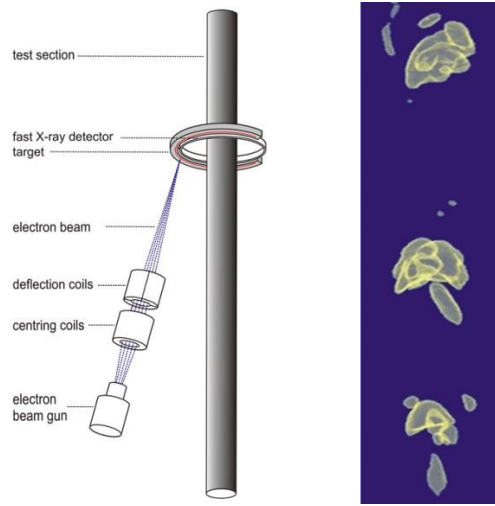
Figure 2-13: Operation principle of ultrafast electron beam X-ray CT [68].

The second limitation is objects overlapping (mainly bubbles) which can result in significant error. There are some proposed techniques to resolve overlapping issue such as object recognition and ellipse fitting. Watershed algorithm is one of the common techniques used to correct the overlapping. An example of overlapping correction using watershed algorithm is shown in Figure 2-14 [71]:

1- Bubbles objects are separated into two groups: Solitary bubbles and Overlapping Bubbles. Classification is done using the following roundness formula:

$$Ro = \frac{S}{\sqrt{4\pi A}} \tag{2.21}$$

33

where S is the object perimeter and A is the area. The object is classified as a solitary bubble if $Ro < 1.25$.

2- Apply water-shedding algorithm to perform segmentation of overlapping objects.

3- Combine the solitary bubbles and overlapping bubbles after segmentation into one image again.
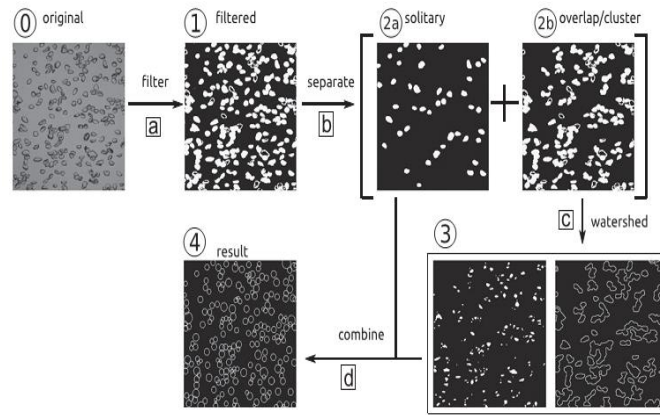
Figure 2-14 : Solving the overlapping process [71].

However, these methods assumes bubbles are either spherical or ellipsoidal which has a limited validity in actual flow conditions. So, there is a need to develop efficient algorithms that can deal with overlapping issue for bubbles with non-uniform shape to have more accurate estimation of the bubble size distribution and estimation of the gas hold up in case of objects overlapping.

Another source for the information loss is the cylindrical to rectangular conversion due to pipe curvature if some enhancement techniques are used such as using optical rectangular box with flat walls around the pipe, [31]. This box can be filled with water to reduce the image distortion results from light source as shown in Figure 2-15, [33].
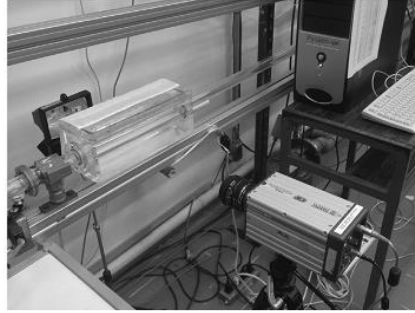
Another limitation is that some fluids such as Crude Oil is not transparent with visible light which makes the use of camera with traditional lighting sources limited. There are some technologies that can may be used to overcome the illumination issue such as laser light [28], Near-Infrared with CCD camera [72] and Particle Video Microscope, [73].

Finally, processing time for multiphase flow analysis is very long which limits the use of image processing for online applications. To overcome this limitation, it is recommended to use parallelization scheme in which multi-processors are used in parallel with pool of shared memory. Graphical Processing Unit (GPU) is a massive multicore processors component that can be considered as one type parallelization scheme. However, in order to use parallelism scheme, the algorithm must be designed carefully to interact correctly with GPU, [74, 75].

Conclusion

Image processing is very promising tool for multiphase flow parameters estimation. It reduces the dependency on the flow patterns identification. In the last few years, there has been growing interest in using the image processing to estimate multiphase flow parameters. Several techniques have been developed for multiphase flow analysis using

image processing. However, there are some limitations that must overcome to improve the accuracy of these techniques without using sophisticated systems. In addition, classical image processing techniques are not enough to have an accurate result. There is a need to combine these techniques with artificial intelligence techniques and advanced computer vision algorithms to have more robust and accurate estimation. Moreover, combining image processing with Artificial Intelligence (AI) can extend this method not only to estimate multiphase parameters but also it can be used to estimate more multiphase flow features such as identifying the flow patterns types using the extracted parameters from image processing. Careful attention should be given to vision system to improve the quality of the image which is a key factor in this approach and make it possible to be used in difficult situations such as crude oil case.

CHAPTER 3

IMAGE PRE-PROCESSING

Before performing the multiphase flow analysis, there is a need to perform some operations to enhance the image quality and prepare it for analysis and finally extract the features. There are various techniques proposed to normalize the image. The appropriate pre-processing techniques are selected based on several factors such as flow environment and vision system used. Figure 3-1 shows some of these steps for the bubbly flow case, [76, 36, 77, 30].
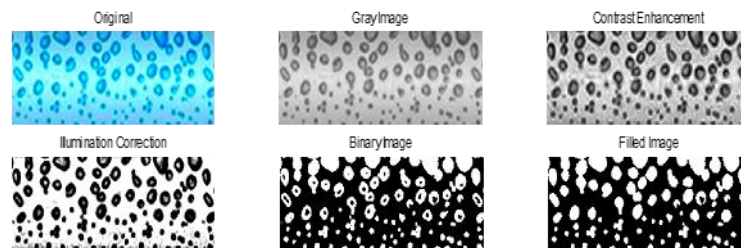
Figure 3-1: Common Image preprocessing.

Common image pre-processing steps are:

3.1 Image color conversion

There are several algorithms used to convert color image, RGB (Red, Green, and Blue) to gray image. Three common algorithms are briefly explained below [78]:

1. Lightness: This approach averages the most prominent color and least prominent color

   (Max (R, G, B) +Min (R, G, B))/2.

2. Average: This approach averages the three colors

   (R+G+B)/3.

3. Luminosity: This is the most accurate approach for converting color image to gray image. It gives a weight to each color: $w_1R+w_2G+w_3B$. The biggest weight is usually given to green because our eyes are more sensitive to green.

3. 2 Contrast Enhancement

It is very useful to improve the identification process of boundaries between liquid and gas phases. Two main algorithms used for contrast enhancement:

3.2.1 Histogram Equalization

It is a method used to improve the image contrast by adjusting the image intensities. Let f be the input image , then, the normalized histogram $Hist$ can be calculated as follow [36, 77]:

$$Hist(in_{input}) = \frac{number\ of\ pixel\ with\ intesity\ in}{total\ number\ of\ pixels} \qquad , in = 0, 1, ..., Li - 1 \qquad (3.1)$$

where in_{input} is the input intensity.

The output intensity value, in_{out} , can be defined as:

$$in_{out} = Tran(in_{input})) \qquad (3.2)$$

where in_{out} is the output intensity and Tran is a transformation function.

This is equivalent to transforming the pixel intensity in_{input} by the following transfer function:

$$Tran(in_{input}) = floor((Li - 1)\sum_{e=0}^{n} p(in_{input_e})) \qquad (3.3)$$

where Li is the number of possible intensity values (for gray image Li=256), floor is a function to round the values to the nearest integer.

There is a better version of the histogram equalization called contrast-limited adaptive histogram equalization (CLAHE) which operates on small regions rather than entire image, [79].

3.2.2 Contrast Stretching

It is simpler than histogram equalization because it applies a linear scaling function to the image pixel values. It results in less harsh enhancement. The formula used for that is shown in the equation below:

$$in_{out} = \left(in_{input} - f_{in_{max}}\right)\left(\frac{in_{max} - in_{min}}{f_{in_{min}} - f_{in_{max}}}\right) + in_{min} \qquad (3.4)$$

where a and b are the lower and the upper limits of the pixel intensity values in the image type, respectively. For gray image $in_{min}=0$, $in_{max}=255$. $f_{in_{min}}$ and $f_{in_{max}}$ are the lower and upper limit of pixel values in the current image, respectively. in_{input} is the pixel intensity value before treatment and in_{out} is the pixel intensity value after stretching, [58, 80, 81].

3.3 Illumination Correction

There is needed to compensate for the non-uniform illumination in the image. This process is based on background subtraction by assuming homogenous background and the objects are brighter or darker than the background, [82].

There are two approaches in the non‑uniform illumination correction:

3.3.1 Prospective Correction

Prospective approach uses several captured images at the same time and utilize them to correct the illumination. These additional images can be dark image (background with no light) or bright (Background with light but not objects). For example, if both bright image and dark image are available, the corrected image $g(x_{im}, y_{im})$ can be obtained using the following formula:

$$g(x_{im}, y_{im}) = \frac{f(x_{im}, y_{im}) - d(x_{im}, y_{im})}{b(x_{im}, y_{im}) - d(x_{im}, y_{im})} . NC \tag{3.5}$$

$$NC = mean(f(x_{im}, y_{im})) . \frac{1}{mean(\frac{f(x_{im}, y_{im}) - d(x_{im}, y_{im})}{b(x_{im}, y_{im}) - d(x_{im}, y_{im})})} \tag{3.6}$$

where $d(x_{im}, y_{im})$ is the dark image, $b(x_{im}, y_{im})$ is the bright image, NC is the normalization constant.

3.3.2 Retrospective Correction

Retrospective approach is used when additional images are not available. It first estimates the bright image then uses background subtraction approach to get the correct image. Several algorithms had been developed using this approach. For example, Low Pass Filtering (LPF) with high kernel can be used to estimate the background. Then, the estimated background is subtracted from the input image to correct the non-uniform illumination. So, the corrected image $g(x_{im}, y_{im})$ is given by:

$$g(x_{im}, y_{im}) = f(x_{im}, y_{im}) - LPF(f(x_{im}, y_{im}))$$
$$+ mean(LPF(f(x_{im}, y_{im}))) \tag{3.7}$$

3. 4 Conversion to Binary Image

This step is required to label the liquid phase and gas phase. In order to label the two phases, it is required to identify the threshold to classify the areas to either liquid or gas,

[36 ،77]. Two common image thresholding approaches are used: Global Thresholding and Variable (Adaptive) Thresholding.

3.4.1 Global Thresholding

This approach uses a single threshold value to segment the image into different regions. Global thresholding can be divided into four categories:

Basic Thresholding: It uses a simple thresholding function which can be defined as follow:

$$g(x_{im}, y_{im}) = \begin{cases} 1 & if\ f(x_{im}, y_{im}) > Th \\ 0 & if\ f(x_{im}, y_{im}) < Th \end{cases} \tag{3.8}$$

where, $f(x_{im}, y_{im})$ is the input image, $g(x_{im}, y_{im})$ is the segmented image, Th is the threshold value, [36, 77, 58].

Optimum Thresholding (Otsu's Method): Thresholding value is determined using statistical decision theory, [36, 77, 83]. It may fail in presence of noise.

a. Image Smoothing: It produces a histogram with separated peaks and it can handle noisy images because smoothing process removes the high frequencies which is basically the noise. However, if the distribution of the gray levels in the histogram is not balanced, the smoothing approach may not be able to extract useful information from the histogram, [36, 77].

b. Edges Extraction: Considering the pixels that on or near the edges which reduces the dependency on the relative size of the objects and background, [36, 77].

3.4.2 Variable Thresholding (Adaptive)

Variable thresholding approach is recommended in case of a non-uniform illumination. There are two main approaches of adaptive thresholding:

a. Image partition: it subdivides the image into several regions, usually rectangles. Then, a threshold value for each region is determined independently which mitigates non-uniform illumination effect. This method works well if the object and background occupy regions that have comparable sizes, otherwise it will fail, [36, 77].

b. Variable thresholding: it utilizes the local image properties to compute a thresholding value at every point. Mean and standard deviation of the neighborhood pixels of the point are two possible quantities that can be used to compute the thresholding value. This type of thresholding is suitable for multiphase flow case, which may have many noise sources especially in outdoor environments, [36, 77].

However, adaptive thresholding requires longer processing time than global thresholding. In order to reduce the processing time, several algorithms had been developed such as Bradley and Roth [84] and Sauvola and Pietikainen [85] which utilized the concept of integral image to reduce number of iterations during processing of the image. There are many adaptive thresholding techniques used for image segmentation and they are depending on different principles to find local threshold and their performance may vary from application to another based on the purpose for which they are formulated. In the following section, a brief description of six techniques will be given to explain how adaptive algorithms work to segment the image.

1- Nilback Technique

Nilback technique uses local variance techniques to determine the local threshold. Threshold value is calculated based on the mean $m(x, y)$ and the standard deviation $\sigma(x, y)$ within window size wxw by the following formula:

$$Th(x, y) = m(x, y) + k\sigma(x, y) \tag{3.9}$$

where k is the bias controlling the adaptation level that varies threshold value.

In this method, the local mean $m(x, y)$ and the standard deviation $\sigma(x, y)$ adapt the threshold value based on the contrast in the local neighborhood area of the pixel, [86].

2- Sauvola Technique

Another local threshold technique that uses local variance is called Sauvola which is a famous method to calculate the local threshold in the image. Basically, the image is divided into small window size w×w, then using the mean $m(x, y)$ and standard deviation $\sigma(x, y)$ of the pixels within this window, the threshold Th(x, y) can be calculated using the following formula:

$$Th(x, y) = m(x, y) \left[1 + k \left(\frac{\sigma(x,y)}{Rd} - 1 \right) \right] \qquad (3.10)$$

where Rd is the dynamic range of the standard deviation (for gray image Rd=128) and k is a bias, which takes positive values in the range [0.2, 0.5].

Similar to Nilback technique, the local mean $m(x, y)$ and the standard deviation $\sigma(x, y)$ work to adapt the threshold value based on the contrast in the local neighborhood area of the pixel but the difference is that Sauvola can tackle the case of high contrast and low contrast, [85].

3- Guanglei Xiong Statistical Thresholding Technique

Guanglei Xiong uses the mean or median of the surrounding pixels to determine the local threshold within window size w x w. Setting the threshold in local area as the mean or median can work if there is clear contrast between foreground pixel and background pixels. The mean value lies between the intensity values of the foreground and background pixels but if the range of intensity values inside a local neighborhood is very small, it will not work and their mean value is close to the value of the center pixel.

Small modification is done to this techniques to overcome this limitation by subtracting a constant value C from the mean or the median. So, the threshold value Th can be either Th= mean- Constant or Th= median- Constant.

With this improvement, all pixels that lie inside a uniform neighborhood are set to the background which, in turn, reduces the segmentation error, [87].

4- Bernsen Technique

Bernsen technique uses the local gray range technique to determine local threshold. In Bernsen technique, threshold value is set to the mean of maximum and minimum gray values within the local window of size w×w as follow:

$$Th(x,y) = 0.5(in_{\max(i,j)} + in_{\min(i,j)}) \tag{3.11}$$

where $in_{\max(i,j)}$ and $in_{\min(i,j)}$ are maximum and minimum gray values (intensity value) within the local window, provided that contrast

$$Cont(i,j) = in_{\max(i,j)} - in_{\min(i,j)} \geq 15 \tag{3.12}$$

However, Bernsen technique does not work properly when the contrast is less than 15, in other word if the contrast value is very low, [88].

5- Bradley Technique

Bradly algorithm is started first by calculating the average of pixels which is centered around each pixel. Then, pixel value is set to black if its brightness is a lower with certain percent than the average brightness of the surrounding pixels in the window of the specified size, otherwise it is set to white.

Bradley's method calculates just local mean while Sauvola method calculate both local mean and local variance which make Bradley faster than Sauvola method. Bradley's method calculate variance using local mean by the following formula:

$$Var(x) = m(x^2) - [m(x)]^2 \tag{3.13}$$

The result from the calculation of the local mean (m(x))^2 is reused and just calculates m(x^2), [84].

6- Energy Technique

Another approach for local thresholding is based on minimizing an energy functional called Variational Minimax algorithm. The algorithm is a non-linear convex combination of the data fidelity and the regularization terms in the energy functional which seeks for the optimum threshold surface using minimax principle.

The energy functional can be formulated as follow:

$$E(Th; \alpha) = \sqrt{1 - \alpha i^2} E_1(Th) + \alpha i E_2(Th) \qquad (3.14)$$

where:

$$E_1(Th) = \frac{1}{2} \iint g(x, y)(f(x, y) - Th(x, y))^2 \, dxdy \qquad (3.15)$$

$$E_2(Th) = \frac{1}{2} \iint |\nabla Th(x, y)|^2 \, dxdy \qquad (3.16)$$

$$g(x, y) = \frac{|\nabla f(x,y)|^{qi}}{\max(|\nabla f(x,y)|^{qi})} \qquad (3.17)$$

where αi is weighting parameter$\in [0,1]$, qi is selected generally as 2 to describe the gradient strength of the image, [89]

One representative frame is illustrated in Figure 3-2, to show the performance of various thresholding algorithms.
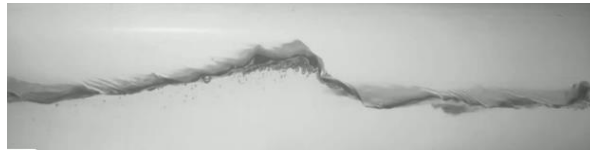
Figure 3-2: Wavy Flow sample. [90]

As shown in Figure 3-3 (a, b) Global threshold could not compensate for non-uniform illumination and it is does not estimate the mix region correctly. Also, Global threshold

could not provide an accurate continuous wave boundary which leads in wrong estimation of liquid and gas hold up.

The performance of adaptive thresholding algorithms were examined for image segmentation. Nilback technique completely failed because it could not handle low contrast images as shown in Figure 3-3 (c, d). Sauvola technique is able to compensate for non-uniform illumination, estimates wave shape and segments the image properly and shows clear boundary between two phases as shown in Figure 3-3 (e, f). Similar results are achieved by Bradley but it could not compensate for nonuniform illumination at the frames edges as shown in Figure 3-3 (m, n). Also, Guanglei Xiong shows very good performance as shown in Figure 3-3 (g, h) using mean and Figure 3-3 (i , j) using median . Bernsen was not able to compensate for non-uniform illumination as global technique but it provides better estimation for the wave shape as shown in Figure 3-3 (k, l). Energy method is able to compensate for non-uniform illumination and good estimation for wave shape.

Segmentation Method	No	Binary Image	No	Layer Edges
Global	a		b	
Nilback	c		d	
Sauvola	e		f	
Guanglei Xiong-Mean	g		h	
Guanglei Xiong-Median	i		j	

Bernsen	**k**		**l**	
Bradly	**m**		**n**	
Energy	**o**		**p**	

Figure 3-3: Image Segmentation performance comparison

In general, the adaptive thresholding techniques have better performance than global thresholding ones. However, the price of this accuracy is the processing time needed to perform the thresholding. Table 3-1 shows the average processing time for global and adaptive thresholding techniques. It is clear that adaptive thresholding requires much more time than global thresholding.

Table 3-1: Average Processing Time.

No	Segmentation Method	Average Processing Time
1	Global	0.000861seconds
2	Nilback	0.153589 seconds
3	Sauvola	0.02916 seconds
4	Guanglei Xiong -Mean	0.025024seconds
6	Guanglei Xiong-Median	1.53761 seconds
7	Bernsen	0.058922 seconds
8	Bradly	0.014323 seconds
9	Energy	1.449521 seconds

3. 5 Multi-Level Thresholding /Color Thresholding

Binary thresholding is not enough to characterize the case of three phase flow, e.g. Oil/Gas/Water. For multiphase flow, it is recommended to use multi-level thresholding or color thresholding to identify the features of each phase. To perform color thresholding of RGB (Red, Green, and Blue) image, red and green and blue values of the pixel are determined first. Then, a threshold range for each color plane is selected to encompass each color pixel values.

However, RGB thresholding can achieve incorrect image segmentation when the color range is diverse. Alternative approach is to use HSV (Hue, Saturation, and Value) or HSL (Hue, Saturation, Luminance) where Hue plane have the main information of the image as shown in Figure 3-4.

| Hue Plane Histogram | Saturation Plane Histogram | Luminance Plane Histogram |
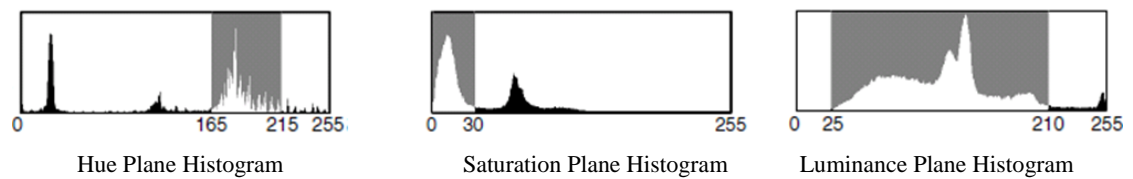
Figure 3-4: HSV Color Model Histograms [45].

HSV/HSL thresholding is done by determining the Hue value of the pixels, then determine the saturation values associated with Hue value if needed. Finally, Luminance value which usually have little information will be determined, [83, 91].

Figure 3-5 shows an example of application HSV/HSL color model to threshold a color image of multiphase flow.

Original Color Image   Hue Channel Image   Saturation Channel Image   Value Channel Image

Histogram of Hue Image   Histogram of Saturation Image   Histogram of Value Image

Binarized Hue Channel Image
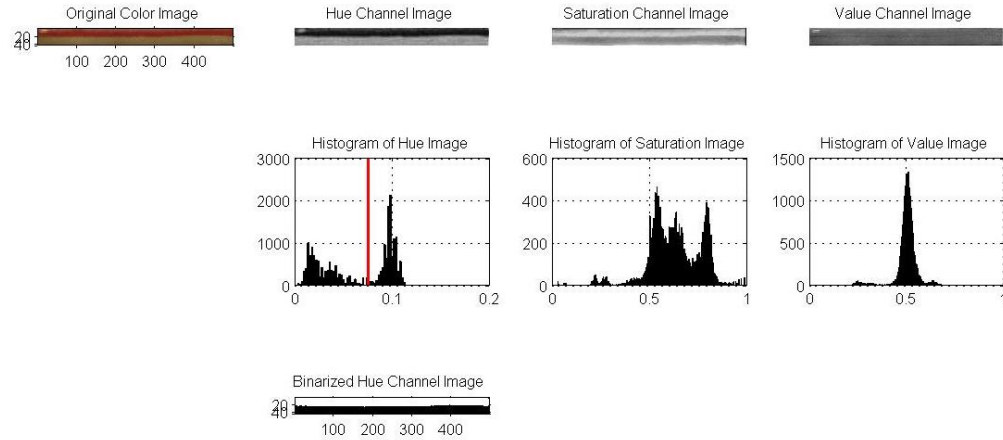
Figure 3-5: Hold up determination using HSV Color Model.

3. 6 Filtering

Image filtering process is necessary to remove the noise from the image. There are various filtering techniques implemented such as low pass filter which is used to smooth the image, and median filter which is effective in removing salt and pepper compress the image without losing any information, [36, 77]. Wavelet filters is also very promising filtering technique in image processing, [92].

3.7 Morphological Operations

These are nonlinear mathematical operations which are related to the shape or morphology of some features in the image. These operations are used to enhance the image and extract features such as holes, filling inside objects and boundaries extraction. Dilation and Erosion are the two basic morphological operations. Dilation allows the object to expand which is useful to fill small holes and connect disjoint objects. Erosion allows the object to shrink by eroding their boundaries. Dilation and Erosion can be combined into more complex operation opening and closing. Opening operation which is erosion followed by dilation,

49
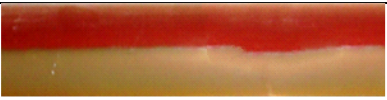
allows to remove unwanted small objects, while closing operation, which is dilation followed by erosion, allow to fill small holes and gaps. These operations are important to identify the bubbles shape and size and fill the gaps in the object boundaries, [36, 77, 93].

3. 8 Image Resize

Image size reduction is recommended to reduce the processing time. There are some algorithms to reduce the image size by cropping the frames such as minimum bounding box, [31] .

3.9 Image Retouching

This process is usually called inpainting which is used to remove the defects in the image and reconstruct it using the information from the surrounding pixels as shown in Figure 3-6. In multiphase flow, these defects include light reflection on the pipe and defects on the pipe due to aging. There are two types of inpainting: Structural inpainting and Texture inpainting. Structural inpainting implement geometric approaches to restore the missing parts while Texture inpainting deals with texture parts. Since most of the images today has both structure and texture, the best practice is to have simultaneous structure and texture inpainting, [94, 95].

No	Original	Corrected
1		
2		

3		
4		
6		
7		

Figure 3-6: Light Reflection Correction.

CHAPTER 4

MULTIPHASE FLOW FACILITY

4.1 Facility Description

The conducted air -water experiments were performed in the "Research Institute" building at the King Fahd University of Petroleum and Minerals. The multiphase flow setup was constructed for two and three phase flow experiments. The setup is shown in Figure 4-1. It consists of two tanks for oil and water, two pumps for each fluid, a pipe with a test section, two separation tanks that are attached at the end of the test tube, a return pump close to the separation tanks, and an air compressor. The tanks have a 1.25 m inner diameter, and a 1.6 m height, and the pumps have a 3.5 hp capacity. The pumps can deliver oil or water with a maximum velocity of 3 m/s. Also, they can deliver oil and water together with a 3 m/s mixture velocity. A Y-shaped mixing section shown in Figure 4-2 joins the oil and water pipes to the test section which has a 2.25 cm diameter. The pipes are made of PVC. The last section of the pipe was made of a transparent Plexiglas for visual observation. The velocity range of the conducted experiments was from 0.05 m/s to 3 m/s. In this work, we conduct the experiments for two phases only: air and water.
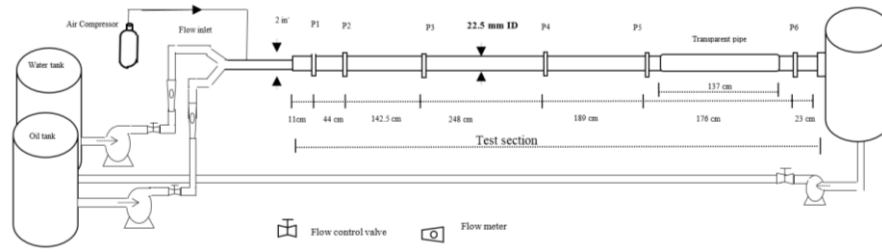
Figure 4-1: Schematic Representation of the Experimental Setup.

Figure 4-2: Picture of the Y-shaped joining section.

4.2 Test Section

The test section for flow visualization is shown in Figure 4-3. The pipe is made of PVC with ASTM D-1785 standard number and a 2.25 cm inner diameter. The pipe was installed horizontally. It contains of two sections, one section is a PVC pipe, used for pressure readings, and the other is transparent made of Plexiglas for visual observation, which is used for flow pattern capturing. The total length of the test section is 8 meters as can be seen in Figure 4-3. Pressure outlets are distributed along the pipe where the

53

differential pressure transducer and manometers are attached. A picture of the transparent section of the pipe is given in Figure 4-4.

Pressure drop was taken between P4 and P5 using water manometer. The pipe length to diameter ratio until P4 is 200; this ratio is taken from the start of the test section until point P4.
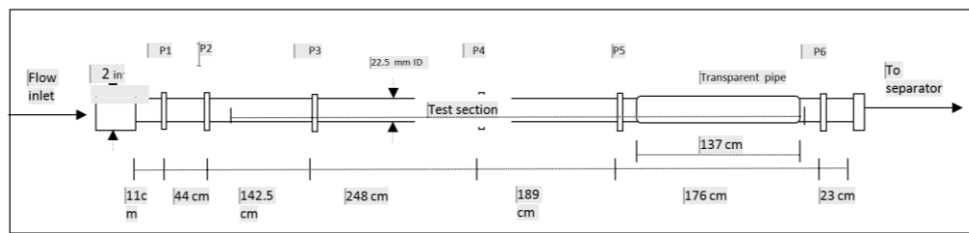
Figure 4-3: The Test Part of the Setup.

Figure 4-4: Picture of the transparent part of the test section, 22.5 mm ID.

4.3 Vision System

To capture the features of the fast moving flow, a high speed camera is needed. The camera used in this work is from SpeedSense 900xx series high speed camera made by Vision Research shown in Figure 4-5.

Specifications of the camera is shown in Table 4-1. Resolution and frame rate can be changed based on the user requirements. These setting should be selected to capture the required details from flow but not higher than needed to avoid unnecessary processing work and time and avoid extra storage space.

Table 4-1: High Speed Camera Specifications.

Model	Maximum Resolution (Pixels)	Bit Depth	Maximum Exposure Time (µs)	FPS	Pixel Size (micron)
9040	1632×1200	8 ,12 ,14	2	1016 /508	11.5

For the experiments performed in this research, the following settings were used:

1- Resolution: 1280×720 pixel.

2- Frame Rate: 900 FPS.

3- Bit Depth: 8 bits.

The capture video is converted to frames using image processing toolbox in MATLAB R2015b software and all analysis were performed on the frames , but keeping the same sequential order.

CHAPTER 5

FLOW FEATURES EXTRACTION AND ANALYSIS

After discussing the image pre-processing operations, we will start to extract and investigate the following multiphase flow features for stratified wavy flow which is a common flow pattern in the pipelines and there is a need to be investigated using image processing. These features are Wave Velocity (Celerity), Wavelength, Wave Frequency, Wave Period, Wave Amplitude and Hold up.

5.1 Experiments

There are several experiments were conducted for Stratified Wavy flow pattern with different conditions as shown in Table 5-2 and Table 5-3. The first set of experiments had been done for two phases water and air without drag reducing polymer (DRP). The flow rate of liquid is increased from 0.000141 m^3/s in case 1 up to 0.000170 m^3/s in case 5. Similarly for the second set of the experiments, the liquid flow rate is increased between cases but with addition of a drag reducing polymer (DRP) to the flow with different concentration at each case as shown in Table 5-3 in order to evaluate the effect of polymer in stabilizing flow. The polymer utilized in this work is a synthetic high molecular weight polyacrylamide and it was supplied as a free flowing white powder. Table 5-1 shows specifications of the selected water-soluble polymer as obtained from the manufacturer. Liquid superficial velocity shown in Table 5-2 and Table 5-3 is calculated using the following formula:

$$V_{SL} = \frac{q_L}{A_p} \qquad\qquad (5.1)$$

where q_L is liquid flow rate and A_p is the cross sectional area of the pipe.

Table 5-1: Physical Properties of ZETAG® 8165 (water soluble polymer)

Properties	Description
Product Name	Polyacrylamide (PAM)
Appearance	Off-white granular solid
Molecular Weight	High
Particle Size	98% < 1750 microns
Bulk Density	0.7 g/cm^3
PH of 0.5% solution	Approx. 3.5
Shear rate	5.11 (1/sec)
Page weight	25 kg of DRP.
Solubility	Water-soluble

Table 5-2: Experiments conditions without Drag Reducing Polymer.

Case No	Liquid Flow Rate (m^3/s)	Gas Flow Rate (m^3/s)	V_{SL} Calculated (m/s)	DRP Concentration (PPM)
1	0.000141	0.0032	0.29	0
2	0.000149	0.0032	0.30	0
3	0.000157	0.0031	0.32	0
4	0.000166	0.0032	0.34	0
5	0.000170	0.0031	0.35	0

Table 5-3 : Experiments conditions with Drag Reducing Polymer

Case No	Liquid Flow Rate (m^3/s)	Gas Flow Rate (m^3/s)	V_{SL} Calculated (m/s)	DRP Concentration (PPM)
1	0.000136	0.0032	0.28	13.21
2	0.000139	0.0032	0.28	44.48
3	0.000143	0.0033	0.29	73.86
4	0.000148	0.0032	0.30	101.24
5	0.000156	0.0033	0.32	151.83

| 6 | 0.000161 | 0.0032 | 0.33 | 174.85 |

5.2 Wave Velocity (Celerity)

Wave Velocity Celerity C is defined as the distance the wave travels per unit time

$$C = \frac{d}{t} \qquad (5.2)$$

d is the distance and t is the time.

To estimate the value of the celerity, the following operations are performed:

1. Frame cropping to reduce the size of the image and make the analysis around the liquid-gas interface.

Figure 5-1: Cropped Original Frame

2. Each frame is converted to binary image using Sauvola adaptive thresholding technique.

Figure 5-2: Binary Image

3. All other small objects are removed.

4. The binary image is complemented to convert the mix region from black to white.

5. All other small objects are removed.

6. The boundary of the mixed region is extracted using the morphological operations:

   a. Create a structuring element.

   b. Erode the image with a structuring element.

   c. Subtract the eroded image from the original image.

   d. Contour of the image boundaries is traced using More-Neighborhood trace

   algorithm.
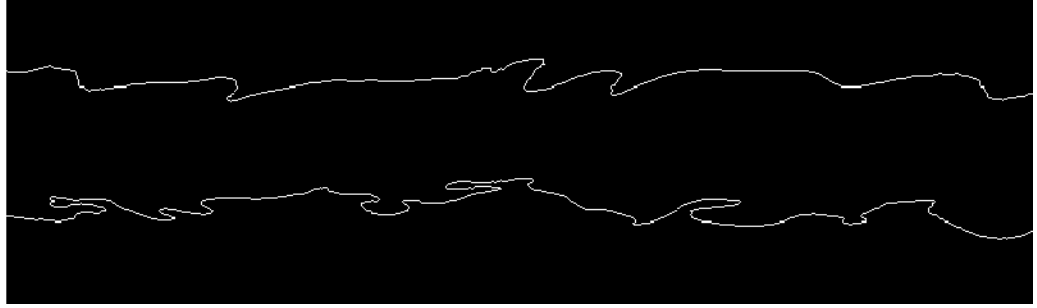
Figure 5-6: Extracted boundary

7. Then, the upper boundary of the mixed region, which is the interface between liquid phase and gas phase is extracted. If there are more than one value of y axis, the maximum of them is taken.
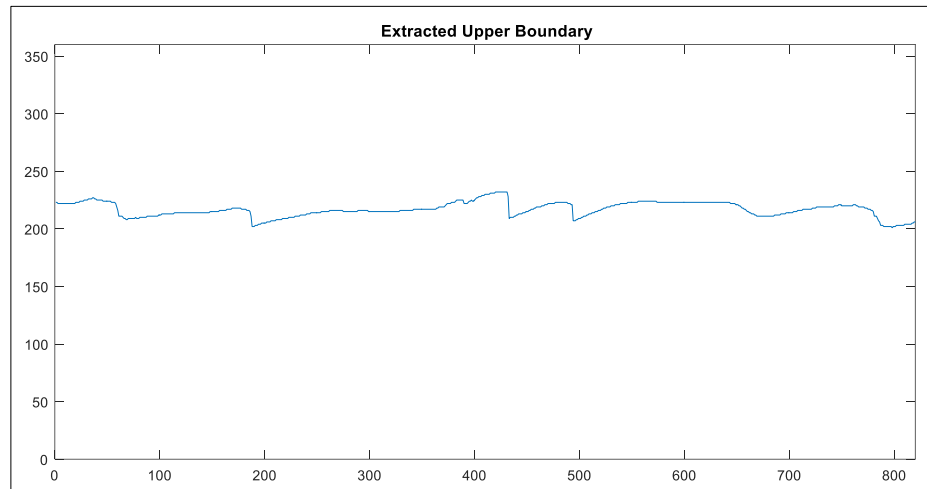
Figure 5-7: Upper Boundary

8. The extracted boundary can be used to estimate the wave velocity, which can be estimated by fining the similarity of the extracted boundaries of the subsequent frames. The recommend technique to achieve this target is the signal cross correlation to find the distance shift. Suppose that we have two extracted boundaries x (n) and y (n+l), the cross correlation coefficient between these two signals r_{xy} can be defined as:

61

$$R_{xy}(l) = \sum_{n=-\infty}^{\infty} x(n)y(n+l) \quad , l = 0, \pm 1, \pm 2, \cdots \qquad (5.3)$$

9. Before performing the cross correlation, the extracted boundaries values is
    normalized using the following formula:

$$x(n)_{normalized} = (x(n) - mean(x(n)))/\max(abs(x(n))) \qquad (5.4)$$

10. In our calculation, we use cross correlation to estimate the distance that wave
    travels between subsequent frames. The distance shift is corresponding the
    maximum correlation value.
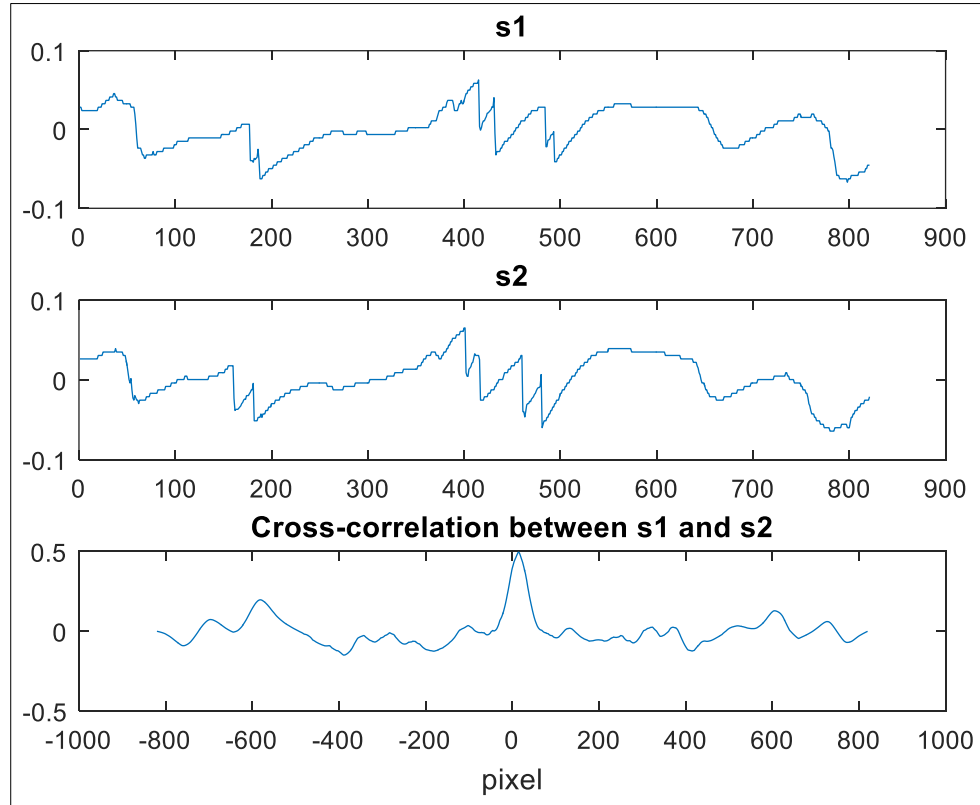
Figure 5-8: Cross correlation between two signals.

11. The estimated distance shift (Δ d) from step is in pixel, so, we need to convert to
    meter. This can be done using the following formula:

$$\Delta \textbf{ d (Meter)} = \Delta \textbf{ d (Pixel) x FOV (Meter) /FW (Pixel)} \qquad (5.5)$$

where FOV is the field of view and FW is the Frame Width.

12. Celerity (C) can be calculated using the following formula:

$$C = \Delta\,\mathbf{d}\,(\mathbf{Meter})\ *\mathbf{FR/NF} \tag{5.6}$$

where FR is the frame rate per second and NF is the number of frames used (NF

=1 in this work since we used consecutive frames)

Since cross correlation is a statistical method, the above procedure is repeated for many frames. Cross correlation sometimes produces outliers which is not considered in the calculation. After removing the outliers, the celerity value is equal to the average value of the calculated celerities between subsequent frames. The estimated celerity values for both non-polymer and polymer experiment are shown in Table 5-4 and Table 5-5. As shown in Table 5-5 , the celerity values increase by adding the polymer to the liquid . The results are compared with PIV flow profile that have been taken from parallel experiments having same flow conditions. The comparison is done by comparing the last value near water –air interface read by PIV with celerity value taken around the interface. For non-polymer case, there is a good match between the two techniques as shown in Figure 5-9 . For polymer case, there is a clear difference between them as shown in Figure 5-10. Cross correlation technique have a larger values for the celerity than non-polymer case while the PIV has lower value non-polymer case although the superficial velocity increases by adding the polymer to liquid as shown in Table 5-6. When we look to the flow in video, we found that there are bubbles around the water-air interface that move with slower velocity than interface. The seeding particles are disturbed by these bubble and move with slower velocity which may explain the difference between PIV and cross correlation for polymer case. The standard deviation of the celerity is quite high mainly due to actual flow fluctuation.

Table 5-4: Celerity Values for non-polymer experiments

	Celerity Values					
	Case 1	Case 2	Case 3	Case 4	Case 5	Ave all
Ave	0.574	0.630	0.708	0.713	0.742	0.673
STD	0.185	0.183	0.248	0.229	0.268	0.223

Table 5-5: Celerity Values for polymer experiments

	Celerity Values						
	Case 1	Case 2	Case 3	Case 4	Case 5	Case 6	Ave all
Ave	0.766	0.785	0.917	0.808	0.750	0.924	0.825
STD	0.268	0.268	0.322	0.331	0.268	0.311	0.295

Table 5-6: Comparison between Cross Correlation and PIV

	Without Polymer				With Polymer		
	Cross Correlation	PIV	Error %		Cross Correlation	PIV	Error %
Case 1	0.574	0.607	5.46		0.766	0.467	-63.96
Case 2	0.630	0.66	-4.55		0.785	0.53	-48.19
Case 3	0.708	0.54	-31.03		0.917	0.64	-43.31
Case 4	0.713	0.72	0.97		0.808	0.59	-37.03
Case 5	0.742	0.737	-0.63		0.750	0.75	-37.85
Case 6					0.924	0.544	-57.46
Ave	0.673	0.6528	-5.956		0.825	0.587	-37.55
STD	0.223				0.295		
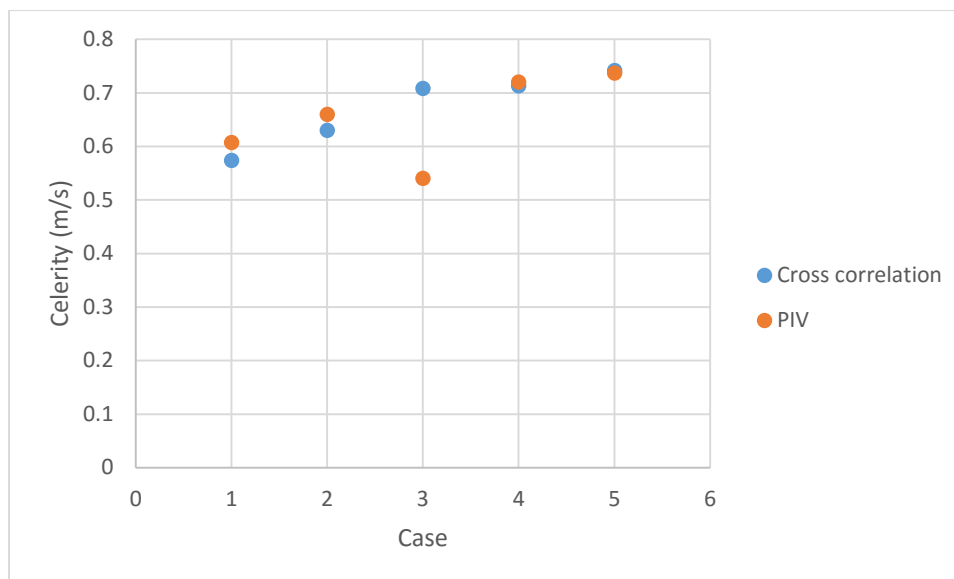
Figure 5-9: Celerity values taken by PIV and Cross correlation for non-polymer experiments
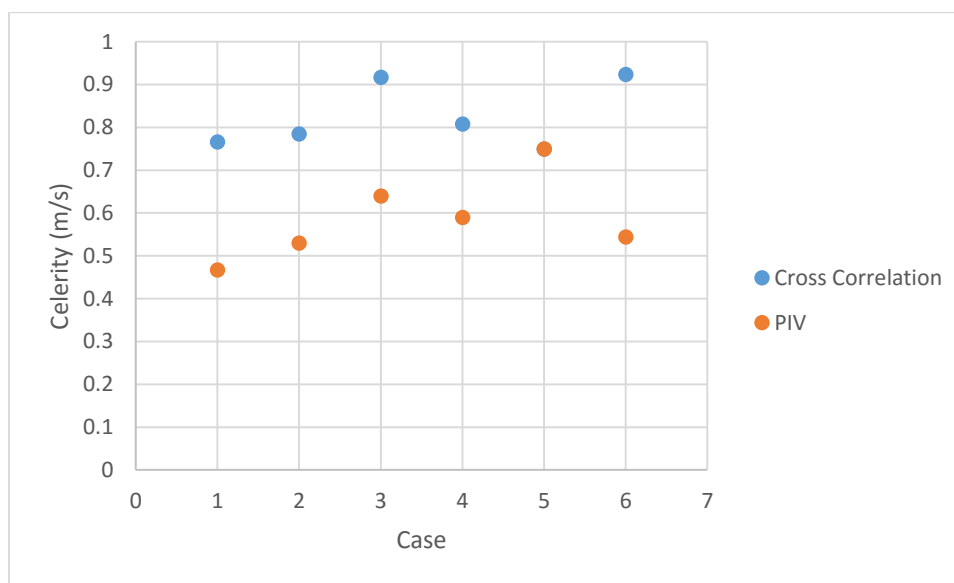
Figure 5-10: Celerity values taken by PIV and Cross correlation for polymer experiments

5.2.1 Celerity Correlations

Another way to compare our results is the empirical correlations developed from experiments, which relate between superficial velocity and celerity. However, these correlation are developed for specific flow conditions and they are valid around that range

only. We will present some of them and select the correlations which are close to our flow conditions.

One correlation was proposed by Schubring and Shedd (2008) [96]:

$$C = 0.42 \frac{V_{SG}}{\sqrt{xm}} Re_G^{-0.25} \tag{5.7}$$

where xm is the flow quality defined as:

$$xm = \frac{\dot{m}_G}{\dot{m}_G + \dot{m}_L} \tag{5.8}$$

where $\dot{m}_G$ is the gas flow rate, $\dot{m}_L$ is the mass flow rate of liquid.

However, this correlation depends only on gas superficial velocity and it is does not consider superficial velocity of liquid. A second one was developed Al-Sarkhi (2011) in which he found that wave celerity is strong function of X^* [97]:

$$\frac{C}{V_{SL}} = 2.379 X^{*-0.9} \tag{5.9}$$

$$X^* = \sqrt{\frac{\rho_G}{\rho_L}} \frac{\dot{m}_L}{\dot{m}_G} = \sqrt{\frac{\rho_G}{\rho_L}} \frac{V_{SL}}{V_{SG}} \tag{5.10}$$

where X^* is the modified Lockhart- Martinelli parameter.

This correlation is suitable for comparison because the pipe diameter is close to the one we have and it includes liquid superficial velocity which has significant impact on the celerity.

Another correlation was proposed by Al-Sarkhi (2014) is shown below [98]:

$$\frac{C}{V_{SL}} = 3.51 X^{*-0.81} \; for \; X^* < 0.305 \tag{5.11}$$

And

$$\frac{C}{V_{SL}} = 5.102 X^{*-0.495} \; for \; X^* > 0.305 \tag{5.12}$$

However, this correlation is not suitable for comparison because it was developed for large pipe diameter. Table 5-7 shows a comparison between the celerity predicted by Al-Sarkhi (2011) correlation using calculated V_{SL} from both flowmeter and PIV. For non-polymer case, the celerity values estimated by cross correlation is very close to the predicted value from flow meter and PIV. For the polymer case, Al-Sarkhi (2011) correlation predicted higher values for celerity using V_{SL} calculated by PIV but still there is a difference between them because the effects of adding polymer into the liquid is not included or in other words, the variation of liquid properties should be taken into account.

Table 5-7: Comparison between Al-Sarkhi (2011) correlation and Cross- Correlation technique.

			Without Polymer				
Case	V_{SL} Calculated	V_{SL} PIV	Celerity (Cross Correlation)	Celerity (V_{SL} flowmeter)	Error %	Celerity (V_{SL},PIV)	Error %
1	0.356	0.313	0.574	0.6673	- 13.98	0.662	-13.245
2	0.375	0.413	0.630	0.6902	-8.72	0.680	-7.445
3	0.395	0.339	0.708	0.6742	5.01	0.667	6.115
4	0.417	0.366	0.713	0.6975	2.22	0.672	6.104
5	0.427	0.445	0.742	0.6796	9.18	0.682	8.229
AVE			0.673	0.68176	-1.25	0.673	-0.048
			With Polymer				
Case	V_{SL} Calculated	V_{SL} PIV	Celerity (Cross Correlation)	Celerity (V_{SL} flowmeter)	Error %	Celerity (V_{SL},PIV)	Error %
1	0.277	0.401	0.766	0.654	17.139	0.678	12.893
2	0.283	0.427	0.785	0.655	19.908	0.682	15.096
3	0.292	0.540	0.917	0.657	39.623	0.699	31.277
4	0.301	0.467	0.808	0.659	22.682	0.689	17.418
5	0.318	0.523	0.750	0.663	13.155	0.696	7.683
6	0.328	0.372	0.924	0.665	39.033	0.673	37.273
AVE			0.825	0.659	25.257	0.686	20.273

5.3 Wavelength

Wavelength can be defined as the distance between two consecutive wave's crest or troughs. Two types of waves are investigated in this work: Short waves and Long waves. Short waves can be identified within field of view while the long waves require the extension of the field of view either physically or artificially by concatenating the consecutives frames. Physical extension of the field of view may not be feasible and costly. Moreover, as the field of view becomes larger, the frames rate that can achieved by the vision system become less which may reduce the accuracy of measurement due to loss of the fast object details.

For both short and long waves, two methods are used to estimate the wavelength: Power Spectrum and Cross Correlation. In the following sections, the two methods for both waves are explained.

5.3.1 Wavelength Estimation by Cross Correlation for Short Waves

The following procedure is used to estimate the wavelength:

1. Frame cropping to reduce the size of the image and make the analysis around the liquid-gas interface.

2. Each frame is converted to binary image using Sauvola adaptive thresholding technique.

3. All other small objects are removed.

4. The binary image is complemented to convert the mix region from black to white.

5. All other small objects are removed.

6. The boundary of the mixed region is extracted using the morphological operation:

a. Create a structuring element.

b. Erode the image with a structuring element.

c. Subtract the eroded image from the original image.

d. Contour of the image boundaries is traced using More-Neighborhood trace algorithm.

7. Then, the upper boundary of the mixed region, which is the interface between liquid phase and gas phase is extracted. If there are more than one value y axis, maximum of them is taken.

8. The cross-correlation between a fixed frame and the subsequent frames is calculated to find distance shift. The maximum distance shift value indicates that wave repeats itself, in other words, the maximum similarity is found. So, Δd_{max} is considered as an estimate of the wavelength. Since this value is in pixel , the following formula is used to convert it to meter

$$W_l \text{(Meter)} = \Delta d_{max} \text{ (Pixel) x FOV (Meter) /Frame Width (Pixel)} \qquad (5.13)$$

where W_l is the wavelength.

5.3.2 Wavelength Estimation by Power Spectrum for Short Waves

The following procedure is used to estimate the wavelength:

1. Frame cropping to reduce the size of the image and make the analysis around the liquid-gas interface.

2. Each frame is converted to binary image using Sauvola adaptive thresholding technique.

3. All other small objects are removed.
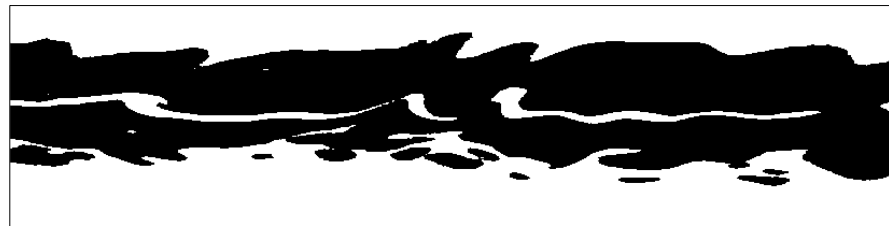
4. The binary image is complemented to convert the mix region from black to white.

5. All other small objects are removed.

6. The boundary of the mixed region is extracted using the morphological operation:

    a. Create a structuring element.

    b. Erode the image with a structuring element.

    c. Subtract the eroded image from the original image.

    d. Contour of the image boundaries is traced using More-Neighborhood trace algorithm.

7. Then, the upper boundary of the mixed region, which is the interface between liquid phase and gas phase is extracted. If there are more than one value y axis, maximum of them is taken.

8. The signal is normalized by subtracting the mean from the signal.

9. The Fast Fourier Transform (FFT) is calculated for the signal.

10. Absolute value of the transformed signal is calculated.

11. Results from step 11 is divided by number of points /2.

12. Power of the positive half is calculated.

13. The sampling frequency Fre_{samp} is calculated as follow:

$$Fre_{samp} = FW/FOV \qquad (5.14)$$

14. Determine the pin number (idx) corresponding to maximum power value.

15. The peak frequency (in distance) by the following formula is calculated as follow:

$$Fre_{peak} = \frac{idx}{FW} * Fre_{samp} \qquad (5.15)$$
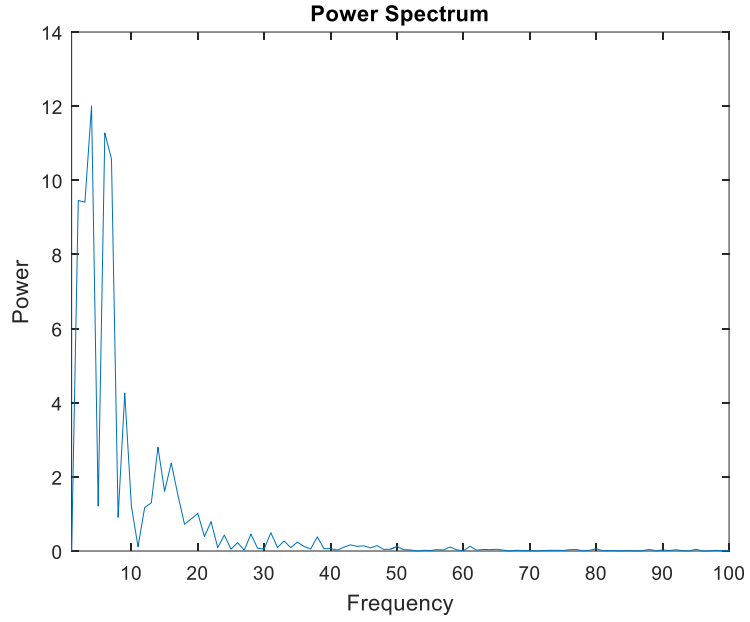
Figure 5-11 : Power spectrum for short waves

16. Calculate the wavelength by the following formula:

$$W_l = 1/Fre_{peak} \qquad (5.16)$$

Table 5-8: Wavelength (meter) Comparison between power spectrum technique and Cross-Correlation technique for non-polymer experiments.

Technique	Wavelengths (meter)				
	Case1	**Case2**	**Case3**	**Case4**	**Case5**
Power Spectrum	0.01125 0.0150 0.0225	0.01125 0.0150 0.0225	0.01125 0.0150 0.0225	0.01125 0.0150 0.0225	0.01125 0.0150 0.0225
Cross Correlation	0.015 0.023 0.022	0.01325 0.0195 0.017	0.0127 0.022 0.026	0.01184 0.0196 0.0223	0.01135 0.0156 0.033

Table 5-9: Wavelength (meter) comparison between power spectrum technique and cross-correlation technique for polymer experiments.

Technique	Wavelengths (meter)					
	Case1	Case2	Case3	Case4	Case6	Case7

71

Power Spectrum	0.01125 0.0150 0.0225	0.01125 0.0150 0.0225	0.01125 0.0150 0.0225	0.01125 0.0150 0.0225	0.01125 0.0150 0.0225	0.01125 0.0150 0.0225
Cross Correlation	0.013 0.016 0.022	0.018 0.023	0.0132 0.01748 0.0248	0.010 0.0147 0.018 0.032	0.014 0.022 0.025	0.012 0.022 0.026

As can be seen from Table 5-8 and Table 5-9, the wavelengths estimated by cross correlation and power spectrum are similar for most of cases. Cross correlation technique tends to estimate longer wavelengths than power spectrum technique. To verify the results, we measured the length of the waves directly from the video by extracting the waves from the frame and measure the length along which the wave extends. We found a good agreement between the measured directly from images and estimated values using signal processing techniques as shown below in Figure 5-12.
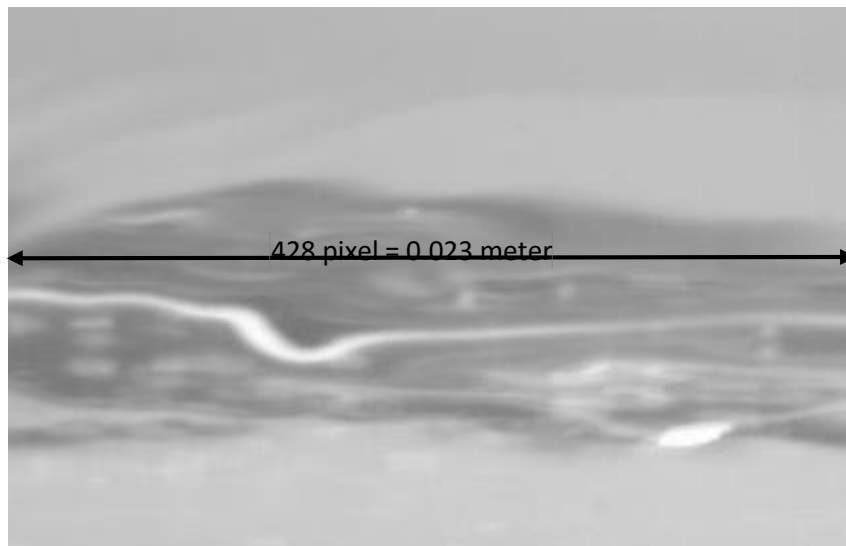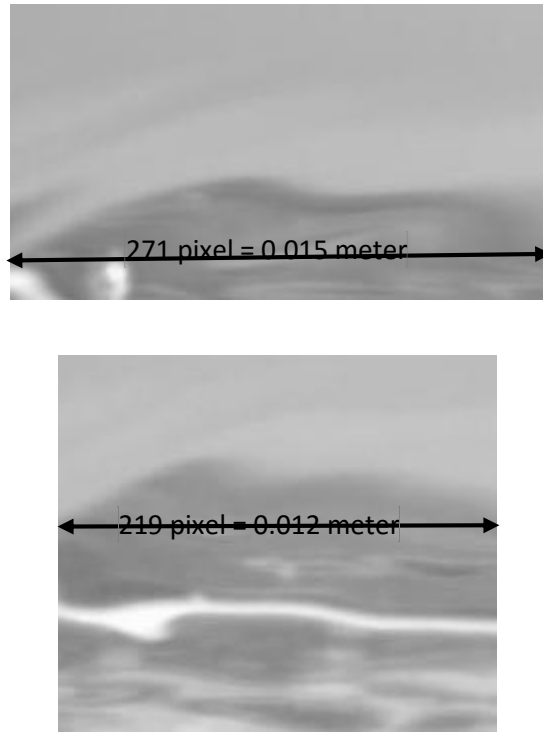
Figure 5-12: Actual wave size.

5.3.3 Wavelength Estimation by Cross Correlation for Long Waves

The following procedure is used to estimate the wavelength:

1. Frame cropping to reduce the size of the image and make the analysis around the liquid-gas interface.

2. Each frame is converted to binary image using Sauvola adaptive thresholding technique.

3. All other small objects are removed.

4. The binary image is complemented to convert the mix region from black to white.

5. All other small objects are removed.

6. The boundary of the mixed region is extracted using the morphological operation:

   a. Create a structuring element.

   b. Erode the image with a structuring element.

    c. Subtract the eroded image from the original image.

    d. Contour of the image boundaries is traced using More-Neighborhood trace algorithm.

7. Then, the upper boundary of the mixed region, which is the interface between liquid phase and gas phase is extracted. If there are more than one value y axis, maximum of them is taken.

8. Calculate the cross correlation between a fixed frame and the subsequent frames to find the distance shift within the window.

9. Convert the distance shift value from pixel to meter.

10. Calculate the shift in time (ΔT) by dividing the distance shift by wave velocity (celerity).

11. Determine the period that wave needed to reach to frame n (nT) where is T is 1/ Frame rate.

12. Calculate the total period by the following formula:

$$\boldsymbol{T_{total}} = \Delta \boldsymbol{T} + \boldsymbol{nT} \tag{5.17}$$

13. Long wavelength can be calculated using the following formula:

$$\boldsymbol{W_l} = \boldsymbol{T_{total}} \times \boldsymbol{C} \tag{5.18}$$

Table 5-10 shows the ten main wavelengths for non-polymer case while Table 5-11 shows ten main wavelengths for polymer case. It can be seen that the wavelengths in polymer case is slightly higher than non-polymer case due to the effect of polymer in reducing the turbulence in the flow and allows the waves to extend more without breaking.

Table 5-10: Main long wavelengths estimated by cross correlation technique for non-polymer case.

Wavelength (meter)	Case 1	Case 2	Case 3	Case 4	Case 5
W_l 1	0.26	0.3	0.32	0.33	0.32
W_l 2	0.24	0.29	0.31	0.32	0.31
W_l 3	0.22	0.28	0.30	0.31	0.30
W_l 4	0.21	0.27	0.28	0.30	0.29
W_l 5	0.20	0.26	0.27	0.29	0.28
W_l 6	0.13	0.25	0.26	0.28	0.27
W_l 7	0.12	0.24	0.25	0.27	0.26
W_l 8	0.11	0.23	0.24	0.26	0.25
W_l 9	0.10	0.22	0.23	0.25	0.24
W_l 10	0.09	0.21	0.22	0.24	0.23

Table 5-11: Main long wavelengths estimated by cross correlation technique for polymer case.

Wavelength (meter)	Case 1	Case 2	Case 3	Case 4	Case 6	Case 7
W_l 1	0.34	0.36	0.42	0.36	0.32	0.41
W_l 2	0.32	0.34	0.41	0.35	0.31	0.40
W_l 3	0.31	0.33	0.40	0.34	0.30	0.39
W_l 4	0.30	0.32	0.38	0.33	0.29	0.38
W_l 5	0.29	0.31	0.37	0.32	0.28	0.36
W_l 6	0.28	0.30	0.35	0.31	0.27	0.35
W_l 7	0.27	0.29	0.34	0.30	0.23	0.34
W_l 8	0.26	0.28	0.33	0.29	0.22	0.33
W_l 9	0.25	0.27	0.32	0.28	0.18	0.32
W_l 10	0.24	0.26	0.31	0.27	0.17	0.31

5.3.4 Wavelength Estimation by Power Spectrum for Long Waves

The following procedure is used to estimate the wavelength:

1. Frame size is extended by concatenating subsequent frames. This can be done by adding the part of the frame that shifts a distance (Δd) to the previous frame. This distance shift can be estimated from cross correlation done in the previous steps. So, the extended frame (concatenated window) can be made using the following formula:

$$Win_{fr} \text{ (Pixel)} = Win_{fr-1}(\text{Pixel}) + Win_{\Delta d} \text{ (Pixel)} \qquad (5.19)$$

where Win_{fr} is the concatenated window, fr is the frame index.

Figure 5-13: Concatenated Image

2. Frame cropping to reduce the size of the image and make the analysis around the liquid-gas interface.

3. Each frame is converted to binary image using Sauvola adaptive thresholding technique with the following settings.

4. All other small objects are removed.

5. The binary image is complemented to convert the mix region from black to white.

6. All other small objects are removed.

7. The boundary of the mixed region is extracted using the morphological operation:

   a. Create a structuring element.

   b. Erode the image with a structuring element.

   c. Subtract the eroded image from the original image.

    d. Contour of the image boundaries is traced using More-Neighborhood trace

    algorithm.

8. Then, the upper boundary of the mixed region, which is the interface between

    liquid phase and gas phase is extracted. If there are more than one value y axis,

    maximum of them is taken.

9. The signal is normalized by subtracting the mean from the signal.

10. The extended frame width and extended field of view is calculated for the

    concatenated frame to be used in the power spectrum analysis.

11. The Fast Fourier Transform (FFT) is calculated for the signal.

12. Take absolute value of the transformed signal.

13. Result from step 11 is divided by number of points /2.

14. The power of the positive half is calculated.

15. The pin number idx corresponding to maximum power value is determined.

16. The extended frame width (FW_{ext}) and extended Field of View (FOV_{ext}) are

    calculated.

17. The sampling frequency F_{samp} is calculated as follow:

$$Fre_{samp} = FW_{ext}/FOV_{ext} \qquad\qquad (5.20)$$

18. he peak frequency (in distance) is calculated by the following formula:

$$Fre_{peak} = \frac{idx}{FW_{ext}} * Fre_{samp} \qquad\qquad (5.21)$$
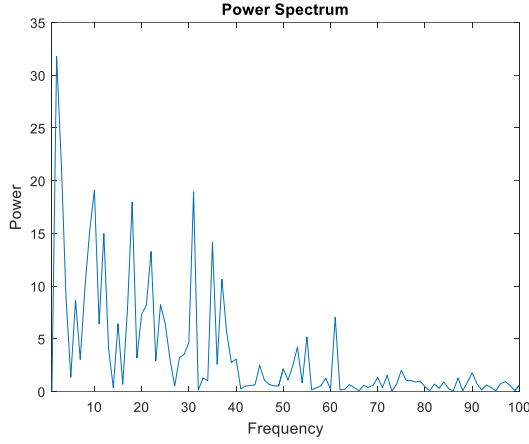
Figure 5-14: Power Spectrum for long waves.

19. Wavelength is calculated by the following formula:

$$W_l = 1/Fre_{peak} \tag{5.22}$$

Table 5-12 shows the long wavelengths estimated by power spectrum technique for non-polymer case while Table 5-13 shows the long wavelengths for polymer case. Similar to cross-correlation technique, the wavelengths in polymer case are slightly higher than non-polymer case. The cross correlation tends to estimate longer wavelengths than power spectrum. Looking to the lower values of the power spectrum, we can see also the short waves estimated previously within original field of view.

Table 5-12: Long wavelengths estimated by power spectrum technique for non-polymer case.

Pin	Case1 PW	W_l (m)	Case 2 PW	W_l (m)	Case 3 PW	W_l (m)	Case 4 PW	W_l (m)	Case 5 PW	W_l (m)
1	4.6E-28		2.3E-29		2.7E-28		8.1E-29		9.2E-29	
2	27.370	0.165	119.298	0.176	141.156	0.187	31.796	0.187	50.176	0.197
3	53.978	0.110	89.337	0.117	35.980	0.124	21.557	0.124	171.557	0.132
4	9.578	0.082	74.386	0.088	38.595	0.093	8.751	0.093	137.033	0.099
5	8.544	0.066	29.567	0.070	122.770	0.075	1.361	0.075	23.030	0.079
6	1.129	0.055	56.995	0.059	12.006	0.062	8.664	0.062	63.395	0.066
7	1.925	0.047	14.574	0.050	119.150	0.053	3.039	0.053	9.329	0.056
8	1.083	0.041	20.061	0.044	67.544	0.047	9.880	0.047	12.480	0.049

9	2.041	0.037	11.546	0.039	0.054	0.041	15.244	0.041	7.883	0.044
10	0.577	0.033	3.174	0.035	24.876	0.037	19.094	0.037	14.345	0.039
11	0.916	0.030	16.769	0.032	0.643	0.034	6.429	0.034	27.113	0.036
12	0.292	0.027	4.110	0.029	39.240	0.031	14.979	0.031	10.266	0.033
13	0.635	0.025	7.988	0.027	27.661	0.029	4.088	0.029	36.595	0.030
14	0.383	0.024	1.925	0.025	14.770	0.027	0.360	0.027	19.244	0.028
15	0.732	0.022	10.570	0.023	1.545	0.025	6.408	0.025	44.528	0.026
16	0.204	0.021	2.489	0.022	16.864	0.023	0.680	0.023	24.894	0.025
17	0.331	0.019	5.132	0.021	31.704	0.022	7.785	0.022	2.790	0.023
18	0.102	0.018	0.726	0.020	25.020	0.021	17.970	0.021	17.113	0.022
19	0.244	0.017	3.351	0.018	2.415	0.020	3.185	0.020	8.844	0.021
20	0.191	0.016	1.467	0.018	16.867	0.019	7.322	0.019	9.528	0.020
21	0.307	0.016	1.931	0.017	10.153	0.018	8.197	0.018	15.953	0.019
22	0.088	0.015	6.297	0.016	19.199	0.017	13.270	0.017	7.649	0.018
23	0.154	0.014	3.633	0.015	2.879	0.016	2.906	0.016	0.435	0.017
24	0.063	0.014	2.374	0.015	12.594	0.016	8.229	0.016	21.315	0.016
25	0.113	0.013	4.232	0.014	4.284	0.015	6.425	0.015	2.538	0.016
26	0.106	0.013	0.902	0.014	4.576	0.014	3.085	0.014	6.904	0.015
27	0.166	0.012	3.846	0.013	14.637	0.014	0.520	0.014	5.769	0.015
28	0.069	0.012	1.837	0.013	1.231	0.013	3.186	0.013	0.033	0.014
29	0.073	0.011	1.542	0.012	5.678	0.013	3.506	0.013	1.050	0.014
30	0.091	0.011	4.132	0.012	4.593	0.012	4.643	0.012	8.462	0.013
31	0.093	0.011	2.622	0.011	11.242	0.012	18.935	0.012	5.777	0.013
32	0.093	0.010	5.293	0.011	2.770	0.012	0.124	0.012	2.938	0.012
33	0.066	0.010	0.515	0.011	0.141	0.011	1.298	0.011	2.706	0.012
34	0.045	0.010	1.553	0.010	1.974	0.011	1.022	0.011	6.984	0.012
35	0.094	0.009	4.582	0.010	8.546	0.011	14.142	0.011	3.296	0.011
36	0.090	0.009	0.031	0.010	14.317	0.010	2.581	0.010	10.195	0.011
37	0.075	0.009	1.143	0.009	13.569	0.010	10.642	0.010	2.195	0.011
38	0.077	0.009	2.384	0.009	0.057	0.010	5.649	0.010	1.984	0.010
39	0.040	0.008	0.327	0.009	3.146	0.010	2.732	0.010	7.346	0.010
40	0.031	0.008	3.220	0.009	2.028	0.009	3.081	0.009	1.407	0.010

Table 5-13: Long wavelengths estimated by power spectrum technique for non-polymer case.

Pin	Case1		Case 2		Case 3		Case 4	
	PW	W_l (m)	PW	W_l (m)	PW	W_l (m)	PW	W_l (m)
1	2.31E-28		6.95558E-28		5.07555E-28		7.24841E-28	0.416784409
2	22.046	0.208	541.710	0.208	44.587	0.230	163.233	0.208
3	3.605	0.139	114.708	0.139	41.123	0.154	51.684	0.139
4	0.054	0.104	29.574	0.104	0.237	0.115	0.951	0.104
5	2.265	0.083	101.179	0.083	6.677	0.092	36.590	0.083

6	1.753	0.069	46.581	0.069	7.685	0.077	7.936	0.069
7	19.524	0.060	50.773	0.060	37.740	0.066	16.035	0.060
8	4.658	0.052	8.584	0.052	53.973	0.058	0.856	0.052
9	4.472	0.046	8.883	0.046	56.077	0.051	21.057	0.046
10	42.092	0.042	7.394	0.042	6.194	0.046	58.094	0.042
11	7.254	0.038	15.464	0.038	15.863	0.042	24.155	0.038
12	0.588	0.035	2.230	0.035	41.823	0.038	19.924	0.035
13	10.896	0.032	7.081	0.032	7.448	0.035	2.079	0.032
14	9.611	0.030	20.164	0.030	15.725	0.033	2.312	0.030
15	41.463	0.028	6.854	0.028	9.865	0.031	9.043	0.028
16	3.541	0.026	1.276	0.026	24.052	0.029	2.401	0.026
17	2.454	0.025	6.158	0.025	1.263	0.027	11.182	0.025
18	4.320	0.023	5.024	0.023	0.762	0.026	20.744	0.023
19	3.520	0.022	2.105	0.022	21.192	0.024	1.036	0.022
20	0.048	0.021	2.400	0.021	4.198	0.023	2.548	0.021
21	0.554	0.020	3.918	0.020	3.517	0.022	17.015	0.020
22	2.408	0.019	0.909	0.019	2.494	0.021	12.999	0.019
23	1.990	0.018	11.480	0.018	3.743	0.020	11.126	0.018
24	1.072	0.017	2.291	0.017	0.293	0.019	6.687	0.017
25	3.851	0.017	1.872	0.017	3.007	0.018	7.589	0.017
26	1.072	0.016	2.143	0.016	5.317	0.018	0.466	0.016
27	2.681	0.015	0.955	0.015	1.592	0.017	3.731	0.015
28	0.280	0.015	3.493	0.015	5.187	0.016	3.288	0.015
29	2.899	0.014	0.468	0.014	2.426	0.016	1.236	0.014
30	2.271	0.014	0.006	0.014	0.657	0.015	5.199	0.014
31	7.879	0.013	0.481	0.013	0.042	0.015	0.898	0.013
32	0.684	0.013	2.535	0.013	11.826	0.014	0.651	0.013
33	0.427	0.013	8.169	0.013	1.726	0.014	0.049	0.013
34	1.372	0.012	0.326	0.012	5.169	0.014	4.172	0.012
35	1.196	0.012	5.094	0.012	6.625	0.013	0.002	0.012
36	0.115	0.012	3.180	0.012	1.473	0.013	0.510	0.012
37	1.797	0.011	1.276	0.011	5.112	0.012	0.088	0.011
38	0.837	0.011	1.214	0.011	0.828	0.012	0.513	0.011
39	3.034	0.011	0.069	0.011	4.610	0.012	1.707	0.011
40	1.035	0.010	1.593	0.010	6.626	0.012	2.096	0.010
41	1.041	0.010	4.997	0.010	0.749	0.011	0.694	0.010
42	1.673	0.010	1.115	0.010	8.311	0.011	0.035	0.010
43	1.387	0.010	1.869	0.010	5.642	0.011	3.133	0.010
44	1.135	0.009	0.507	0.009	2.070	0.010	1.263	0.009
45	0.426	0.009	2.185	0.009	1.256	0.010	8.079	0.009
46	1.826	0.009	5.069	0.009	1.148	0.010	1.951	0.009

47	0.277	0.009	1.775	0.009	7.424	0.010	0.293	0.009
48	3.125	0.009	0.831	0.009	5.540	0.010	3.181	0.009
49	1.145	0.009	3.215	0.009	2.310	0.009	0.035	0.009
50	0.727	0.008	4.145	0.008	2.777	0.009	0.696	0.008
51	0.564	0.008	1.938	0.008	3.819	0.009	1.216	0.008
52	0.113	0.008	0.829	0.008	0.678	0.009	2.107	0.008
53	0.189	0.008	1.802	0.008	4.494	0.009	1.284	0.008
54	0.590	0.008	0.154	0.008	4.334	0.009	0.636	0.008
55	0.032	0.008	1.074	0.008	1.356	0.008	0.391	0.008
56	0.144	0.007	1.300	0.007	0.236	0.008	2.878	0.007
57	0.559	0.007	3.392	0.007	5.241	0.008	2.874	0.007
58	0.035	0.007	1.558	0.007	0.482	0.008	1.584	0.007
59	1.557	0.007	1.119	0.007	0.133	0.008	1.945	0.007
60	0.855	0.007	0.792	0.007	1.579	0.008	0.379	0.007

Case 5		Case 6	
PW	W_l (m)	PW	W_l (m)
3.03E-28	0.395791717	6.61472E-28	0.483489647
270.650	0.198	239.390	0.242
149.635	0.132	179.517	0.161
19.730	0.099	32.973	0.121
21.346	0.079	30.400	0.097
54.580	0.066	39.267	0.081
50.149	0.057	26.899	0.069
41.251	0.049	12.510	0.060
28.602	0.044	3.624	0.054
14.463	0.040	11.807	0.048
3.861	0.036	10.320	0.044
9.170	0.033	5.936	0.040
5.778	0.030	6.236	0.037
7.742	0.028	5.940	0.035
1.177	0.026	10.912	0.032
1.313	0.025	4.916	0.030
2.484	0.023	0.073	0.028
20.441	0.022	4.799	0.027
3.747	0.021	0.746	0.025
8.346	0.020	6.582	0.024
0.610	0.019	5.283	0.023
4.606	0.018	7.526	0.022
7.323	0.017	0.875	0.021

1.361	0.016	12.917	0.020
8.786	0.016	2.480	0.019
1.820	0.015	0.254	0.019
4.222	0.015	5.651	0.018
1.352	0.014	2.367	0.017
3.149	0.014	3.291	0.017
3.173	0.013	1.681	0.016
5.163	0.013	4.642	0.016
1.505	0.012	0.526	0.015
0.992	0.012	0.096	0.015
1.039	0.012	1.283	0.014
0.752	0.011	4.982	0.014
3.879	0.011	0.445	0.013
0.916	0.011	1.289	0.013
1.441	0.010	1.243	0.013
0.048	0.010	0.298	0.012
1.856	0.010	1.778	0.012
0.144	0.010	2.629	0.012
0.182	0.009	0.082	0.012
0.799	0.009	0.418	0.011
0.100	0.009	0.845	0.011
0.017	0.009	1.791	0.011
0.427	0.009	0.189	0.011
0.242	0.008	2.854	0.010
0.009	0.008	0.318	0.010
0.324	0.008	0.173	0.010
0.792	0.008	0.132	0.010
0.662	0.008	2.082	0.009
1.424	0.008	0.126	0.009
1.050	0.007	1.284	0.009
2.058	0.007	0.829	0.009
0.733	0.007	0.730	0.009
1.543	0.007	0.590	0.009
0.152	0.007	0.449	0.008
1.152	0.007	0.022	0.008
0.102	0.007	0.374	0.008
0.033	0.007	0.206	0.008

5.4 Wave Frequency and Period

Wave frequency W_{Fre} and period W_T can be calculated using the following formulas:

$$W_{Fre} = C/W_l \tag{5.23}$$

$$W_T = 1/W_{Fre} \tag{5.24}$$

Frequencies and period are calculated for both short and long waves. Table 5-14 shows the high frequencies and short periods for non-polymer case while Table 5-15 shows the high frequencies and short periods for polymer case. The frequencies in polymer case is slightly higher than non-polymer case although the wavelengths is higher but difference in celerity values is much higher than the difference in wavelengths. Table 5-16 shows low frequencies and long periods for long waves in non-polymer case and Table 5-17 shows them for polymer case. Similar to the short waves, long waves in polymer case have slightly higher frequencies and shorter period than non-polymer case.

Table 5-14: Frequencies and period for short waves (non-polymer case)

Case No	Frequency (Hz)	Period (s)
1	25.51 , 38.27, 51.02	0.04, 0.026, 0.02
2	28 , 42, 56 ,	0.036, 0.024, 0.018
3	31.5, 47.2, 63, 78.7	0.032, 0.021,0.016, 0.013
4	31.7, 47.53, 63.38, 79.22	0.032, 0.021, 0.016, 0.0092
5	33.0 , 49.5, 66.0, 82.44, 99.0	0.03, 0.02,0.015,0.012,0.010

Table 5-15: Frequencies and period for short waves (polymer case)

Case No	Frequency (Hz)	Period (s)
1	34.04, 51.07, 68.09, 85.11,102.13	0.029,0.02, 0.015, 0.012,0.0098
2	34.89, 52.33, 69.78,	0.029, 0.019, 0.014
3	40.76, 61.13, 81.51, 122.67, 142.64	0.025, 0.016, 0.012, 0.0082, 0.007

4	35.91, 53.87, 71.82, 89.78,125.69	0.028, 0.019, 0.014, 0.011, 0.008
6	33.33, 50, 66.67,83.33,116.67,133.33	0.03, 0.02,0.015, 0.012,0.0090,0.008
7	41.07, 61.6, 82.13,102.67 123.2,143.73	0.024,0.016, 0.012, 0.01, 0.008, 0.007

Table 5-16: Frequencies and periods for long waves (non-polymer case)

Case No	Frequency (Hz)	Period (s)
1	3.49 , 5.23 , 6.97, 8.72	0.28, 0.19 ,0.14 ,0.11
2	3.59, 5.38 ,7.18, 10.76	0.28, 0.19,0.14,0.093
3	3.8, 9.5 , 13.3 ,15.18	0.26 0.11, 0.08 ,0.07
4	3.82,5.73, 19.11	0.26 ,0.17, 0.052
5	3.76 , 5.63 , 7.52, 11.27	0.27, 0.17, 0.13, 0.09

Table 5-17: Frequencies and periods for long waves (polymer case)

Case No	Frequency (Hz)	Period (s)
1	3.68 , 5.51, 9.189, 12.9	0.27, 0.18, 0.11, 0.08
2	3.77, 5.65, 9.42, 13.18	0.27, 0.18, 0.11,0.08
3	3.76, 12.9 ,18.37, 27.57	0.27, 0.08, 0.054, 0.036
4	3.88, 5.82, 9.69 , 19.39	0.26 ,0.17, 0.10, 0.052
6	3.79, 5.68, 11.37, 13.26	0.26 , 0.18, 0.09 , 0.075
7	3.82 , 5.73, 7.644, 11.5,	0.26 , 0.17, 0.13 , 0.09

5.4.1 Frequency Correlations

These correlations are used to validate the estimated frequencies for long waves. The first correlation was proposed by Schubring and Shedd (2008) as shown in equation (5.25)

$$Fre = 0.0050 \frac{V_{SG}}{D\sqrt{xm}} \qquad (5.25)$$

However, this correlation is not suitable because it was developed for small diameter (8.8, 15.1 mm). Another correlation proposed also by Schubring and Shedd but it was developed for 26.3 mm shown in:

$$Fre = 0.035 \frac{V_{SG}\sqrt{Fr_{mod}}}{D} \tag{5.26}$$

$$Fr_{mod} = \frac{\rho_G V_{SG}}{\rho_L \sqrt{gaD}} \tag{5.27}$$

Although this correlation was developed for a pipe diameter close to the one we have but it does not consider the effect of liquid superficial velocity.

Ousaka et al. (1992) [99] proposed a correlation in which he includes the effect of liquid superfical velocity which directly propotinal to the wave frequncy as shown in :

$$Fre = 0.066 \frac{V_{SL}}{D} \left(\frac{Re_G}{Re_L}\right)^{1.18} \tag{5.28}$$

Another correlation proposed by Setyawan et al (2014) [100] which was developed following the model of Schubring and Shedd (2008) to improve the accuracy wave frequency prediction as shown below:

$$Fre = 0.0035 \frac{V_{SL}^{0.02} V_{SG}^{0.9} Fr_{mod}^{0.25}}{D^{0.8} xm^{0.25}} \tag{5.29}$$

Table 5-18 and Table 5-19 shows the comparison between the estimated max frequency and the predicted frequency by Ousaka (1992) and Andriyanto et al (2014) correlations. The estimated frequency value lies between two values but it is more close to Andriyanto et al (2014) correlation. Another observation is that estimated frequency value and Andriyanto et al (2014) correlations in general have similar trend while Ousaka (1992) shows opposite trend as shown in Figure 5-15 and Figure 5-16.

Table 5-18: Max Wave Frequency comparison with correlations for experiment without polymer.

Case no	Estimated max Frequency	Ousaka (1992)	Error %	Andriyanto et al (2014)	Error %
1	3.49	2.55	37.11	4.33	19.35
2	3.59	2.52	42.45	4.39	18.24
3	3.8	2.50	52.21	4.45	14.64
4	3.82	2.47	54.55	4.52	15.45
5	3.76	2.46	52.78	4.55	17.30

Table 5-19: Max Wave Frequency comparison with correlations for experiment with polymer.

Case no	Estimated max Frequency	Ousaka (1992)	Error %	Andriyanto et al (2014)	Error %
1	3.68	2.56	43.64	4.29	14.15
2	3.77	2.55	47.73	4.31	12.55
3	3.76	2.54	48.10	4.34	13.44
4	3.88	2.52	53.77	4.38	11.48
5	3.79	2.50	51.63	4.44	14.72
6	3.82	2.49	53.70	4.48	14.76
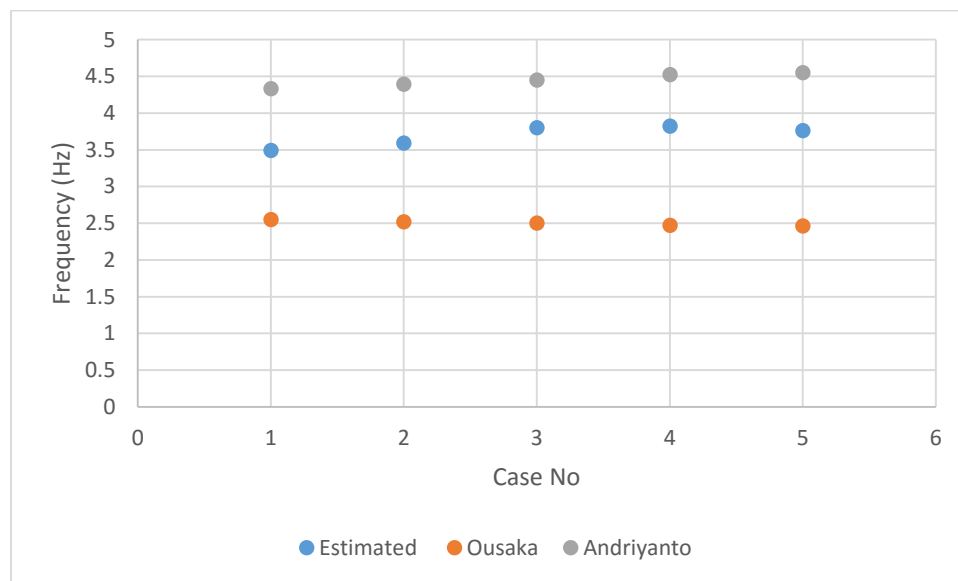
Figure 5-15 : Frequency Comparison for experiments with no-polymer
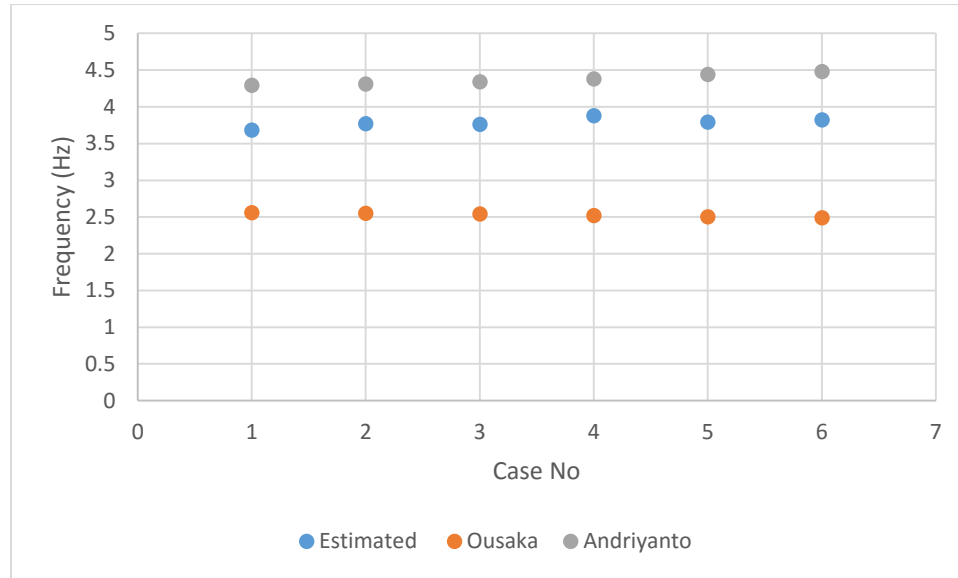
Figure 5-16 : Frequency Comparison for experiments with polymer

5.5 Wave Amplitude

Wave amplitude can be defined as one half of the distance between wave's crest and troughs.

The following procedure is used:

1. Frame cropping to reduce the size of the image and make the analysis around the liquid-gas interface.

2. Each frame is converted to binary image using Sauvola adaptive thresholding technique.

3. The binary image is complemented to convert the mix region from black to white.

4. All small holes are filled.

5. All other small objects are removed.

6. The boundary of the mixed region is extracted using the morphological operation:

a. Create a structuring element.

b. Erode the image with a structuring element.

c. Subtract the eroded image from the original image.

d. Contour of the image boundaries is traced using More-Neighborhood trace algorithm.

7. Then, the upper boundary of the mixed region, which is the interface between liquid phase and gas phase is extracted. If there are more than one value y axis, maximum of them is taken.

8. The maximum and minimum of the extracted signal are calculated.

9. Wave amplitude can be calculated by subtracting the minimum value from the maximum value and divide the results by 2.

10. The wave amplitude W_{Amp} calculated from step 9 is in pixel. The following formula is used to convert to meter:

$$W_{Amp} \text{ (Meter)} = W_{Amp} \text{ (Pixel) x FOV (Meter) /FW (Pixel)} \tag{5.30}$$

Table 5-20 shows the wave amplitude for non-polymer case while Table 5-21 shows the wave amplitude for polymer case. From these two tables, we can see the effect of adding polymer to reduce the turbulence in the flow. The average of the wave amplitude in polymer case is reduced by about 27 % and variation is reduced by 30 % compared to the non-polymer case. In other words, the polymer makes flow smoother and depresses the high wave formation which may lead to slug flow which undesirable flow pattern in pipelines.

Table 5-20: Wave Amplitude for non-polymer case (meter).

	Case 1	Case 2	Case 3	Case 4	Case 5	ALL
Ave	0.0013	0.0012	0.0014	0.0018	0.0018	0.0015

Min	0.0005	0.0004	0.0006	0.0008	0.0007	0.0006
Max	0.0028	0.0028	0.0036	0.0043	0.0044	0.0036
STD	0.0006	0.0006	0.0006	0.0006	0.0008	0.0006

Table 5-21: Wave Amplitude for polymer case (meter).

	Case 1	Case 2	Case 3	Case 4	Case 5	Case 7	ALL
Ave	0.0013	0.0012	0.0009	0.0013	0.0011	0.0009	0.0011
Min	0.0005	0.0005	0.0004	0.0004	0.0003	0.0004	0.0004
Max	0.0032	0.0032	0.0028	0.0040	0.0031	0.0027	0.0031
STD	0.0004	0.0004	0.0003	0.0006	0.0004	0.0004	0.0004

5.6 Hold Up

In this work, the holdup is calculated based on the area occupied by each phase. The following procedure is used to calculate the hold up:

1. Frame cropping to reduce the size of the image to capture internal pipe area only.

2. Each frame is converted to binary image using Sauvola adaptive thresholding technique with the following settings.

3. All other small objects are removed.

4. The area of the mix region (White area) is calculated.

5. The binary is complemented to convert the mix region from black to white.

6. The area occupied by the liquid is calculated.

7. The area occupied by the gas is calculated.

8. Since the mix region is a liquid dominant, it is added to liquid area.

9. Liquid hold up is calculated by the following formula:

$$H_L = \frac{A_L}{A_p}$$
(5.31)

where A_L = Area of liquid + Area of mix region , A_p: internal pipe area

10. Gas hold up is calculated by the following formula:

$$H_G = \frac{A_G}{A_p}$$
(5.32)

or

$$H_G = 1 - H_L$$
(5.33)

Figure 5-17 show the area occupied by the gas, liquid and mix region between them for one frame sample.
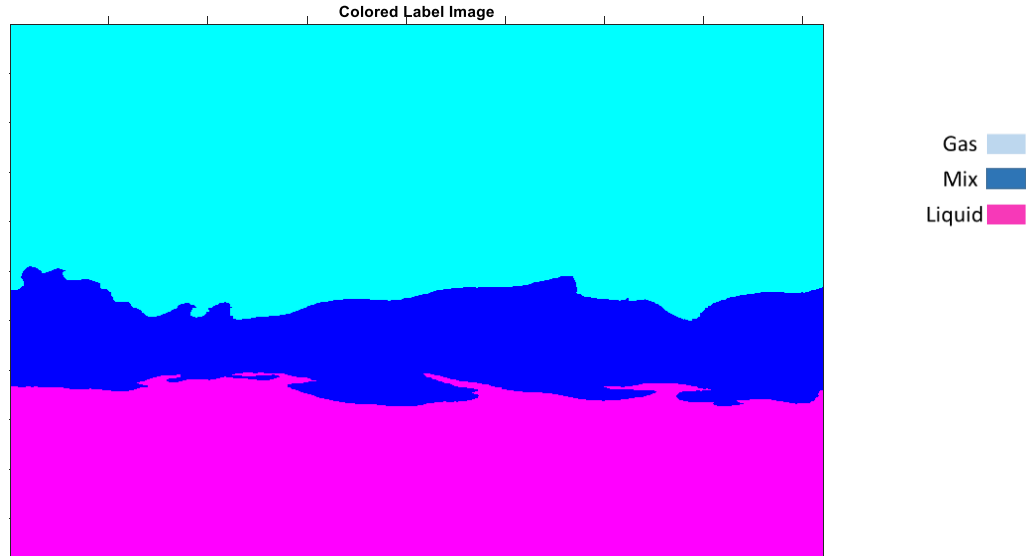
Figure 5-17: Image segmentation into liquid, mixed region and gas.

Liquid hold up value for non-polymer case is shown in Table 5-22 while the holdup value for polymer case is shown Table 5-23. Although the average hold up for both non-polymer and polymer case is close to each other, the holdup variation in non-polymer case

90

is much higher than polymer case which indicate that flow is more turbulent in non-polymer case which can be seen clearly from the standard deviation of both cases.

Table 5-22: Liquid Hold up for non-polymer case.

	Case 1	Case 2	Case 3	Case 4	Case 5	ALL
Ave	0.414	0.421	0.422	0.444	0.435	0.427
Min	0.352	0.370	0.383	0.399	0.383	0.377
Max	0.562	0.525	0.499	0.487	0.491	0.513
STD	0.060	0.027	0.028	0.014	0.028	0.031

Table 5-23: Liquid Hold up for polymer case.

	Case 1	Case 2	Case 3	Case 4	Case 5	Case 6	ALL
Ave	0.401	0.390	0.433	0.416	0.486	0.484	0.435
Min	0.368	0.347	0.373	0.390	0.418	0.438	0.388
Max	0.430	0.414	0.490	0.460	0.566	0.564	0.486
STD	0.012	0.012	0.018	0.017	0.026	0.023	0.018

Summary and Conclusion

Two sets of experiments were conducted in this research to investigate the behavior of Stratified Wavy flow which is an important flow pattern in industry. First set of the experiments were performed to estimate the main multiphase flow parameters for two phase (air and water) while the second set of experiment were conducted to estimate the parameters with addition of drag reducing polymer. First estimated parameter is the wave velocity (Celerity). The results were compared with PIV results and it showed good match

for the first set of experiments but image processing technique showed better results for the second set of experiment. Also, the results were compared with empirical correlations and it showed good match as well. The second estimated parameter is wavelength. Both short and long wavelength in two sets of experiments were estimated using two techniques: cross correlation and power spectrum. The results of the two methods are close and validated by the visual measurement for the short wave but for the long wave cross correlation estimated higher values. The third and fourth estimated parameters are the wave frequency and the wave period. Both high frequencies (short period) and low frequencies (long period) were estimated for both sets of experiments. Frequency correlations were used for comparison. Wave amplitude is fifth parameter estimated in this research for both sets of the experiments. Hold up is the sixth parameter estimated for both set of experiment and the results agreed with visual observation. From the results, the effect of adding the polymer to the flow is so clear in making the flow smoother and stable which are desirable features for multiphase flow in pipelines.

CHAPTER 6

FLOW PATTERNS IDENTIFICATION USING ARTIFICIAL NEURAL NETWORK

Introduction

Multiphase flow refers to the simultaneous flow of two phases or more and they can be liquid, gas, solid, two components from the same phase such oil and water, or two phases single component such as water vapor and liquid. Multiphase flow is encountered in many industries and processes such as oil and gas industry and petrochemical process, and there is an increasing demand for more accurate multiphase metering. Several approaches were reported in the literature in the modeling side to accurately identify the flow features and parameters [18]. One of the common difficulties in these techniques is the need to identify the flow pattern correctly. Flow patterns are more than 20 types including bubble flow, Slug flow, Annular flow and many more. These flow patterns depend on many factors such as pipe inclination, phase composition and physical properties, and velocity of the individual fluids [5].

The overlapping between these flow patterns especially at the transition zones makes the identification more difficult. Therefore, the combination of flow patterns at transition zone introduces metering errors, as these meters usually assume one type of flow patterns and are tuned based on it. Accordingly, identification of the correct flow pattern at different time interval will greatly improve the multiphase flow measurement [4].

Artificial Intelligence (AI) is a promising technique to identify flow patterns. Xiea et al. [101] used transportable artificial neural network for the classification of flow patterns. They studied three phase flow (Gas/Liquid/Fiber) in vertical pipe. They used 7 inputs in terms of normalized pressure signals (standard deviation, coefficients of skewness and kurtosis, and several second-order correlation terms). They reported classification problems in the transition zone. Rosa et al [102] attempted to develop an expert system to identify the flow pattern. They studied 6 flow patterns. They used several types of Artificial Neural Networks (ANN) and expert systems for flow patterns identification. They used four statistical momentums (mean, standard deviation, skewness and kurtosis) and Probability Density Function (PDF) of instantaneous line average void fraction as inputs to the system. They used clustering systems and showed that clustering algorithms has low correct identification rate because of confusion at transition zones when number of flow patterns is large. They concluded that knowledge base is required to assist neural network

El-Sebakhy [103] used adaptive Neuro Fuzzy Interference System (ANFIS) for flow patterns classifications. He selected ANFIS because of its ability to predict the output in uncertain conditions. ANN Inputs are liquid superficial velocity, gas superficial velocity, pressure, temperature, fluid properties. Four flow patterns were studied: Annular, Slug, Wavy and Stratified. The results showed high correct classification rate, but suffered from misclassifications at transition zones. Murat and Ertan [31] implemented three AI techniques: Nearest Neighborhood (NN), Back propagation Neural Network (BNN) and classification tree (CT) to identify the flow pattern and estimate liquid hold up. He used Reynolds number for both gas and liquid as neural network inputs. Seven flow patterns were considered in his study. To improve the performance, he scaled the gas Reynolds

number to overcome the issue of overlapping between flow patterns. It was concluded that BNN has the best performance in flow patterns identification.

The main objective in this work is to use an ANN with non-dimensional inputs to be used for different flow conditions such as, pipe diameter, liquid density and viscosity. Three non-dimensional inputs were used: Liquid Reynold Number, Gas Reynold Number and Pressure Drop Multiplier. Also, a pre-process stage for data was performed before feeding them to neural network using logarithmic normalization to properly scale the data and reduce the overlapping between flow regimes.

The chapter is organized as follows: Section.2 explains the concept of Artificial Neural Network, Section.3 describes the flow patterns, Section.4 explains the Unified Model used to generate the data, Section. 5 describes the flow patterns maps and finally Section.6 shows and discusses the results of the non-dimensional model developed in this work for both model and experimental data.

6.1 Artificial Neural Network

Artificial neural networks ANN have proven to be effective tool in modeling complex physical relations. ANNs are composed of signal processing elements called neurons. The neurons are interconnected and the strength of the interconnections are denoted by parameters called synaptic weights. The model of a neuron is shown in Figure 6-1.

where $x_1, x_2, \ldots, x_p$ are the input signals, $w_{k1}, w_{k2}, \ldots, w_{kp}$ are the synaptic weights of neuron k, w_{k0} is the bias, v_k the linear combiner output, $f(.)$ is an activation function, and y_k is the output signal of the neuron.
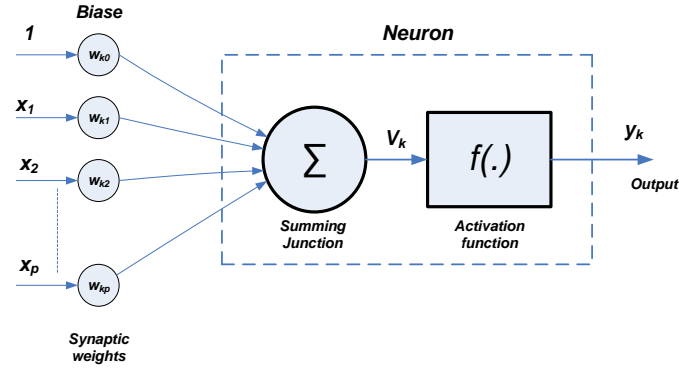
Figure 6-1: Model of a neuron.

In mathematical form the k-th neuron is described as:

$$v_k = \sum_{j=1}^{p} w_{kj} x_j + w_{k0} \tag{6.1}$$

$$y_k = f(v_k) \tag{6.2}$$

The activation function, $f(.)$, defines the output of a neuron in terms of the activity level at its input. There are several classes of artificial neural networks structures. The most common structure of ANN is known as Feed Forward Neural Networks (FFNN). FFNNs are composed of layers of interconnected neurons. Usually, an input layer, number of hidden layers and an output layer are used as shown in Figure 6-2 [104]. The input layer is essentially a direct link to the inputs of the first hidden layer. The output of each neuron may be connected to the inputs of all the neurons in the next layer. Signals are unidirectional i.e., they flow only from input to output.
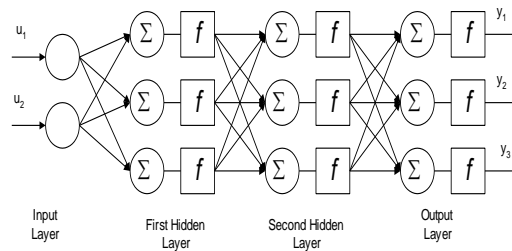
Figure 6-2: Multi-layer feed-forward neural network (FFNN).

The potential of FFNN as a basis for the modeling, classification, and statistical estimation stems from the following characteristics:

- For a sufficient number of hidden units, feed-forward neural networks (FFNN) can approximate any continuous static input-output mapping to any desired degree of approximation. [104, 105]

- Due to the modular and feed-forward structure, the training of the network is simple and can be made to adapt to varying conditions.

The back propagation (BP) algorithm is usually used for (FFNN) training [104, 106, 107, 108]. Although BP is simple, the choice of a good learning rate requires some trial and error. Several improved variants of the BP algorithms were proposed in the literatures. We used Scaled Conjugate Gradient Back propagation algorithm as in [109]. During training, only the class output corresponding to the input data will have a target of 1, while the other outputs will have a target of zero. During the classification operation, the output with the highest score is taken to be the identified class.

6.2 Flow Patterns

Four multiphase flow patterns are considered in this work, namely; Stratified, Dispersed Bubbles, Intermittent, and Annular as shown in Figure 6-3.

1. **Stratified Flow (STR)**: Liquid and gas phases are completely separated and flow at low velocity.

2. **Dispersed Bubble flow (DB)**: High liquid rate and low gas rate moving as Dispersed bubble in the liquid phase.

3. **Intermittent Flow (INT)**: This flow pattern starts to form as the gas velocity increases and interfacial wave amplitude becomes large. It can be divided into two sub-flow patterns: Slug Flow and Plug flow. In plug flow, there are elongated bubbles flow at the top of the pipe but the liquid phase is continuous. As, the gas velocity increase, the elongated bubbles diameter reaches to the height of the pipe.

4. **Annular Flow (AN)**: At high gas velocity, the liquid is forced to move along the pipe wall as a film and gas flows in the core.
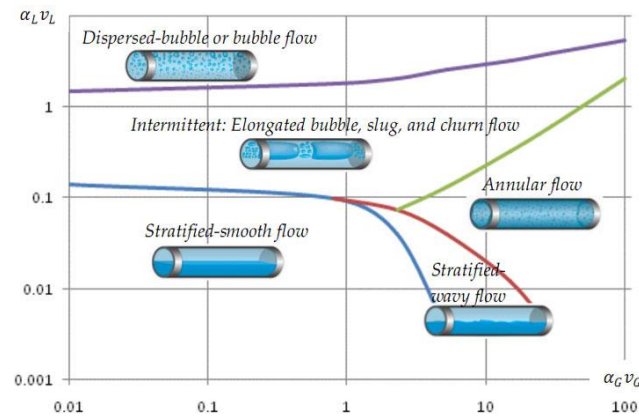
Figure 6-3: Gas-liquid flow pattern map in a horizontal. [5]

6.3 Unified Model

The unified model is used for generating data for testing various flow classification techniques. Zhang and Sarica [110], and Zhang et al. [111] proposed a unified model for prediction of gas-oil-water flow behavior in wellbores and pipelines based on Slug dynamics. This model describes three-phase flow based on two criteria: gas-liquid flow pattern and oil-water mixing status. The three-phase flow was treated as gas-liquid two-

phase flow if the two liquids are fully mixed or as a three-layer Stratified flow at low flow rates in horizontal or slightly inclined pipes. Closure relationships describing the distribution between the two liquid phases were proposed. Experimental data for gas-oil-water pipe flow from many studies in literature were used to validate the model. The Zhang et al. [111] flow pattern map in the unified model was compared also with Taitel and Dukler [15] gas-liquid flow pattern maps and showed excellent agreement. Due to the confidence received by unified model in literature, it was decided to use the resulted data from the Unified model to train our ANN in this study.

6.4 Flow Pattern Maps

There are many flow pattern maps used to determine flow patterns using different multiphase flow parameters. Superficial velocities of liquid and gas are the most popular used parameters on the two-dimensional axis's of the map. Superficial velocity of liquid and gas can be defined as:

$$V_{SL} = \frac{q_L}{A} \tag{6.3}$$

$$V_{SG} = \frac{q_G}{A} \tag{6.4}$$

where q_L and q_G are volume flow rates of the liquid and gas respectively. Liquid hold is another important multiphase flow parameter, which can be defined:

$$H_L = \frac{A_L}{A} \tag{6.5}$$

where A is pipe cross sectional area and A_L is the cross sectional area occupied by liquid.

Another multiphase flow parameter is the pressure gradient

$$\frac{dP}{dx} = \frac{dP}{dx_{acc}} + \frac{dP}{dx_{fric}} + \frac{dP}{dx_{ga}}$$ (6.6)

where

$\frac{dP}{dx_{acc}}$ is the accelerational pressure gradient .

$\frac{dP}{dx_{fric}}$ is the frictional pressure gradient.

$\frac{dP}{dx_{ga}}$ is the gravitational pressure gradient.

However, these maps depend on dimensional parameters which means they work for a certain pipe diameter and flow conditions. Reynolds numbers for gas and liquid are candidate parameters that can be used to develop dimensionless maps

$$\boldsymbol{Re_G} = \frac{\rho_G V_{SG} D}{\mu_G}$$ (6.7)

$$\boldsymbol{Re_L} = \frac{\rho_L V_{SL} D}{\mu_L}$$ (6.8)

where

ρ_G , ρ_L are densities of gas and liquid, respectively.

μ_G, μ_L are viscosities of gas and liquid, respectively.

Since pressure gradient is one of the most important parameter in multiphase flow, a dimensionless parameter called Pressure Drop Multiplier $\emptyset_{LO}^2$ will be used in the present work. This parameter can be defined as the multiphase flow pressure drop (measured or calculated from models) divided by the calculated single phase liquid pressure gradient [112].

The following are the steps to calculate the pressure drop multiplier based on the liquid phase:

1) Calculate single phase friction factor by calculating first single phase (Liquid) Reynolds number. The friction factor correlation for smooth pipe is given as

   $f = C.Re_L^{-n}$, where C=64, n=1 for laminar flow, and C=0.316, n=0.25 for turbulent.

2) Use the above correlations based on the value of Re Laminar <2000 or turbulent Re>2300

3) Calculate

$$\left(\frac{dp}{dL}\right)_{Lo} = \frac{f.\rho_L.V_{SL}^2}{2D} \tag{6.9}$$

Then, two phase frictional multiplier will be as in Equation (4-10)

$$\emptyset_{Lo}^2 = \left[\frac{dP}{dL}\right]_{TP} / \left[\frac{dP}{dL}\right]_{Lo} \tag{6.10}$$

where *D* is pipe diameter, *TP* refers to two phase, *Lo* refers Liquid Only.

6.5 Results and Discussion

In this work, we used unified model simulator to generate the data for training and testing the Neural Network to cover a wide range of flow conditions which is not easy to be covered by experiments. Four cases are simulated. In case 1, we simulated one horizontal pipe with dimensional parameters sets and two cases with dimensionless sets. In case two, we did a simulation of horizontal pipes with different diameters. In case 3, we added another two parameters, namely, viscosity and density. In case 4, we used an experimental data to build the model using the same dimensionless parameters set. In all cases, we simulated two phases: liquid and gas. In this simulation, we consider four flow patterns: Stratified (STR), Dispersed Bubbles (DB), Intermittent (INT), and Annular (AN).

6.5.1 One Horizontal Pipe

In this case, we studied a horizontal pipe with diameters of 1 inch, and used 946 points divided as follows: 277 for Annular, 264 for Dispersed Bubble, 252 Intermittent and 153 for Stratified. The data is divided into 70% for training, 15 % for validation and 15 % for testing. Simulation was done using Neural Network Toolbox in MATLAB .In each case, the Neural Network model has 2 inputs, one hidden layer with 20 neurons, and 4 outputs. We considered the following pairs of multiphase parameters; (V_{SG}, V_{SL}), Total pressure drop (DP) and liquid hold (H_L), and the Reynolds numbers for the liquid and gas flows (Re_G, Re_L). Since Neural Network cannot handle nonnumeric outputs, we represented the flow patterns with the target numeric values shown in Table 6-1.

Table 6-1: Numerical representation of flow patterns.

Flow Pattern	Numerical Value
Annular	1000
Dispersed Bubble	0100
Intermittent	0010
Stratified	0001

Different configuration of input parameters are used in neural networks model:

1- Gas Superficial Velocity (V_{SG}) & Superficial velocity of liquid (V_{SL}).

2- Natural Logarithmic of V_{SG} and V_{SL}.

3- Total Pressure Drop (DP) & Liquid Hold Up (H_L).

4- Natural Logarithmic of DP and H_L.

5- Liquid Reynolds Number Re_L & Gas Reynolds Number Re_G.

6- Natural Logarithmic of Re_L, Re_G.

Figure 6-4 indicates some regions of overlapping and critical parameter values for flow patterns. For example, the overlapping of Intermittent flow and Stratified flow at low liquid superficial velocity can easily cause pattern identification errors. On the other hand, in some cases a small change in a critical parameter could trigger change of flow patterns. For example, at $V_{SL}=4$ a change of gas velocity from 12 to 13 can cause the flow pattern to change from bubbles to Intermittent. As such, identification errors could easily happen due to measurement noise in the gas velocity at these critical values.

For the (DP,H_L) pair, the range of the flow patterns is depicted in Figure 6-5. Clearly, the situation is much worst with clear overlapping between the Stratified and Intermittent at low pressure drop values, and overlapping between Annular and Intermittent at low liquid hold up values. Similar behavior was observed when we examined the range of the parameter pairs (Re_G, and Re_L). Another issue for Reynolds number is the unbalance data distribution along large range as shown in Figure 6-6.

Next we studied the possibility of using nonlinear mapping of the flow parameters to improve the separation between the regions of the flow patterns. We reported here the result of taking the natural logarithm. Figure 6-7 shows the regions of the four flow patterns using Ln (V_{SG}) and Ln (V_{SL}). Figure 6-7 shows a clear separation of the regions for each of the considered flow patterns. A more impressive result was observed when we considered the (Ln (DP), Ln (H_L)) as shown in Figure 6-8. In fact, the observed overlapping between Intermittent and Stratified disappeared.

In the case of the Reynolds number pairs, the logarithmic mapping not only helps to have better separation between the regions of the patterns, but also provides efficient scaling of the parameter range as shown in Figure 6-9. Table 6-2 shows the results of flow patterns prediction using different configuration of input parameters sets. Improvement in flow

103

patterns identification can be noticed using natural logarithmic of original parameters. For V_{SL} and V_{SG}, the improvement is 3.5 %, for DP and H_L is 13.4 % and for Re_L and Re_G is 4.9 %.

Table 6-2: Percent of correct classification.

Parameter/ Pattern	% Correct Classification				
	AN	DB	INT	STR	Total
V_{SG} , V_{SL}	97.5 %	100.0%	87.5 %	96.0 %	95.1 %
$Ln(V_{SG})$, $Ln(V_{SL})$	97.8 %	100.0 %	97.4 %	100.0 %	98.6%
DP , H_L	88.2 %	98.0 %	79.4 %	54.2 %	83.8 %
$Ln(DP)$, $Ln(H_L)$	100.0 %	95.3 %	97.1 %	95.7 %	97.2%
Re_L, Re_G	97.8 %	92.3 %	84.8 %	96.0 %	93.0 %
$Ln(Re_L)$, $Ln(Re_G)$	100.0 %	97.2.0%	94.9 .0 %	100.0 %	97.9 %

As can be seen in the confusion matrices in Table 6-3 based on the tested data, the first common thing is that confusion is reduced by using natural logarithmic. For all flow patterns, the total confusion is reduced by using the normalized inputs.

Table 6-3: Incorrect Classification:

(a) V_{SG} & V_{SL}, (b) Ln (V_{SG}) & Ln (V_{SL}). (c) DP & HL, (d) Ln (DP) & Ln (HL), (e) Re_G & Re_L, (f) Ln (Re_G) & Ln (Re_L).

	% Incorrect Classification			
	AN	DB	INT	STR
AN	-------	0 %	0%	4.0 %
DB	0 %	-----	2.5 %	0 %
INT	0 %	0 %	-----	0 %
STR	2.5 %	0 %	10.0 %	---------

Total	2.5 %	0 %	12.5 %	4.0%

(a)

	% Incorrect Classification			
	AN	DB	INT	STR
AN	----------	0 %	0%	0 %
DB	0 %	----------	2.6 %	0 %
INT	2.2 %	0 %	----------	0 %
STR	0 %	0 %	0 %	----------
Total	2.2 %	0 %	2.6 %	0 %

(b)

	% Incorrect Classification			
	AN	DB	INT	STR
AN	----------	0 %	0 %	29.2 %
DB	0 %	----------	5.9 %	0 %
INT	0 %	2.0 %	----------	16.7 %
STR	11.8 %	0 %	14.7 %	----------
Total	11.8 %	2.0 %	20.6 %	45.8%

(c)

	% Incorrect Classification			
	AN	DB	INT	STR
AN	----------	0 %	2.9 %	4.3 %
DB	0 %	----------	0 %	0 %
INT	0 %	4.7 %	----------	0 %
STR	0 %	0 %	0 %	----------
Total	0 %	4.7 %	2.9 %	4.3 %

(d)

	% Incorrect Classification

	AN	DB	INT	STR
AN	----------	0 %	0 %	4.0 %
DB	0 %	----------	6.1 %	0 %
INT	2.2 %	7.7%	----------	0 %
STR	0 %	0 %	9.1 %	----------
Total	2.2 %	7.7 %	15.2 %	4.0 %

(e)

	% Incorrect Classification			
	AN	DB	INT	STR
AN	----------	0 %	2.56%	0 %
DB	0 %	----------	2.56 %	0 %
INT	0 %	2.8 %	----------	0 %
STR	0 %	0 %	0 %	---------
Total	0 %	0 %	5.1%	0 %

(f)

These results are based on random points selected from the data. Since the transition between flow patterns is one of the main confusion reasons, we need to look to the transition points and show the improvement in this region due to the natural logarithmic normalization. There are 18 data points at the transition between flow patterns in this data set. Table 6-4 shows the percentage of misclassified points for each case. Although natural logarithmic does not remove confusion at transition completely but the improvement using natural logarithmic normalization is very clear.

Table 6-4: Misclassified percentage at transition region.

Parameters	Percentage of misclassified
V_{SG} , V_{SL}	50 %
$Ln(V_{SG})$, $Ln(V_{SL})$	16.7 %

DP , H_L	55.6 %
Ln(DP), Ln(H_L)	38.9 %
Re_L, Re_G	38.9 %
Ln(Re_L), Ln(Re_G)	22.2 %
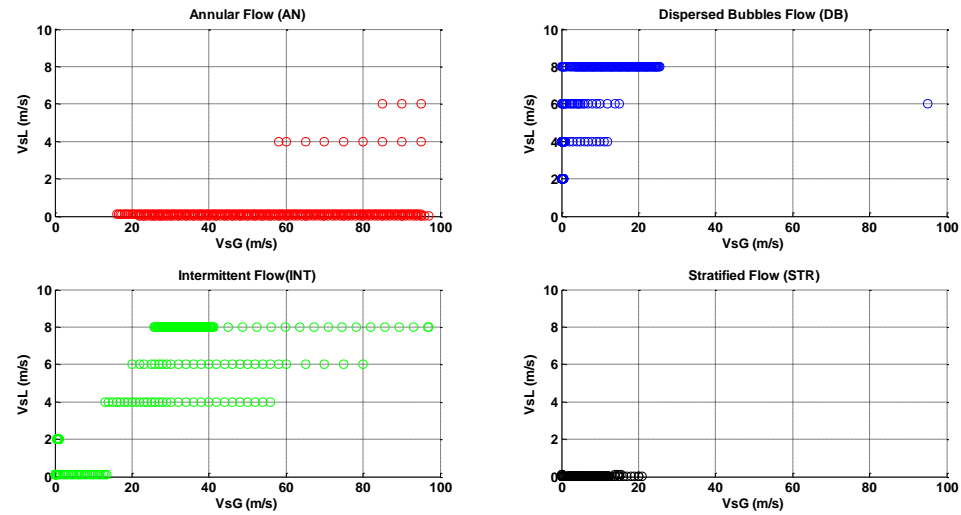
Figure 6-4: Regions of the four flow patterns using (V_{SG}, V_{SL}).
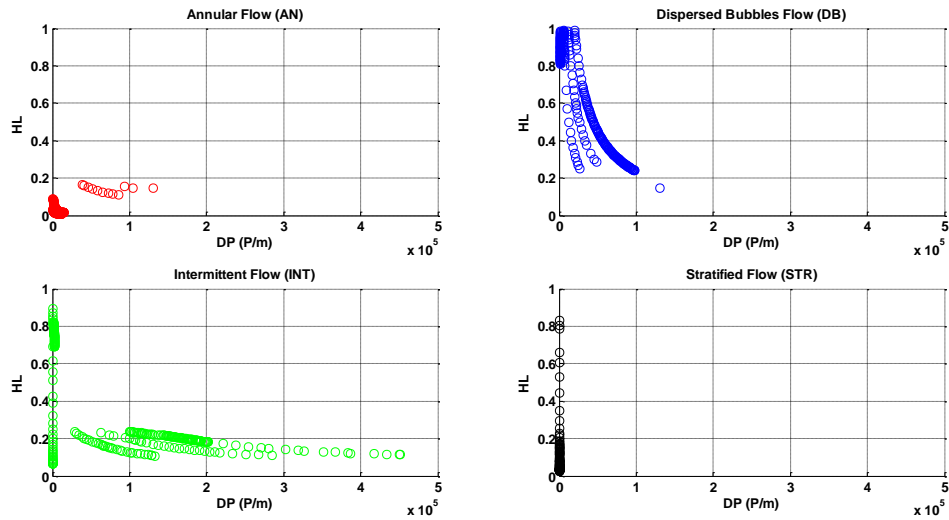
Figure 6-5: Regions of the four flow patterns using (DP, H_L).
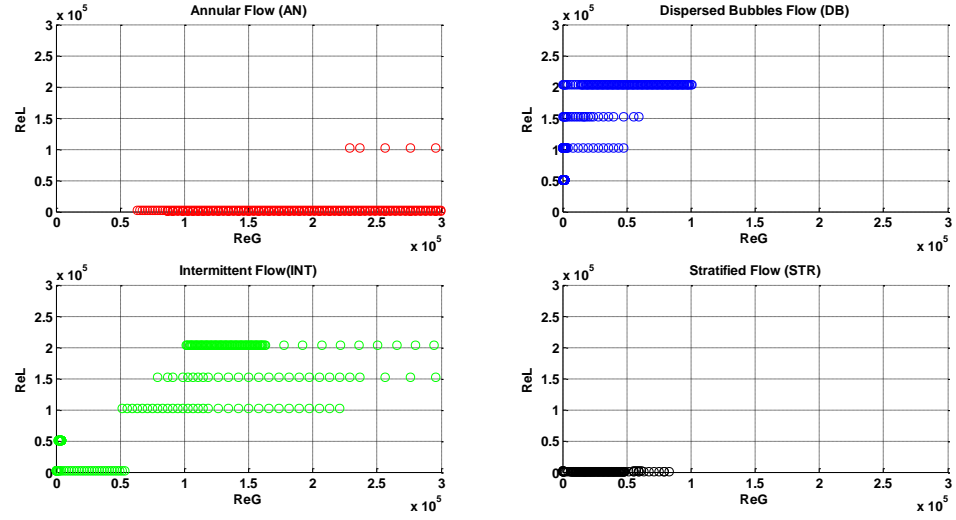
Figure 6-6: Regions of the four flow patterns using (Re$_G$, Re$_L$).
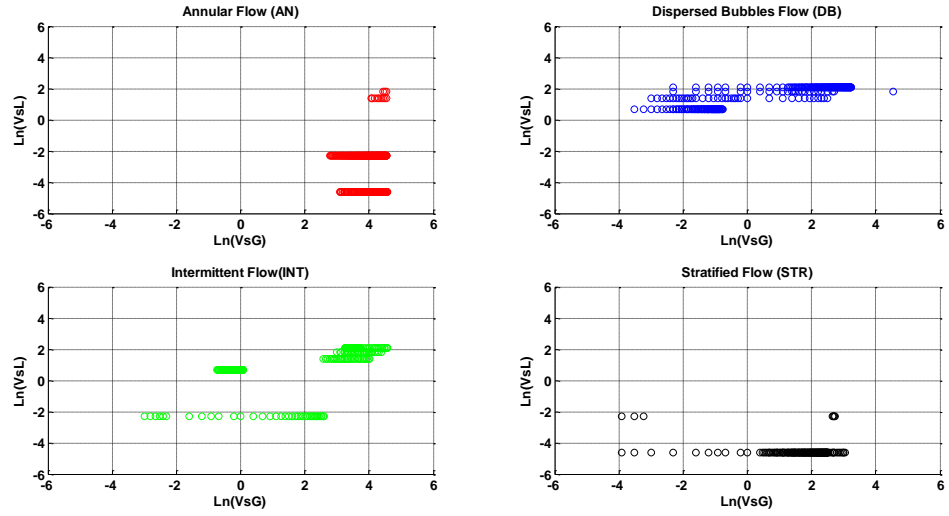
Figure 6-7: Regions of the four flow patterns using the natural logarithm of (V$_{SG}$, V$_{SL}$).
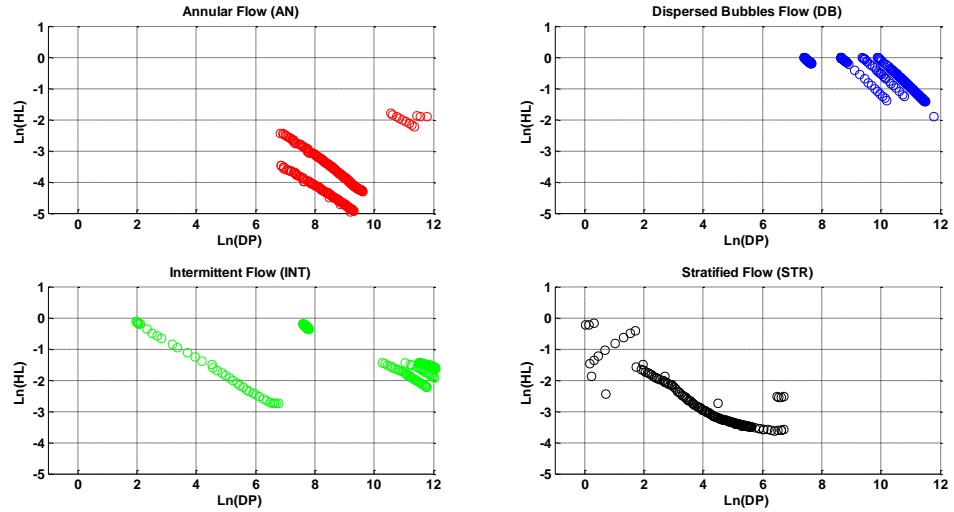
Figure 6-8: Regions of the four flow patterns using the natural logarithm of (DP, H_L).
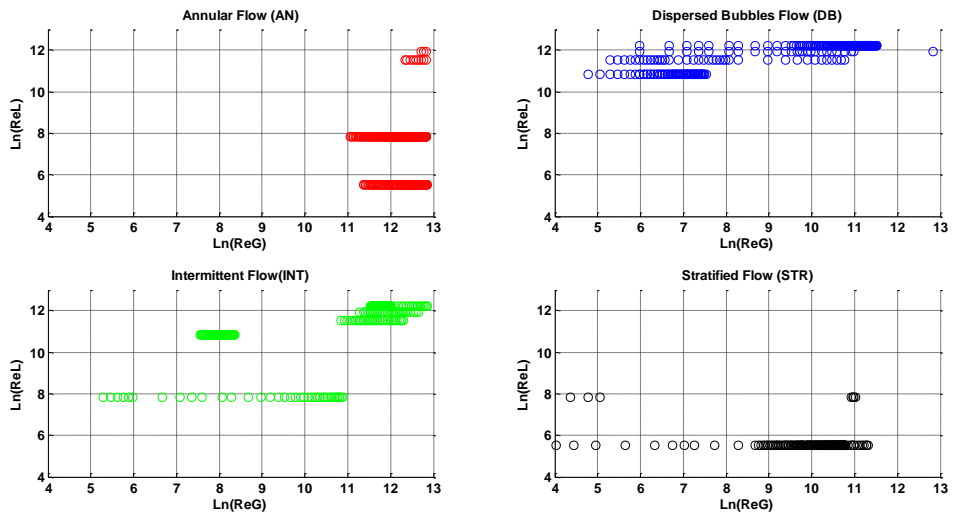
Figure 6-9: Regions of the four flow patterns using the natural logarithm of (Re_G, Re_L).

6.5.2 Horizontal Pipes with Different Diameters

In this case, six horizontal pipes with diameter 0.5 inch, 1 inch, 2 inch, 3 inch, 4 inch, 5 inch were examined. In this simulation, we used 5676 points divided as follow: 1135 for

Annular, 1575 for Dispersed Bubble, 1492 Intermittent and 1474 for Stratified. These points are divided as follow: 70 % for training, 15 % for validation, 15 for % testing.

Since there are different pipes diameters, we need to use dimensionless parameters. Four different input configurations are tested in this simulation:

1- Re_L, Re_G

2- Ln (Re_L), Ln (Re_G).

3- Re_L, Re_G, $\emptyset_L^2$.

4- Ln(Re_L), Ln(Re_G), Ln($\emptyset_L^2$)

The Neural Network model has two inputs for configuration 1 and 2 and three inputs for configuration 3 and 4, one hidden layer with 80 neurons, and four outputs. Looking to Reynolds number flow pattern map, It can be seen that there is overlapping between flow patterns at liquid Reynolds numbers values especially between Annular and Stratified flow as shown in Figure 6-10 (a).

The confusion can be seen clearly in the confusion matrices as shown in Table 6-5 (a) and the effect of overlapping on the correct flow patterns classification as shown in Table 6-6. Annular flow has low correct classification percentage due to overlapping mainly with Stratified flow and Intermittent. Dispersed bubble has confusion with other flow patterns. Figure 6-10 (b) shows the effect of natural logarithmic normalization in normalizing the data and reducing the overlapping between flow patterns. Table 6-5 (b) shows the great improvement using normalized data to reduce the misclassification percentage between flow patterns to about 6.3 % for Annular, 3.9 % for Dispersed Bubble, 2.84 % for Intermittent and 8.1 % for Stratified as shown in Table 6-5 (b). For flow pattern map based on three parameters, the classification accuracy is improved by adding the

pressure drop multiplier to the map but the misclassification percentage is still high due to overlapping between flow patterns especially at low values of the three parameters as shown in Figure 6-11 (a) & Figure 6-12 (a). Using natural logarithmic normalization, the overlapping between flow patterns is greatly reduced as shown in Figure 6-11 (b) & Figure 6-12 (b). Table 6-5 (d) shows that misclassification percentage is reduced to about 2 % using natural logarithmic normalization compared to relativity high misclassification percentage using the original three parameters as shown in Table 6-5 (c).

(a)   (b)

Figure 6-10: Regions of the four flow patterns of multiple pipes using: (a) Re$_G$, Re$_L$ for multiple pipes, (b) Natural logarithmic of (Re$_G$, Re$_L$).
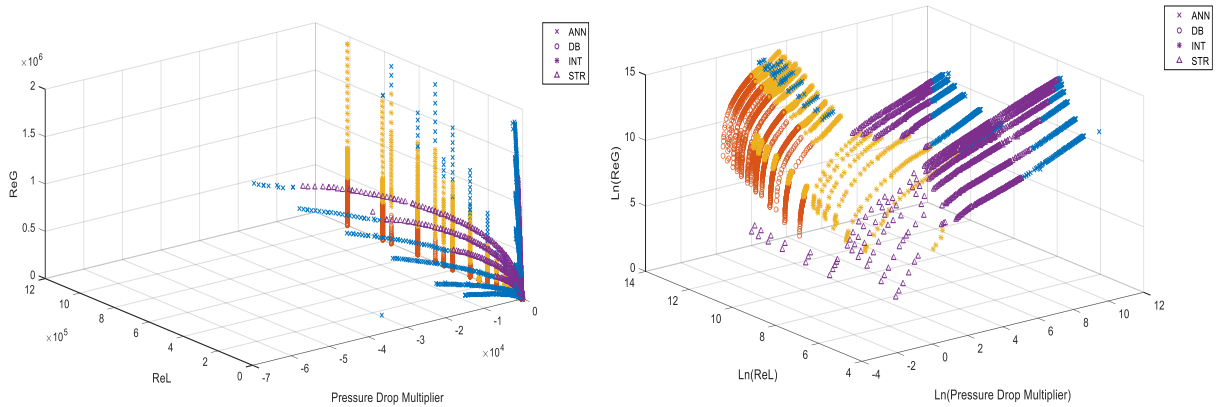
Figure 6-11: Flow patterns map using (a) Re$_G$, Re$_L$ and $\emptyset_L^2$ for multiple pipes, (b) Natural logarithmic of (Re$_G$, Re$_L$ and $\emptyset_L^2$)

111

(a)   (b)
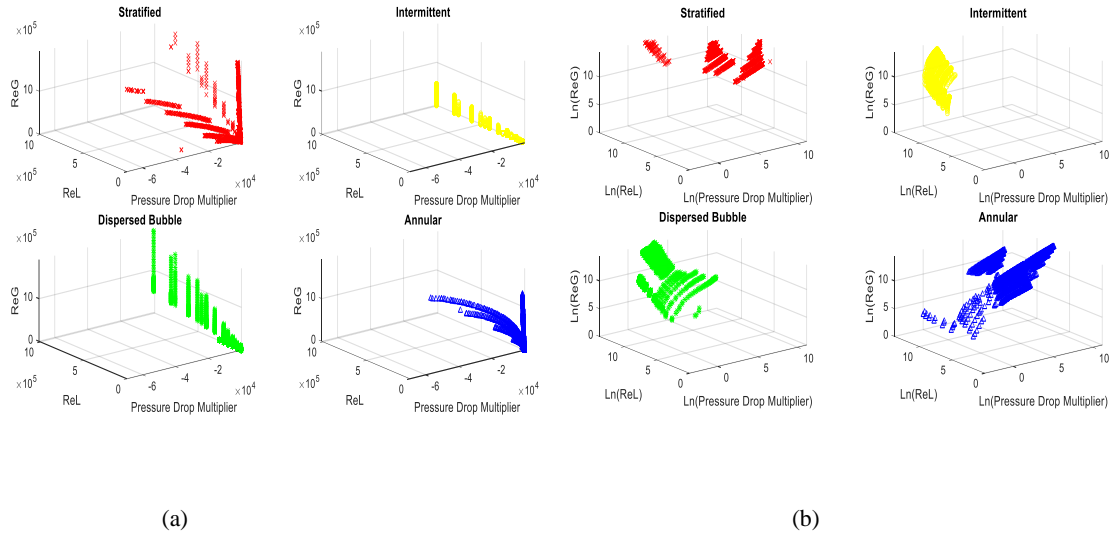
Figure 6-12: Regions of the four flow patterns using: (a) Re$_G$, Re$_L$ and $\emptyset_L^2$ for multiple pipes, (b) Natural logarithmic of (Re$_G$, Re$_L$ and $\emptyset_L^2$).

Table 6-6 summarized correct classification percentage for four configurations. As shown in this analysis, adding the pressure drop multiplier as a third parameter to the flow patterns map is very useful to improve multiphase flow patterns identification.

Table 6-5: Incorrect classification %: (a) Re$_G$, Re$_L$,(b) Ln (Re$_L$), Ln (Re$_G$) , (c) Re$_L$, Re$_G$,$\emptyset_L^2$,(d) Ln(Re$_L$), Ln(Re$_G$), Ln($\emptyset_L^2$).

	% Incorrect Classification			
	AN	DB	INT	STR
AN	---------	10.6 %	6.0 %	7.13 %
DB	3.57 %	--------	16.13 %	1.83 %
INT	16.1 %	11.3 %	---------	12.33 %
STR	54.2 %	15.7 %	27.2%	---------
Total	73.8 %	44.5%	49.3 %	21.5 %

(a)

	% Incorrect Classification			
	AN	DB	INT	STR

	AN	DB	INT	STR
AN	---------	0 %	1.42 %	4.74 %
DB	0.0 %	--------	1.42 %	0 %
INT	2.3 %	3.9 %	---------	3.32 %
STR	4.0 %	0 %	0.0 %	---------
Total	6.3 %	3.9 %	2.84 %	8.1%

(b)

	% Incorrect Classification			
	AN	DB	INT	STR
AN	---------	0.0 %	0.5 %	15.5 %
DB	0 %	---------	15.4 %	0 %
INT	1.4 %	13.0 %	---------	0.43 %
STR	32.9 %	0 %	12.6 %	---------
Total	34.3 %	13.0 %	28.5%	15.9 %

(c)

	% Incorrect Classification			
	AN	DB	INT	STR
AN	---------	%	0.44 %	0.0 %
DB	0.0 %	--------	1.32 %	0.0 %
INT	0.0 %	1.6 %	---------	0.0 %
STR	0.0 %	0.0 %	0.44 %	---------
Total	0.0 %	1.6 %	2.2 %	0.0 %

(d)

Table 6-6: Percent of correct classification.

	% Correct Classification				
Parameter/ Pattern	AN	DB	INT	STR	Total
Re_L, Re_G	26.2 %	55.5 %	50.7 %	78.5%	54.4 %

Ln(Re$_L$), Ln(Re$_G$)	93.7 %	96.1 %	97.2 %	91.9 %	94.8 %
Re$_L$, Re$_G$,$\emptyset_L^2$	65.7 %	87.0 %	71.5 %	84.1 %	78.7%
Ln(Re$_L$), ln(Re$_G$), ln($\emptyset_L^2$)	100.0 %	98.4 %	97. 8%	100.0 %	98.9 %

Next, the model is examined in the transition region since the transition between flow patterns is one of confusion reasons. 139 data points at the transition between flow patterns are examined. Table 6-7 shows the number of misclassified points for each case. Misclassification percentage is very high using original parameters but using the normalized parameters, the percentage is greatly reduced. Although natural logarithmic does not remove confusion at transition completely but the improvement using natural logarithmic normalization is very clear.

Table 6-7: Misclassified percentage at transition region.

Parameters	Percentage of misclassified
Re$_L$, Re$_G$	61.9%
Ln(Re$_L$), Ln(Re$_G$)	26.6 %
Re$_L$, Re$_G$, $\emptyset_L^2$	44.6 %
Ln(Re$_L$), ln(Re$_G$),ln($\emptyset_L^2$)	4.3 %

6.5.3 Horizontal Pipe with Different Diameters and Liquid Viscosities and Densities

In the previous section, a dimensionless model is built for various pipe diameters for air and water only. In this section, the model is extended to include different fluids with different viscosities and densities. A dataset consisting of 17,028 points is used to develop the extended model. 3497 data points for Annular, 5265 data points for Dispersed Bubble , 5608 data points for Intermittent and 2658 for Stratified .The viscosities of the fluid range from 1 cp (Water) up to 300 cp (High Viscous oil). Also, the density is another variable in this case: Water density 998 kg/m^3, Oil density 880 kg/m^3.

Similar to case 2, four different input configurations are tested in this simulation:

1. Re$_L$, Re$_G$

2. Ln (Re$_L$), Ln (Re$_G$).

3. Re$_L$, Re$_G$, $\emptyset_L^2$.

4. Ln (Re$_L$), Ln (Re$_G$), Ln ($\emptyset_L^2$).

The Neural Network model has 2 inputs for configuration 1 and 2, 3 inputs for configuration 3 and 4, one hidden layer with 100 neurons, and 4 outputs.

Looking to Reynolds number flow pattern map, we can see the overlapping between flow patterns at low Reynold numbers values for all flow patterns as shown in Figure 6-13 (a). The confusion between flow patterns is clearly shown in confusion matrices in Table 6-8 (a) and the effect of overlapping on correct flow patterns classification is shown in Table 6-9. All flow patterns have low correct classification percentage due to overlapping. Figure 6-13 (b) shows the effect of natural logarithmic normalization in normalizing the data and reducing the overlapping between flow patterns.
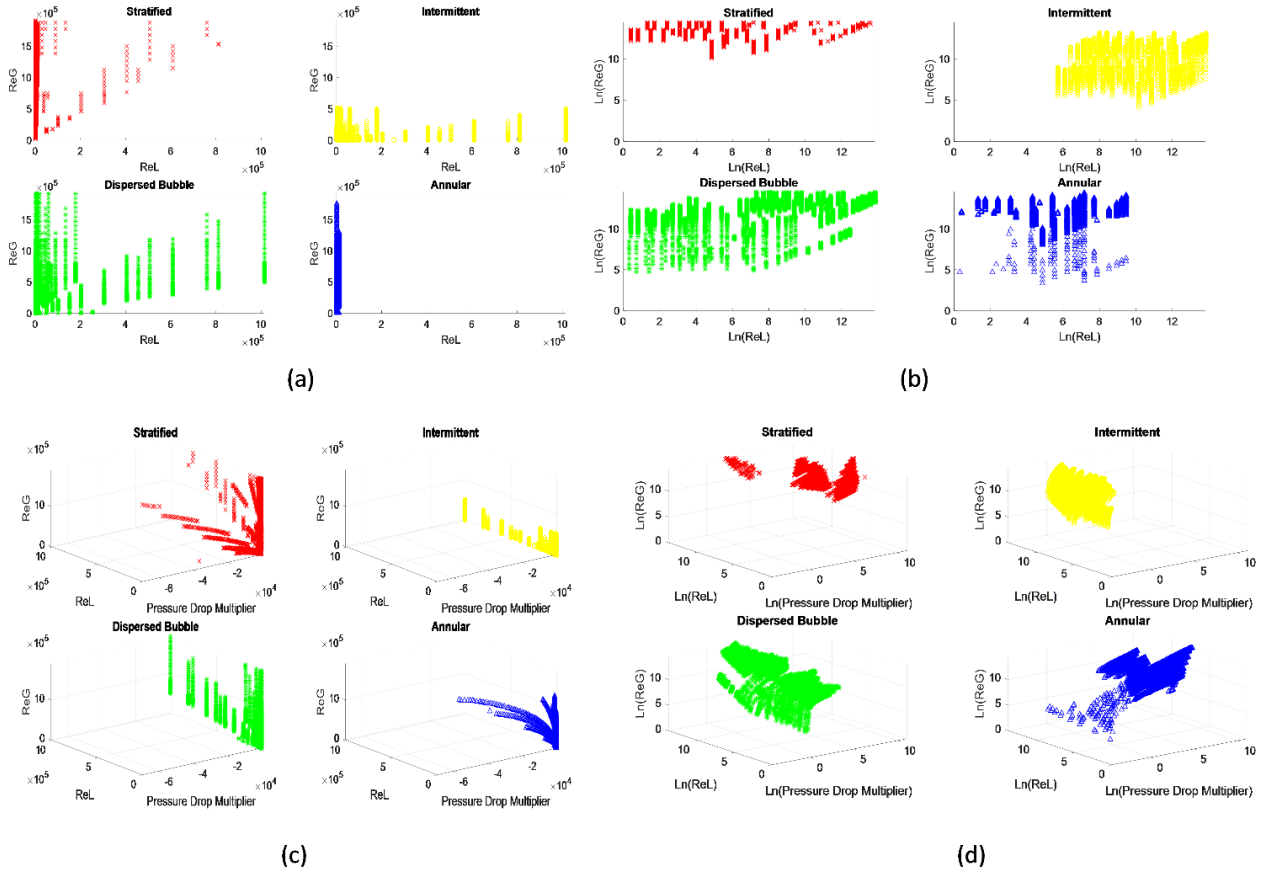
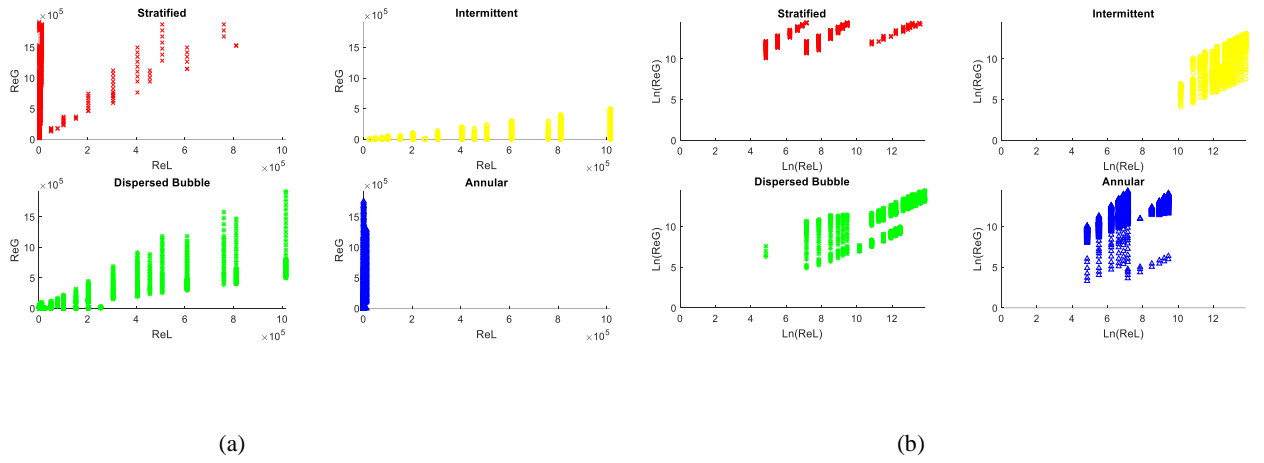Figure 6-13: Regions of the four flow patterns using: (a) Re$_G$, Re$_L$ for multiple pipes, (b) Natural logarithmic of (Re$_G$, Re$_L$) (c) Re$_G$, Re$_L$ and $\emptyset_L^2$ for multiple pipes, (d) Natural logarithmic of (Re$_G$, Re$_L$ and $\emptyset_L^2$).

Table 6-8 (b) shows the improvement using normalized data to reduce the misclassification percentage between flow patterns to about 24.25 % for Annular, 15.3 % for Dispersed Bubble, 23.2 % for Intermittent and 49.7 % for Stratified but it is not as good as previous case which indicates that Reynolds number is not enough to cover the wide range dataset. Looking to the flow pattern map based on three parameters, we can see also the overlapping between flow patterns as shown in Figure 6-13 (c) while the overlapping is greatly reduced using natural logarithmic normalization as shown in Figure 6-13 (d). Table 6-8 (c) shows an improvement by introducing the pressure drop multiplier to map but with applying the normalization to original parameters, the misclassification percentage is

116

greatly reduced to less than 5 % as shown in Table 6-8 (d). Table 6-9 summarized correct classification percentage for four configurations. As shown in this analysis, adding the pressure drop multiplier as a third parameter to the flow patterns map is very useful to improve multiphase flow patterns identification and extend the validity of the model for wider data range. Looking to the performance of the model at the transition region in Table (10), 14.8 % improvement in case of normalized Reynold numbers and 26 % improvement in case of the normalized three parameters compared to the original parameters. The improvement in this case at transition region is not as good as the case 2 due to the extremely wide range flow conditions tested which is difficult to be covered completely by a single model. So, reducing the overlapping to about 20 % in the transition region for this wide range of flow conditions is really a good achievement.

Table 6-8: Incorrect classification %: (a) Re$_G$, Re$_L$,(b) Ln (Re$_L$), Ln (Re$_G$) , (c) Re$_L$, Re$_G$,$\emptyset_L^2$,(d) Ln(Re$_L$), Ln(Re$_G$), Ln($\emptyset_L^2$).

	% Incorrect Classification			
	AN	DB	INT	STR
AN	---------	5.28 %	13.66 %	23.4 %
DB	0.76 %	--------	36.65 %	25.12%
INT	25.38%	17.91%	---------	16.34 %
STR	13.93 %	0 %	1.5 %	---------
Total	40.1 %	23.2%	51.8 %	64.9 %

(a)

	% Incorrect Classification			
	AN	DB	INT	STR
AN	---------	1.12 %	7.5 %	23.48 %
DB	5.25 %	--------	9.26 %	6.57 %

	AN	DB	INT	STR
INT	10.1 %	11.6 %	--------	19.7%
STR	8.9 %	2.59 %	6.45 %	--------
Total	24.25 %	15.3%	23.2%	49.7%

(b)

	% Incorrect Classification			
	AN	DB	INT	STR
AN	---------	1.84 %	6.7 %	1.2 %
DB	0.0 %	---------	10.6 %	0.8 %
INT	5.5 %	21.4 %	---------	38.42 %
STR	15.6 %	0 %	1.63 %	---------
Total	21.1 %	19.4 %	19.0%	40.42 %

(c)

	% Incorrect Classification			
	AN	DB	INT	STR
AN	---------	0 %	0.36 %	1.0 %
DB	0 %	--------	3.0 %	0.5 %
INT	0.8 %	1.73%	---------	2.77 %
STR	0.2 %	0 %	0.84 %	---------
Total	1.0 %	1.73 %	4.2 %	4.3 %

(d)

Table 6-9: Percent of correct classification.

	% Correct Classification				
Parameter/ Pattern	AN	DB	INT	STR	Total
Re_L, Re_G	59.9%	76.8 %	71.9 %	35.1%	57.6 %
$Ln(Re_L)$, $Ln(Re_G)$	75.8 %	84.70%	76.8 %	50.3 %	75.0 %
Re_L, Re_G, $\emptyset_L^2$	78.9 %	76.8%	81.0 %	41.1 %	73.3 %

Ln(Re$_L$), Ln(Re$_G$) , Ln($\emptyset_L^2$)	99.0 %	98.3 %	95. 8%	95.7 %	97.2 %

Table 6-10: Misclassified percentage at transition region.

Parameters	Percentage of misclassified
Re$_L$, Re$_G$	64.8 %
Ln(Re$_L$), Ln(Re$_G$)	51.0 %
Re$_L$, Re$_G$, $\emptyset_L^2$	47.0%
Ln(Re$_L$), ln(Re$_G$),ln($\emptyset_L^2$)	21.0 %

6.5.4 Experimental Data

In this case, an experimental data is used to build the dimensionless model and verify the proposed technique using actual data. The reference for the data is Brito, R. (2012) experimental work [113]. In this experiment, two phase flow of oil and air have been investigated at experimental facility shown in Figure 6-14. Test section has two 59.8 ID pipes: 9.75 m long PVC pipe and 9.15 m long transparent acrylic pipe. Medium viscosity mineral oil, DN-20, with different viscosities ranged from 38 cp up to 166 cp .The physical properties of DN-20 mineral oil are: API Gravity: 30.5 @ 60 °F, Density: 873 kg/m^3 @ 60 °F, Surface Tension: 27.5 dynes/cm @ 60 °F, Flash Point Temperature: 435 °F, and Pour Point Temperature: -5 °F. Superficial oil and gas velocities are varied between 0.01 m/s to 3.0 m/s and 0.1 m/s to 9.0 m/s, respectively.
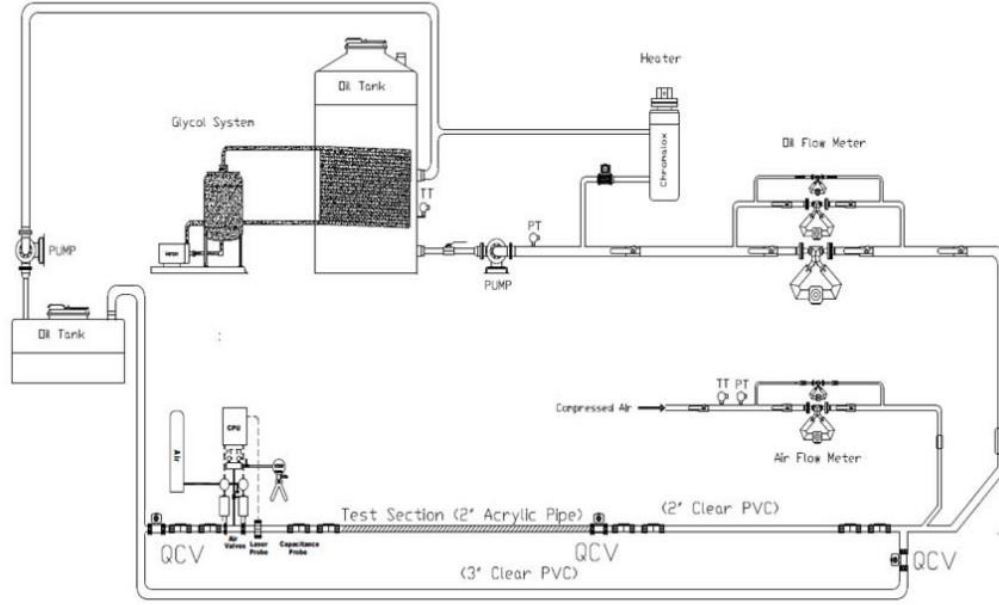
In this experiment set, there are 376 points divided between the four flow patterns (some points are artificially to make balance between flow regimes). Similar to case 2 and 3, four input configurations are used:

1. Re_L, Re_G

2. Ln (Re_L), Ln (Re_G).

3. Re_L, Re_G, $\emptyset_L^2$.

4. Ln(Re_L), Ln(Re_G), Ln($\emptyset_L^2$)

The Neural Network model has two inputs for configuration 1 and 2, three inputs for configuration 3 and 4, one hidden layer with 20 neurons, and four outputs.

Similar to the previous cases, Figure 6-15 (a, c) shows the overlapping between flow patterns while Figure 6-15 (b, d) shows the enhancement of flow patterns identification accuracy using the natural logarithmic normalization. Table 6-11 (a) shows high

misclassification percentage between flow patterns using only Reynolds numbers while Table 6-11 (c) shows a slight improvement by adding the pressure drop multiplier to the map. Looking to Table 6-11 (b, d), the percentage of misclassification is greatly reduced using logarithmic normalization of the original parameters. Table 6-12 summarizes the percentage of correct classification for the four configurations. It shows 11 % - 13 % improvement in flow patterns classification using normalized parameters over the original parameters.

Finally, Table 6-13 shows the misclassification percentage for the four configurations at transition area. About 10 % of experimental data, which is at the transition region, is tested with developed model. Although, the natural logarithmic normalization does not remove the confusion at the transition area completely but it is able to improve the accuracy of classification at this critical area.
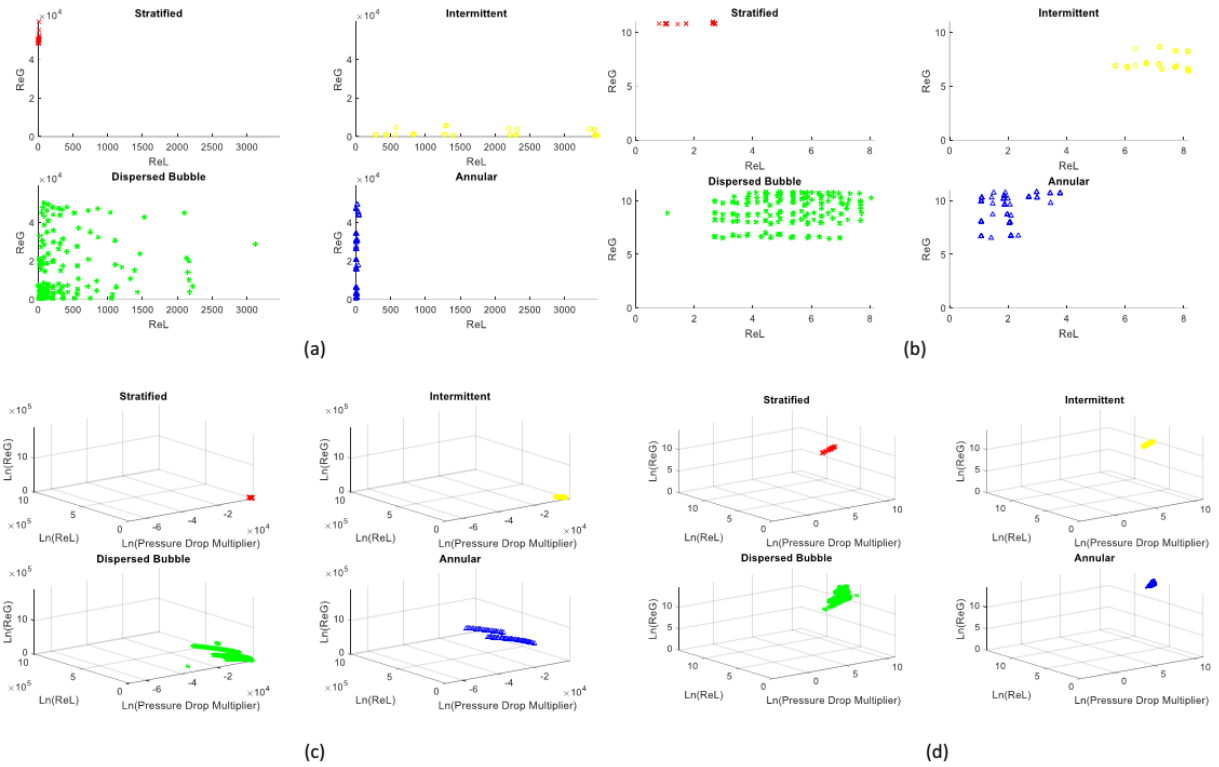
Figure 6-15: Regions of the four flow patterns using: (a) ReG, ReL for multiple pipes, (b) Natural logarithmic of (ReG, ReL) (c) ReG, ReL and $\emptyset_L^2$ for multiple pipes, (d) Natural logarithmic of (ReG, ReL and $\emptyset_L^2$).

Table 6-11: Incorrect classification %: (a) ReG, ReL ,(b) Ln (ReL), Ln (ReG) , (c) ReL, ReG,$\emptyset_L^2$,(d) Ln(ReL), Ln(ReG), Ln($\emptyset_L^2$).

	% Incorrect Classification			
	AN	DB	INT	STR
AN	---------	0.0 %	4.17 %	0.0 %
DB	0.0 %	--------	2.78 %	0.0 %
INT	14.29 %	22.22 %	---------	36.0%
STR	0.0 %	0.0 %	4.17 %	---------
Total	14.29 %	22.22%	11.1 %	36.6%

(a)

	% Incorrect Classification			
	AN	DB	INT	STR

	AN	DB	INT	STR
AN	---------	0.0 %	0.0 %	0.0 %
DB	0.0 %	--------	3.9 %	0.0 %
INT	0.0 %	22.22%	--------	5.0 %
STR	0.0 %	0 %	1.3 %	--------
Total	0.0 %	22.2%	5.2 %	5.5 %

(b)

	% Incorrect Classification			
	AN	DB	INT	STR
AN	---------	0.0 %	3.95 %	0.0 %
DB	0.0 %	---------	3.95 %	0.0 %
INT	0.0 %	36.36 %	---------	33.33 %
STR	0.0 %	0.0 %	1.32 %	---------
Total	0.0 %	36.36 %	9.2 %	33.33 %

(c)

	% Incorrect Classification			
	AN	DB	INT	STR
AN	---------	0 %	0.0 %	0.0 %
DB	0.0 %	--------	0.0 %	0.0 %
INT	0.0 %	8.3%	---------	0.0 %
STR	0.0 %	0 %	1.3 %	---------
Total	0.0 %	8.3 %	1.3 %	0.0 %

(d)

Table 6-12: Percent of correct classification.

Parameter/ Pattern	% Correct Classification				
	AN	DB	INT	STR	Total
Re_L, Re_G	85.7%	77.8 %	88.9 %	64.0%	82.3 %
$Ln(Re_L)$, $Ln(Re_G)$	100.0 %	77.8%	94.8%	95.0 %	93.8 %
Re_L, Re_G, $\emptyset_L^2$	100.0 %	63.6 %	90.8 %	66.7 %	85.0 %
$Ln(Re_L)$, $ln(Re_G)$, $ln(\emptyset_L^2)$	100.0 %	91.7 %	98. 7%	100.0 %	98.2 %

Table 6-13: Misclassified percentage at transition region.

Parameters	Percentage of misclassified
Re_L, Re_G	38.9 %
$Ln(Re_L)$, $Ln(Re_G)$	25.0 %
Re_L, Re_G, $\emptyset_L^2$	33.3 %
$Ln(Re_L)$, $ln(Re_G)$, $ln(\emptyset_L^2)$	19.4 %

Conclusion

Flow patterns identification is one of the most difficult tasks in multiphase flow analysis. In this work, we built a simple ANN Model to identify the flow patterns in horizontal pipes. The natural logarithmic normalization was used for the inputs as a pre-processing stage to properly scale the data and reduce the overlapping between flow patterns. It was clearly shown the improvement in the results using this pre-processing stage.

Then, the applicability of this procedure was extended by using dimensionless inputs to use the model for pipes with various diameters and fluids with various densities and viscosities.

Three dimensionless parameters were used as inputs to ANN. By using natural logarithmic of these three dimensionless inputs, enabled us to identify flow patterns using these parameters, namely, Liquid Reynolds Number, Gas Reynolds Number and Pressure Drop Multiplier with more than 97 % correct classification of flow patterns for a wide range of flow conditions. Finally, the concept was validated using experimental data to show the advantages of this approach. Introducing pressure drop multiplier to flow pattern map has obvious effect in improving the classification accuracy which becomes very clear for wide range of flow conditions. Regarding transition region, which is the most difficult locations in the flow pattern map, noticeable improvement has been shown. In conclusion, proper data normalization and scaling allowed the use of neural network model for flow patterns identification with high accuracy.

CHAPTER 7

CONCLUDING REMARKS

7.1 Main Contribution

1. Since the use the image processing in multiphase flow is quite new, we have prepared a Literature review for image processing in multiphase flow analysis.

2. Evaluation study of image thresholding techniques for multiphase flow.

3. Utilize Image processing to estimate the Stratified-Wavy flow Characteristics: Wave Celerity, Wavelength, Wave Frequency and Wave period, Amplitude and Hold Up.

4. Assess Drag Reducing Polymer (DRP) effects on stratified wavy flow using image processing techniques.

5. Introduce the concept of a pre-processing of the data using Logarithmic normalization for neural network to reduce confusion resulting from overlapping between flow patterns and properly scale the neural network inputs.

6. Build a neural network model using three dimensionless parameters to identify flow patterns. This model can be used to identify the flow patterns for a wide range of flow conditions regardless of pipe diameter and fluid properties.

7.2 Future Work and Recommendations

1. Proper vision system setup such as lighting system is very important to have images with needed quality for the analysis and reduce the effort and processing

time needed to prepare the images for the analysis and enhance the accuracy of the parameters estimation.

2. Advanced image processing systems such as Tomography allow the use of the image processing techniques in difficult industrial situation.

3. Artificial Intelligence (AI) is a promising technology for flow patterns identification.

4. To extend the validity of the AI model for wide range of flow conditions, it should use dimensionless inputs.

5. A pre-processing step should be applied on the inputs for proper arrangement and scaling before using them to build AI model.

6. Several important multiphase flow parameters were identified in this research. The estimated parameters could be used to provide useful information for industry such as early warning for slug formation.

7. There is a need to combine these techniques with artificial intelligence techniques and advanced computer vision algorithms to have more robust and accurate estimation.

8. Combining image processing with Artificial Intelligence (AI) can extend this method not only to estimate multiphase parameters but also it can be used to estimate more multiphase flow features such as identifying the flow patterns types using the extracted parameters from image processing.

9. Careful attention should be given to vision system to improve the quality of the image which is a key factor in this approach and make it possible to be used in difficult situations such as crude oil case.

7.3 Publications

1. M. AL-Nasser, M. Elshafei and A. AL-Sarkhi, "Image Adaptive Thresholding for Multiphase Wavy Flow," in *ASME 2014 4th Joint US-European Fluids Engineering Division Summer Meeting*, Chicago, Illinois, USA., 2014.

2. M. AL-Nasser, M. Elshafei and A. Al-Sarkhi, " Two-Phase Flow Regimes Identification using Artificial Neural Network with Nonlinear Normalization, " in 2nd International Conference on Fluid Flow, Heat and Mass Transfer , Ottawa, Ontario, Canada, 2015.

3. M. AL-Nasser, A. Al-Sarkhi and M. Elshafei, "Dimensionless Model for Flow Regimes Identification Using Artificial Neural Network," Journal of Fluid Flow, Heat and Mass Transfer, 2015 (Accepted).

4. M. AL-Nasser, M. Elshafei and A. Al-Sarkhi " Multiphase Flow Measurements Using Image Processing: A Critical Review" Journal of Brazilian Society of Mechanical Science and Engineering, 2015 (Submitted).

5. M. AL-Nasser, A. Al-Sarkhi and M. Elshafei, "Artificial Neural Network Application for Multiphase Flow Patterns Detection: A new Approach, " Journal of Petroleum Science and Engineering, 2016 (Submitted).

6. I. Alsurakji, M. AL-Nasser, A. Al-Sarkhi and M. Elshafei "Flow Characteristics with and without reducing drag polymer using PIV and Image Processing" under preparation to be submitted to a Journal.

REFERENCES

[1] S. Corneliussen, J.-P. Couput, E. Dahl, E. Dykesteen, K.-E. Frøysa, E. Malde, H. Moestue, P. Moksnes, L. Scheers and H. Tunheim, Handbook of Multiphase Flow Metering, OSLO: NFOGM & Tekna, 2005.

[2] M. Al-Kadem , F. T. Al Khelaiwi , A. Al Mashhad, M. Al Dabbous and M. Al Amri, "A Decade of Experience with Multiphase Flow Meters," in *International Petroleum Technology Conference*, Kuala Lumpur, Malaysia, 2014.

[3] Flow Research, Inc., "New study finds growth of multiphase flowmeter market outpaces all other flowmeters," Processing Solutions for the Process Industries, 2015. [Online]. Available: http://www.processingmagazine.com/company-resources/new-study-finds-growth-of-multiphase-flowmeter-market-outpaces-all-other-flowmeters/. [Accessed 2016].

[4] O. Bratland, "Update on Commercially Avaliable Flow Assurance Software Tools: What they can and cannot do ?," in *4th Asian Pipeline Conference & Exibitio*, Kuala Lumpur, Malaysia,, 2008.

[5] O. Bratland, Pipe Flow 2, Multiphase flow assurance Book, 2009.

[6] A. Robert and P. Webb, "Multiphase Flow Measurement," BP Exploration and Production, Huston Texas USA, 2007.

[7] R. A. Webb, "Multiphase Flow Measurement," BP Exploration and Production, Huston Texas USA..

[8] G. Falcone, "Multiphase Flow Metering Principles," in *Multiphase Flow Metering Principles and Applications*, Netherlands , Elsevier , 2009, p. 33–45.

[9]   Nel: flow measurement service, "Multiphase and Wet Gas," 2016. [Online]. Available: http://www.tuvnel.com/_x90lbm/An_Introduction_to_Multiphase_Flow_Measurement.pdf. [Accessed 2016].

[10] G. Wallis, One-Dimensional Two-Phase Flow, New York City: McGraw-Hill Book Co. Inc, 1969.

[11] R. Lockhart and R. Martinelli, "Proposed correlation of data for isothermal two phase, two-component flow in pipes.," *Chemical Engineering Progres,* vol. 45, pp. 39-48, 1949.

[12] H. Duns Jr. and N. Ros, "Vertical Flow of Gas and Liquid Mixtures in Wells," in *6th World Petroleum Congress*, Frankfurt am Main, German, 1963.

[13] A. Dukler, M. Wickes III and R. Cleveland, "Frictional pressure drop in two-phase flow: an approach through similarity analysis," *AIChE Journal,* vol. 10, no. 1, p. 44–51, 1964.

[14] H. Beggs and J. Brill, "A Study of Two-Phase Flow in Inclined Pipes.," *Journal of Petroleum Technology,* vol. 25, pp. 607-617, 1973.

[15] Y. Taitel and A. Dukler, "A model for predicting flow regime transitions in horizontal and near horizontal gas-liquid flow," *AIChE,* vol. 22, no. 1, p. 47–55, 1976.

[16] D. Barnea, "A unified model for predicting flow-pattern transitions for the whole range of pipe inclinations," *International Journal of Multiphase Flow,* vol. 13, no. 1, pp. 1-12, 1987.

[17] N. Petalas and K. Aziz, "A Mechanistic Model for Multiphase Flow in Pipes," *Journal of Canadian Petroleum Technology,* vol. 39, no. 6, 2000.

[18] M. Shippen and W. Bailey, "Steady-State Multiphase Flow—Past, Present, and Future, with a Perspective on Flow Assurance," *Energy Fuels,* vol. 26, no. 7, p. 4145–4157, 2012.

[19] G. Falcone, G. Hewitt, C. Alimonti and B. Harrison, "Multiphase Flow Metering: Current Trends and Future Developments," *Journal of Petroleum Technology,* vol. 54, no. 4, pp. 77-84, 2002.

[20] M. Haouche, A. Tessier, Y. Deffous and J. Authier, "Virtual Flow Meter Pilot: Based on Data Validation and Reconciliation Approach," in *SPE international Production and Operation Conference and Exhibition*, Doha Qatar, 2012.

[21] B. Bringedal and A. Phillips, " Application of Virtual Flow Metering as a Backup or Alternative to Multiphase Flow Measuring Devices.,," in *Subsea Controls and Data Acquisition*, Neptune, France, 2006.

[22] B. Kruif, M. Leskens, R. Linden and G. Alberts, "Soft- sensing for Multilateral Wells with Downhole Pressure and Temperature Measurements," in *Abu-Dhabi International Petroleum Exhibition and Conference,*, Abu-Dhabi , UAE, 2008.

[23] H. Mukherjee and J. Brill, "Pressure drop correlation for inclined two phase flows," *J. Energy Res Tech,* vol. 107, pp. 549-554, 1985.

[24] A. Ansari, N. Sylvester, O. Shoham and J. Brill, "A Comprehensive Mechanistic Model for Upward Two-Phase Flow in Wellbores," in *SPE Annual Technical Conference and Exhibition*, New Orleans, Louisiana., 1990.

[25] A. Pablo, "Mechanistic Flow Modelling in pipes," SPT Group, 2012.

[26] L. Gomez, Z. Schmidt, . R. Chokshi and T. Northug, "Unified Mechanistic Model for Steady-State Two-Phase Flow: Horizontal to Vertical Upward Flow," *SPE Journal,* vol. 5, no. 3, 2000.

[27] M. Gopal and W. Jepson, "Development of digital image analysis techniques for the study of velocity and void profiles in slug flow," *International Journal of Multiphase Flow,* p. 945–965, 1997.

[28] M. Honkanen, H. Eloranta and P. Saarenrinne, "Digital imaging measurement of dense multiphase flows in industrial processes," *Flow Measurement and Instrumentation,* vol. 21, no. 1, p. 25–32, 2010.

[29] S. Goto, Y. Ishizaki, H. Ohashi and M. Akiyama, "Characteristic behavior of bubbles and slugs in transient two-phase flow using image-processing method," *Jpn. Soc. Mech. Eng,* p. 1626–1631, 1995.

[30] T. Dinh, B. Kim and T. Choi, "Application of image processing techniques in air/water two phase flow," in *Applications of Digital Image Processing*, Denver, CO, USA, 1999.

[31] A. Ozbayoglu and H. Yuksel, "Analysis of gas–liquid behavior in eccentric horizontal annuli with image processing and artificial intelligence techniques," *Journal of Petroleum Science and Engineering,* vol. 81, p. 31–40, 2012.

[32] M. Damsohn and H.-M. Prasser, "Droplet deposition measurement with high-speed camera and novel high-speed liquid film sensor with high spatial resolution," *Nuclear Engineering and Design,* vol. 241, no. 7, p. 2494–2499, 2011.

[33] C. do Amaral, R. Alves, M. da Silva and L. Arruda, "Image processing techniques for high-speed videometry in horizontal two-phase slug flows," *Flow Measurement and Instrumentation,* vol. 33, p. 257–264, 2013.

[34] A. Busciglio, G. Vella and G. Micale, "Measurement of Multiphase Flow Characteristics Via Image Analysis Techniques: The Fluidization Case Study.," in *Hydrodynamics - Theory and Model Book, Ch.7*, Italy, InTech, 2012, pp. 143-166.

[35] A. Zarubaa, E. Kreppera, H.-M. Prassera and B. Reddy , "Experimental study on bubble motion in a rectangular bubble column using high-speed video observations," *Flow Measurement and Instrumentation,* vol. 16, no. 5, p. 277–287, 2005.

[36] R. Gonzalez and R. Woods, Digital Image Processing, Third ed., Pearson Prentice Hall: New Jersey, 2008..

[37] Tutorialspoint, "Spatial Resolution," 2014. [Online]. Available: http://www.tutorialspoint.com/dip/Spatial_Resolution.htm. [Accessed 25 03 2016].

[38] J. Hiscock and C. Ching, "Gas bubble site and velocity measurements using high-speed images of gas–liquid flows," *Journal of Flow Visualization and Image Processing,* vol. 8, pp. 355-367, 2001.

[39] M. AL-Nasser, M. Elshafei and A. AL-Sarkhi, "Image Adaptive Thresholding for Multiphase Wavy Flow," in *ASME 2014 4th Joint US-European Fluids Engineering Division Summer Meeting*, Chicago, Illinois, USA., 2014.

[40] K. Hay, Z.-U. Liu and T. Hanratty, "A backlighted imaging technique for particle size measurements in two-phase flows," *Experiments in Fluids,* vol. 25, no. 3, pp. 226-232, 1998.

[41] R. Fintel, "Comparison of the Most Common Digital Interface Technologies in Vision Technology Camera Link®, USB3 Vision, GigE Vision, FireWire," Basler, Ahrensburg ,Germany, 2013.

[42] Point Grey, "Machine Vision Interface Comparison and Evolution," 2016. [Online]. Available: https://www.ptgrey.com/white-paper/id/10696. [Accessed 2016].

[43] A. B. Riaño, A. C. Bannwart and O. M. H. Rodriguez, "Holdup estimation in core flow using image processing," in *IEEE International Instrumentation and Measurement Technology Conference (I2MTC)*, Minneapolis, MN, 2013.

[44] E. Schleicher and H. Pietruske, "Wire-mesh sensors. .," HZDR, 2013. [Online]. Available: http://www.hzdr.de/db/Cms?pOid=25191&pNid=3018. [Accessed 2016].

[45] U. Hampel, "Conductivity Wire-Mesh Sensors.," HZDR, 2015. [Online]. Available: http://www.hzdr.de/db/Cms?pOid=10412&pNid=1014. [Accessed 2016].

[46] M. Da Silva and U. Hampel, "Capacitance wire-mesh sensor applied for the visualization of three-phase gas–liquid–liquid flows," *Flow Measurement and Instrumentation,* vol. 34, p. 113–117, 2013.

[47] H.-M. Prasser, D. Scholz and C. Zippe, "Bubble size measurement using wire-mesh sensors," *Flow Measurement and Instrumentation,* vol. 12, no. 4, pp. 299-312, 2001.

[48] D. Itoa, H.-M. Prasser, H. Kikura and M. Aritomi, "Uncertainty and intrusiveness of three-layer wire-mesh sensor," *Flow Measurement and Instrumentation,* vol. 22, no. 4, p. 249–256, 2011.

[49] Y. Bian, F. Dong, W. Zhang, H. Wang, C. Tan and Z. Zhang, "3D reconstruction of single rising bubble in water using digital image processing and characteristic matrix," *Particuology,* vol. 11, no. 2, p. 170– 183, July 2013.

[50] M. Elshafei, F. AL-Sunni and S. El-Ferik , "Multi-phase flow identification and measurement using image correlation". Patent US US20130211746 A1, Aug 2013.

[51] M. Robert, Basic Wave Mechanics: For Coastal and Ocean Engineers, Wiley-Interscience, 1993.

[52] M. S. de Castro, C. C. Pereira, J. N. dos Santos and O. M. H. Rodriguez, "Geometrical And Kinematic Properties Of Interfacial Waves In Horizontal Heavy Oil-Water Stratified Flow," *WIT Transactions on Engineering Sciences,* vol. 70, p. 11, 2011.

[53] J. Mohsen, "Particle Image Velocimetry: Fundamentals and Its Applications," Division of Fluid Dynamics, Department of Applied Mechanics, Chalmers University of Technology , Göteborg, Sweden, 2011.

[54] M. Raffel, C. Willert, S. Wereley and J. Kompenhans, Particle Image Velocimetry: A Practical Guide., Springer-Verlag Berlin Heidelberg, 2007.

[55] Velocimetry Technology Limited P, "Particle Image Velocimetry.," 2008. [Online]. Available: http://www.velocimetry.net/principle.htm..

[56] R. Adrian and J. Westerweel, Particle Image Velocimetry, New York: Cambridge University Press, 2011.

[57] T. Dracos, "Particle Tracking Velocimetry (PTV) - basic concepts.," in *Three-Dimensional Velocity and Vorticity Measuring and Image Analysis Techniques*, Springer Netherlands, 1996, pp. 155-160.

[58] E. Davies, Machine Vision Theory, Algorithms, Practicalities, Elsevier Inc., 2005.

[59] M. Da Silva, E. Schleicher and U. Hampel, "Capacitance wire-mesh sensor for fast measurement of phase fraction distributions," *Measurement Science and Technology,* vol. 18, no. 7, pp. 2245-2251, 2007.

[60] E. Schleicher, "Capacitance Wire Mesh Sensor," HZDR, 2013. [Online]. Available: https://www.hzdr.de/db/Cms?pOid=25207&pNid=0. [Accessed 2016].

[61] C. Saetre, G. Johansen and S. Tjugum, "Tomographic multiphase flow measurement," *Applied Radiation and Isotopes,* vol. 70, no. 7, p. 1080–1084, 2012.

[62] F. Fischer, D. Hoppe, E. Schleicher, G. Mattausch, H. Flaske, R. Bartel and U. Hampel, "An ultra fast electron beam x-ray tomography scanner," *Meas. Sci. Technol,* vol. 19, pp. 1-11, 2008.

[63] G. Falcon, G. Hewitt and C. Alimonti, "Key Multiphase flow metering techniques," in *Multiphase Flow Metering Principles and Applications*, Elsevier, 2009.

[64] F. Barthel , "Ultrafast electron beam X-ray tomography system "ROFEX".," HZDR, 2013. [Online]. Available: https://www.hzdr.de/db/Cms?pOid=30242&pNid=3523. [Accessed 2016].

[65] E. J. Mohamad , O. M. F. Marwah , R. A. Rahim, M. H. F. Rahiman and S. Z. M. Muji, "Electronic design for portable electrical capacitance sensor: A multiphase flow measurement," in *Mechatronics (ICOM), 2011 4th International Conference* , Kuala Lumpur, 2011.

[66] R. Thorn, G. Johansen and E. Hammer, "Three-Phase Flow Measurement in the Offshore Oil Industry, Is There a Place for Process Tomography?," in *1st World Congress on Industrial Process Tomography*, Greater Manchester, Buxton., 1999.

[67] Q. Wang, H. Wang and Y. Yan, "Fast reconstruction of computerized tomography images based on the cross-entropy method.," *Flow Measurement and Instrumentation,* vol. 22, no. 4, pp. 295-302, 2011.

[68] F. Fischer and U. Hampel, "Ultra fast electron beam x-ray computed tomography for two-phase flow measurement," *Nuclear Engineering and Design,* vol. 240, no. 9, pp. 2254-2259, 2010.

[69] A. Tayler and T. College, "Experimental Characterization of Bubbly Flow using MRI.PhD Thesis," Department of Chemical Engineering and Biotechnology, University of Cambridge, 2011.

[70] D. Holland, A. Blake, A. Tayler, A. Sederman and L. Gladden, "A Bayesian approach to characterising multi-phase flows using magnetic resonance: application to bubble flows," *Journal of Magnetic Resonance,* vol. 209, no. 1, pp. 83-87, 1997.

[71] Y. Lau, N. Deen and J. Kuipers, "Development of an image measurement technique for size distribution in dense bubbly flows," *Chemical Engineering Science,* vol. 94, p. 20–29, 2013.

[72] H. Aakre, T. Solbakken and R. Schüller, "An in-line NIR/endoscope technique for observations in real hydrocarbon multiphase systems," *Flow Measurement and Instrumentation,* vol. 16, no. 5, p. 289–293, 2005.

[73] M. Khatibi, "Experimental study on droplet size of dispersed oil-water flow," Norwegian University of Science and Technology ,Department of Energy and Process Engineering, 2013.

[74] J. Ma, C. Hsiao and G. Chahin, "Shared- Memory Parallelization for two-way coupled Euler-Lagrange modelling of Bubble Flows," in *4th Joint US-European Fluids Engineering Division Summer Meeting, ASME*, Chicago, 2014.

[75] J. E. McClure, . J. F. Prins, C. T. Miller and H. Wang, "Petascale Application of a Coupled CPU-GPU Algorithm for Simulation and Analysis of Multiphase Flow Solutions in Porous

Medium Systems," in *Parallel and Distributed Processing Symposium, IEEE 28th International*, Phoenix, AZ, 2014 .

[76] MathWorks, *Image Processing Toolbox: User Guide.,* 2014.

[77] R. Gonzalez, R. Woods and L. Steven, Digital Image Processing Using MATLAB, 2nd ed, Gatesmarks publishing, 2009.

[78] C. Kanan and G. Cottrell , "Kanan C, Cottrell GW (2012) Color-to-Grayscale: Does the Method Matter in Image Recognition?," *PLoS ONE 7(1): e29740. doi:10.1371/journal.pone.0029740,* vol. 7, no. 1, pp. 1-7, 2012.

[79] K. Zuiderveld, "Contrast Limited Adaptive Histogram Equalization.," in *Graphics Gems IV*, San Diego, Academic Press Professional, Inc., 1994, pp. Pages 474-485.

[80] A. Jain, Fundamentals of Digital Image Processing,, Upper Saddle River, NJ, USA: Prentice-Hall, 1989.

[81] D. Vernon, Machine Vision, Prentice-Hall, 1991.

[82] J. Russ, The Image Processing Handbook, Fifth Edition, CRC Press Taylor & Franics Group, 2006.

[83] N. Otsu, "A Threshold Selection Method from Gray-Level Histograms," *IEEE Transactions on Systems, Man, and Cybernetics,* vol. 9, no. 1, pp. 62-66, 1979.

[84] D. Bradley and G. Roth , "Adaptive Thresholding Using the Integral Image," *Journal of Graphics Tools.,* vol. 12, no. 2, pp. 13-21, 2007.

[85] J. Sauvola and M. Pietikainen , "Adaptive document image binarization," *Pattern Recognition,* vol. 33, pp. 225-236, 2000.

[86] W. Niblack, An introduction to digital image processing, Englewood Cliffs, New Jersey: Prentice Hall, 1986.

[87] G. Xiong, "Adaptive Thresholding," HIPR2, 2003. [Online]. Available: http://homepages.inf.ed.ac.uk/rbf/HIPR2/adpthrsh.htm. [Accessed 2016].

[88] J. Bernsen, "Dynamic thresholding of gray-level images," in *International Conference on Pattern Recognition*, 1986.

[89] N. Ray and B. N. Saha, "Edge Sensitive Variational Image Thresholding," in *IEEE International Conference on Image Processing (ICIP)*, San Antonio, TX, 2007.

[90] Horizon JIP, "Wavy Flow: Smooth waves," 2013. [Online]. Available: https://www.youtube.com/watch?v=s7tX6fPIt3s. [Accessed 2016].

[91] National Instrument., "Thresholding," 2012. [Online]. Available: http://zone.ni.com/reference/en-XX/help/372916M-01/nivisionconcepts/thresholding/.

[92] Z. Xizhi , "The Application of Wavelet Transform in Digital Image Processing," in *MultiMedia and Information Technology*, Three Gorges, 2008.

[93] S. Umbaugh , Computer Vision and Image Processing, Prentice Hall PTR, 1998.

[94] M. Bertalmio, L. Vese, G. Sapiro and S. Osher, "Simultaneous Structure and Texture Image Inpainting," in *IEEE Scoitey Conference on Computer Vision and Pattern Recognition*, 2003.

[95] WOLFARM, "WOLFARM Language and System , Documentation center," 2015. [Online]. Available: http://reference.wolfram.com/language/ref/Inpaint.html. [Accessed 2016].

[96] D. Schubring and T. Shedd, "Wave behavior in horizontal annular air–water flow," *International Journal of Multiphase Flow,* vol. 34, no. 7, pp. 636-646, 2008.

[97] A. Al-Sarkhi, C. Scaria and K. Magrini, "Inclination effects on wave characteristics in annular gas–liquid flows. AIChE J. 58, 1018–1029.," *AIChE,* no. 58, p. 1018–1029., 2011.

[98] K. Gawas, H. Karami, E. Pereyra, A. Al-Sarkhi and C. Sarica, "Wave characteristics in gas–oil two phase flow and large pipe diameter," *International Journal of Multiphase Flow,* vol. 63, pp. 93-104, 2014.

[99] A. Ousaka, I. Morioka and T. Fukano, "Air-water annular two-phase flow in horizontal and near horizontal tubes: Disturbance wave characteristics and liquid transportation," *Japanese Journal of Multiphase Flow,* vol. 6, no. 9, pp. 80-87, 1992.

[100] A. Setyawan , I. Indarto and D. Deendarlianto, "Experimental Investigation on Disturbance Wave Velocity and Frequency in Air-Water Horizontal Annular Flow," *Modern Applied Science,* vol. 8, no. 4, pp. 84-96, 2014.

[101] T. Xiea, S. Chiaasiaana and S. Karrila, "Artificial neural network approach for flow regime classification in gas–liquid–¬fiber flows based on frequency domain analysis of pressure signals, " *Chemical Engineering Science,* vol. 59, no. 11, pp. 2241-2251, 2004.

[102] E. Rosa, R. Salgado, T. Ohishi and N. Mastelari, ""Performance comparison of artificial neural networks and expert systems applied to flow pattern identification in vertical ascendant gas–liquid flows,"," *International Journal of Multiphase Flow,* vol. 36, no. 9, pp. 738-754, 2010.

[103] E. A. El-Sebakhy , "Flow regimes identification and liquid-holdup prediction in horizontal multiphase flow based on neuro-fuzzy inference systems," *Mathematics and Computers in Simulation,* vol. 80, no. 9, pp. 1854-1866, 2010.

[104] S. Haykin , "Neural Networks; A Comprehensive Foundation, NJ: Macmillan Publishing Company Englewood Cliffs, 1994.

[105] K. Hornik, M. Stinchombe and H. White, "Multilayer feed-forward network are universal approximators,"," *Neural Networks,* vol. 2, no. 5, pp. 359-366, 1989.

[106] M. Stinchcombe and H. White, "Multilayer feed-forward network are universal approximators," *Neural Networks,* vol. 2, pp. 359-366, 1989.

[107] J. Hopfield, "Neural networks and physical systems with emergent collective computational abilities," *Proc. Of the National Academy of Sciences of the U.S.A.,* vol. 79, pp. 2554-2558, 1982.

[108] R. Jacob, "Increased Rates of Convergence Through Learning Rate Adaptation," *Neural Networks,* vol. 1, pp. 295-307, 1988.

[109] M. Moller, "A Scaled Conjugate Gradient Algorithm for Fast Supervised Learning," *Neural Networks,* vol. 6, pp. 525-533, 1993.

[110] H.-Q. Zhang and C. Sarica, ""Unified Modeling for Gas/Oil/Water Pipe Flow-Basic Approaches and Preliminary Validation," *SPE J. Project, Facilities & Construction,* vol. 1, no. 2, pp. 1-7, 2006.

[111] H.-Q. Zhang, Q. Wang, C. Sarica and J. Brill, "Unified Model for Gas-Liquid Pipe Flow via Slug Dynamics—Part 1: Model Development," *Journal of Energy Resources Technology,* vol. 125, no. 4, pp. 266-273 , 2003.

[112] P. Vassallo and K. Keller, ""Two-phase frictional pressure drop multipliers for SUVA R-134a flowing in a rectangular duct," *International Journal of Multiphase Flow,* vol. 32, no. 4, pp. 466-482, 2006.

[113] R. Brito, "Effect of Medium Oil Viscosity on Two-Phase Oil-Gas Flow Behavior in Horizontal Pipes," MS Thesis, The University of Tulsa., 2012.

[114] Y. Taitel and A. E. Dukler, "A model for predicting flow regime transitions in horizontal and near horizontal gas-liquid flow," *AIChE Journal,* vol. 22, no. 1, pp. 47-55, 1976.

VITAE

Name   : MUSTAFA AHMAD ALNASER

Nationality   : Syrian

Date of Birth   : 4/26/1982

Email   : Mustafa_n82@yahoo.com

Address   : Dammam

Academic Background : System Engineering

Education:

BS in Control & Instrumentation System Engineering - King Fahd University of Petroleum & Minerals (KFUPM) - Saudi Arabia (2006)

MSc in System Engineering - KFUPM – Saudi Arabia (2009)

PhD. in System & Control Engineering – KFUPM - Saudi Arabia (2016)

Publications:

1. M. AL-Nasser, M. Elshafei and A. Al-Sarkhi, "Image Adaptive Thresholding for Multiphase Wavy Flow," in ASME 2014 4th Joint US-European Fluids Engineering Division Summer Meeting, Chicago, Illinois, USA., 2014.

2. M. AL-Naser, M. Elshafei and A. Al-Sarkhi, "Two-Phase Flow Regimes Identification using Artificial Neural Network with Nonlinear Normalization, " in 2nd International Conference on Fluid Flow, Heat and Mass Transfer , Ottawa, Ontario, Canada, 2015.

3. M. AL-Naser, A. Al-Sarkhi and M. Elshafei, "Dimensionless Model for Flow Regimes Identification Using Artificial Neural Network," Journal of Fluid Flow, Heat and Mass Transfer, 2015 (Accepted).

4. M. AL-Naser, M. Elshafei and A. Al-Sarkhi "Multiphase Flow Measurements Using Image Processing: A Critical Review" Journal of Brazilian Society of Mechanical Science and Engineering, 2015 (Submitted).

5. M. AL-Naser, A. Al-Sarkhi and M. Elshafei, "Artificial Neural Network Application for Multiphase Flow Patterns Detection: A new Approach, " Journal of Petroleum Science and Engineering, 2016 (Submitted).